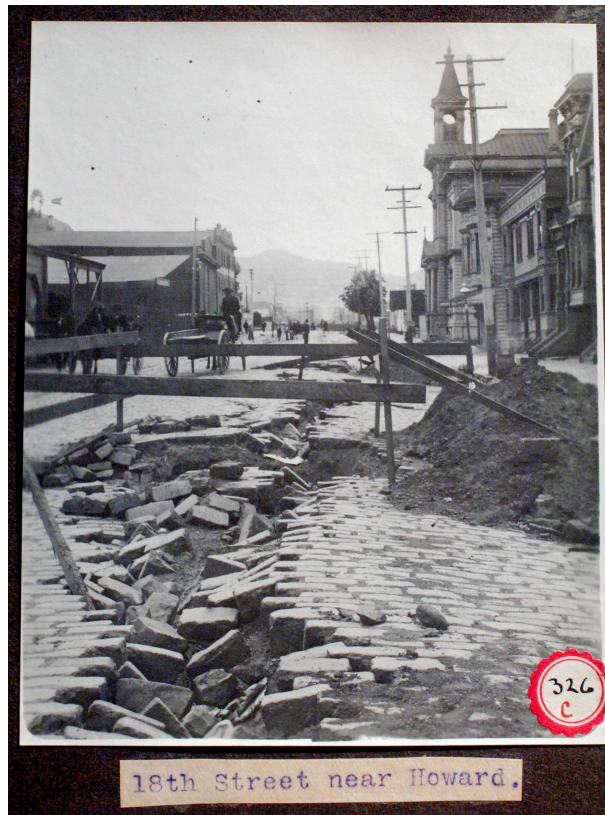


# Berkeley Seismological Laboratory



**Annual Report**  
**July 2005 - June 2006**

**Berkeley Seismological Laboratory**  
**Annual Report**  
**July 2005 - June 2006**

Cover Picture

Photograph of damage to 18th Street near Howard St. in San Francisco due to the 1906 earthquake. This photograph, from the archives of the Berkeley Seismological Laboratory was one of many taken by H.C. Branner in his efforts to document the effects of the quake for the *Report of the State Earthquake Investigation Commission*

# Contents

<b>1</b>	<b>Director's Report</b>	<b>1</b>
1.	Background and Facilities . . . . .	2
2.	Highlights of 2005-2006 . . . . .	3
3.	BSL staff news . . . . .	6
4.	Acknowledgements . . . . .	7
<b>2</b>	<b>In Memoriam: Bruce Bolt</b>	<b>8</b>
<b>3</b>	<b>Research Studies</b>	<b>11</b>
1.	Is Earthquake Rupture Deterministic? . . . . .	12
2.	Periodic Pulsing of the San Andreas Fault: An Update . . . . .	15
3.	Monitoring Nonvolcanic Tremor on the San Andreas Fault . . . . .	17
4.	Repeating Earthquakes on an Imbricated Thrust Fault in the Arc-Continent Collision Boundary of Eastern Taiwan . . . . .	19
5.	Subsurface Creep From Repeating Earthquakes at the Juncture of the San Andreas and Calaveras Faults	21
6.	Kinematic Modeling of the 2004 Parkfield Earthquake . . . . .	22
7.	Identifying Isotropic Events Using an Improved Regional Moment Tensor Inversion Technique . . . . .	24
8.	3D Simulations of Ground Motions of the 1989 Loma Prieta Earthquake Using the USGS SF06 Velocity Model . . . . .	28
9.	Toward Earthquake Early Warning in Northern California . . . . .	30
10.	Identifying and Removing Noise from the Monterey Ocean Bottom Broadband Seismic Station (MOBB) Data . . . . .	33
11.	The Orinda Earthquake Sequence: Complexity in Small Earthquakes . . . . .	36
12.	Northern California Seismicity Project . . . . .	38
13.	Seismogram Scanning Project . . . . .	40
14.	Regional Attenuation Method Comparison for Northern California . . . . .	43
15.	Geodetically Constraining Indian Plate motion and Implications for Plate Boundary Deformation . . . . .	46
16.	Large Scale Ground Deformation of Etna Observed by GPS Between 1994 and 2001 . . . . .	48
17.	Parkfield-Hollister Electromagnetic Monitoring Array . . . . .	50
18.	Observation and Analysis of Vertical Electric Fields in the Earth . . . . .	53
19.	Surface Deformation and Fault Kinematics of the San Francisco Bay Area from PS-InSAR Analysis . . . . .	57
20.	Slip of the 2004 Sumatra-Andaman Earthquake from Joint Inversion of Long Period Global Seismic Waveforms and GPS Static Offsets . . . . .	61
21.	Inversion for the Velocity Structure of the Santa Clara Valley, California . . . . .	63
22.	A Study of the Relation between Ocean Storms and the Earth's Hum . . . . .	65
23.	Physically Constrained Inversion of Long-Period Seismic Data: Insights on the Nature of the Transition Zone . . . . .	67
24.	The Fate of the Juan de Fuca Plate . . . . .	71
25.	Applying the Spectral Element Method to Model 3D Attenuation in the Upper Mantle . . . . .	73
26.	Radial and Azimuthal Anisotropic Structure of the North American Upper Mantle From Inversion of Surface Waveform Data . . . . .	76
27.	Improvements in Waveform Modeling and Application to Eurasian Velocity Structure . . . . .	78
28.	Toward Constraints on Lateral S Wave Velocity Gradients around the Pacific Superplume . . . . .	80
29.	Joint Inversion for 3D Velocity Structure of the Broader Africa-Eurasia Collision Region . . . . .	81

30.	A Three Dimensional Radially Anisotropic Model of Shear Velocity in the Whole Mantle . . . . .	83
31.	Short Wavelength Topography on the Inner Core Boundary . . . . .	85
32.	Long Period Seismology on Europa . . . . .	87
33.	Tidal Excitation of Free Oscillations of Icy Satellites . . . . .	89
34.	A Comparison of Standard Inversion, Neural Networks and Support Vector Machines . . . . .	92
<b>BSL Operations</b>		<b>96</b>
<b>4</b>	<b>Berkeley Digital Seismic Network</b>	<b>97</b>
1.	Introduction . . . . .	97
2.	BDSN Overview . . . . .	97
3.	2005-2006 Activities . . . . .	102
4.	Acknowledgements . . . . .	107
5.	References . . . . .	107
<b>5</b>	<b>California Integrated Seismic Network</b>	<b>108</b>
1.	Introduction . . . . .	108
2.	CISN Background . . . . .	108
3.	2005-2006 Activities . . . . .	109
4.	Statewide Integration . . . . .	111
5.	Acknowledgements . . . . .	114
6.	References . . . . .	115
<b>6</b>	<b>Northern Hayward Fault Network</b>	<b>116</b>
1.	Introduction . . . . .	116
2.	NHFN Overview . . . . .	116
3.	2005-2006 Activities . . . . .	121
4.	Acknowledgments . . . . .	125
5.	References . . . . .	125
<b>7</b>	<b>Parkfield Borehole Network (HRSN)</b>	<b>126</b>
1.	Introduction . . . . .	126
2.	HRSN Overview . . . . .	126
3.	2005-2006 Activities . . . . .	132
4.	Acknowledgments . . . . .	136
5.	References . . . . .	136
<b>8</b>	<b>Bay Area Regional Deformation Network</b>	<b>137</b>
1.	Introduction . . . . .	137
2.	BARD overview . . . . .	137
3.	2005-2006 Activities . . . . .	141
4.	Data Analysis and Results . . . . .	142
5.	Acknowledgements . . . . .	142
6.	References . . . . .	143
<b>9</b>	<b>Northern California Earthquake Data Center</b>	<b>146</b>
1.	Introduction . . . . .	146
2.	2005-2006 Activities . . . . .	146
3.	Data Collections . . . . .	146
4.	NCEDC Operations . . . . .	153
5.	Data Quality Control . . . . .	154
6.	Database Development . . . . .	154
7.	Data Distribution . . . . .	155
8.	Acknowledgements . . . . .	157

<b>10 Data Acquisition and Quality Control</b>	<b>158</b>
1. Introduction . . . . .	158
2. Data Acquisition Facilities . . . . .	158
3. Data Acquisition . . . . .	159
4. Seismic Noise Analysis . . . . .	160
5. Sensor Testing Facility . . . . .	161
6. STS-1 Electronics Development . . . . .	161
7. Acknowledgements . . . . .	162
8. References . . . . .	162
<b>11 Northern California Earthquake Monitoring</b>	<b>163</b>
1. Introduction . . . . .	163
2. Northern California Earthquake Management Center . . . . .	163
3. 2005-2006 Activities . . . . .	164
4. Routine Earthquake Analysis . . . . .	166
5. Acknowledgements . . . . .	168
6. References . . . . .	168
<b>12 Outreach and Educational Activities</b>	<b>171</b>
1. Introduction . . . . .	171
2. Highlights of 2005-2006 . . . . .	171
3. On-Going Activities . . . . .	172
4. Acknowledgements . . . . .	173
<b>13 Glossary of Common Acronyms</b>	<b>174</b>
<b>Appendix I Publications, Presentations, and Panels 2005-2006</b>	<b>175</b>
<b>Appendix II Seminar Speakers 2005-2006</b>	<b>186</b>
<b>Appendix III Organization Chart 2005-2006</b>	<b>188</b>



# Chapter 1

## Director's Report

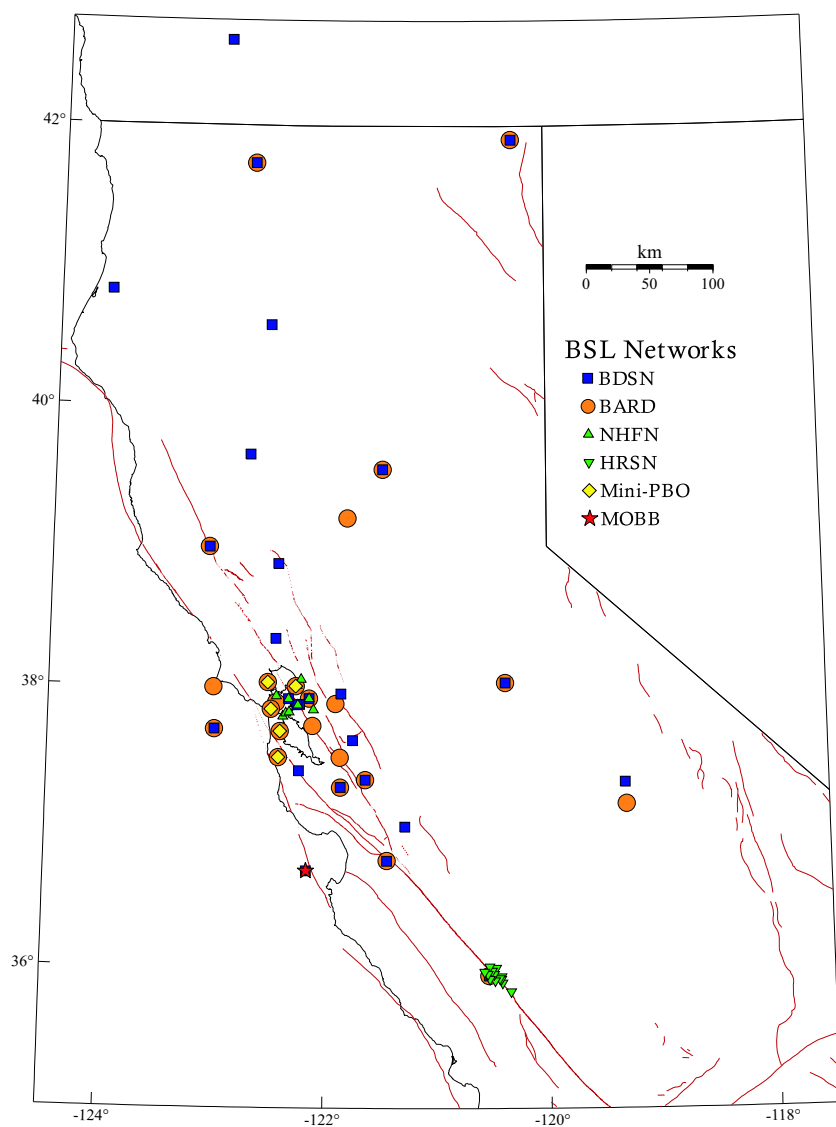


Figure 1.1: Map illustrating the distribution of stations in the BDSN, NHFN, HRSN, BARD, and Mini-PBO networks in northern and central California. A star indicates the location of the MOBB deployment.

# 1. Background and Facilities

The Berkeley Seismological Laboratory (BSL), formerly the Berkeley Seismographic Station (BSS), is the oldest Organized Research Unit (ORU) on the UC Berkeley campus. Its mission is unique in that, in addition to research and education in seismology and earthquake-related science, it is responsible for providing timely information on earthquakes (particularly those that occur in northern and central California) to the UC Berkeley constituency, the general public, and various local and state government and private organizations. The BSL is therefore both a research center and a facility/data resource, which sets it apart from most other ORUs. A major component of our activities is focused on developing and maintaining several regional observational networks, and participating, along with other agencies, in various aspects of the collection, analysis, archival, and distribution of data pertaining to earthquakes, while maintaining a vigorous research program on earthquake processes and Earth structure. In addition, the BSL staff spends considerable time with public relations activities, including tours, talks to public groups, responding to public inquiries about earthquakes, and, more recently, World-Wide-Web presence (<http://www.seismo.berkeley.edu/seismo/>).

UC Berkeley installed the first seismograph in the Western Hemisphere at Mount Hamilton (MHC) in 1887. Since then, it has played a leading role in the operation of state-of-the-art seismic instruments and in the development of advanced methods for seismic data analysis and interpretation. Notably, the installation, starting in 1927, of Wood-Anderson seismographs at 4 locations in northern California (BKS, ARC, MIN and MHC) allowed the accurate determination of local earthquake magnitude ( $M_L$ ) from which a unique historical catalog of regional earthquakes has been maintained to this day, providing crucial input to earthquake probabilities studies.

Over the years, the BSS continued to keep apace of technological improvements. The first centrally telemetered network using phone lines in an active seismic region was installed by BSS in 1960. The BSS was the first institution in California to operate a 3-component “broadband” system (1963). Notably, the BSS played a major role in the early characterization of earthquake sources using “moment tensors” and source-time functions, and made important contributions to the early definitions of detection/discrimination of underground nuclear tests and to earthquake hazards work, jointly with UCB Engineering. Starting in 1986, the BSS acquired 4 state-of-the-art broadband instruments (STS-1), while simultaneously developing PC-based digital telemetry, albeit with limited resources. As the telecommunication and computer technology made rapid progress, in parallel with broadband instrument development, paper record reading could be completely abandoned in favor of largely

automated digital data analysis.

The current modern facilities of BSL have been progressively built over the last 14 years, initiated by significant “upgrade” funding from UC Berkeley in 1991-1995. The BSL currently operates and acquires data, continuously and in real-time, from over 60 regional observatories, housing a combination of broadband and strong motion seismic instrumentation installed in vaults, borehole seismic instrumentation, permanent GPS stations of the Bay Area Regional Deformation (BARD) network, and electromagnetic sensors. The seismic data are fed into the BSL real-time processing and analysis system and are used in conjunction with data from the USGS NCSN network in the joint earthquake notification program for northern California, started in 1996. This program capitalizes on the complementary capabilities of the networks operated by each institution to provide rapid and reliable information on the location, size and other relevant source parameters of regional earthquakes. In recent years, a major emphasis in BSL instrumentation has been in densifying the state-of-the-art seismic and geodetic networks, while a major on-going emphasis in research has been the development of robust methods for quasi-real time automatic determination of earthquake source parameters and predicted strong ground motion, using a sparse network combining broadband and strong motion seismic sensors, as well as permanent geodetic GPS receivers.

The backbone of the BSL operations is a regional network of 25+ digital broadband and strong motion seismic stations, the Berkeley Digital Seismic Network (BDSN), with continuous telemetry to UC Berkeley. This network provides the basic regional data for the real-time estimation of location, size and rupture parameters for earthquakes of M 3 and larger in central and northern California, within our Rapid Earthquake Data Integration (REDI) program and is the Berkeley contribution to the California Integrated Seismic Network (CISN). It also provides a fundamental database for the investigation of three-dimensional crustal structure and its effects on regional seismic wave propagation, which is ultimately crucial for estimating ground shaking for future earthquakes. Most stations also record auxiliary temperature/pressure channels, valuable in particular for background noise quality control. Complementing this network is a  $\sim 25$  station “high-resolution” network of borehole seismic sensors located along the Hayward Fault (HFN) and under the Bay Area bridges, operated jointly with the USGS/Menlo Park and linked to the Bridge Safety Project of the California Department of Transportation (Caltrans). The latter has facilitated the installation of sensor packages at 15 bedrock boreholes along 5 east-bay bridges in collaboration with Lawrence Livermore National Laboratory (LLNL). A major science goal of this network is to collect high signal-to-noise data

for micro-earthquakes along the Hayward Fault to gain insight into the physics that govern fault rupture and its nucleation. The BSL is also involved in the operation and maintenance of the 13 element Parkfield borehole seismic array (HRSN), which is yielding enlightening results on quasi-periodic behavior of micro-earthquake clusters and important new constraints on earthquake scaling laws and is currently playing an important role in the characterization of the site for the future San Andreas Fault Observatory at Depth (SAFOD). Since April 2002, the BSL is also involved in the operation of a permanent broadband ocean bottom station, MOBB, in collaboration with MBARI (Monterey Bay Aquarium Research Institute).

In addition to the seismic networks, the BSL is involved in data archival and distribution for the permanent geodetic BARD Network as well as the operation, maintenance, and data processing of 22 out of its 70+ sites. Whenever possible, BARD sites are collocated with BDSN sites in order to minimize telemetry costs. In particular, the development of analysis methods combining the seismic and geodetic data for the rapid estimation of source parameters of significant earthquakes has been one focus of BSL research.

Finally, two of the BDSN stations (PKD, SAO) also share data acquisition and telemetry with 5-component electromagnetic sensors installed with the goal of investigating the possibility of detection of tectonic signals. In 2002-2003, an automated quality control software was implemented to monitor the electromagnetic data.

Archival and distribution of data from these and other regional networks is performed at the Northern California Earthquake Data Center (NCEDC), operated at the BSL in collaboration with USGS/Menlo Park. The data reside on a mass-storage device (current holdings  $\sim 10$  TerraBytes), and are accessible "on-line" over the Internet (<http://www.quake.geo.berkeley.edu>). Among others, data from the USGS Northern California Seismic Network (NCSN), are archived and distributed through the NCEDC. The NCEDC also maintains, archives and distributes the ANSS/CNSS earthquake catalog.

Core University funding to our ORU has suffered from permanent budget cuts to research programs from the State of California, and currently provides salary support for 2 field engineers, one computer expert, 2 data analysts, 1 staff scientist and 2 administrative staff. This supports a diminishing portion of the operations of the BDSN and provides seed funding for our other activities. All other programs are supported through extramural grants primarily from the USGS and NSF, and in the past five years, the Governor's Office of Emergency Services (OES). We acknowledge valuable recent contributions from other sources such as Caltrans, the CLC program and PEER, as well as our Earthquake Research Affiliates.

## 2. Highlights of 2005-2006

### 2.1 Research Accomplishments

Chapter 3 documents the main research contributions of the past year. Research at the BSL spans a broad range of topics, from the study of microseismicity at the local scale to global deep earth structure, and includes the use of seismological, geodetic, and remote sensing (InSAR) techniques.

Richard Allen and his students have continued to develop a methodology for earthquake early warning (1.,9.), documenting, in particular, that, for large earthquakes, the frequency content of radiated seismic energy within the first few seconds of rupture scales with the final magnitude of the event.

Bob Nadeau and collaborators continued to work on characteristically repeating micro-earthquakes (2.,5.). In particular, Nadeau has extended the study published in 2004 to investigate if the time varying patterns of periodic pulsing of deep slip, extends through an additional 5 years. The successful prediction of time periods with increased likelihood for larger earthquakes based on his earlier data suggest that there is significant potential in his approach to refine time dependent earthquake forecasts, at least for the central San Andreas Fault segment (2.). Nadeau and collaborators are also studying repeating earthquakes in other tectonic settings, such as Taiwan (4.).

Studies of data generated by the M6 2004 Parkfield earthquakes continue. Nadeau and collaborators have been further documenting the time and space distribution of non-volcanic tremors on the San Andreas fault near Parkfield (3.). Graduate student Karl Kappler has been refining EM data analysis procedures (17., 34., 18.). Doug Dreger and his student Ahyi Kim have developed a kinematic model of the Parkfield earthquake using jointly GPS and seismic data (6.).

Doug Dreger and his students and collaborators have also worked on a variety of source and structure topics including the development of a promising method to identify seismic events with a strong isotropic component, very relevant to the recent nuclear test in North Korea (7.), new earthquake ground motion simulations using the recently developed USGS SF06 velocity model (8.), the determination of structure in the Santa Clara Valley using both teleseisms and microearthquake data (21.), and evaluation of methodologies to constrain attenuation models in northern California (14.).

Geodetic studies include work by Roland Bürgmann and his students and post-docs on the surface deformation in the San Francisco Bay Area using InSAR data (19.) and on the motion of the Indian plate (15.), as well as work by Nicolas Houlié and collaborators on the deformation of the Etna volcano, using GPS (16.). In a collaborative effort involving three BSL faculty members

(Dreger, Bürgmann and Romanowicz), separate tools developed by each of them were combined by graduate student Junkee Rhie to obtain a slip model for the great M9 2004 Sumatra earthquake, based on teleseismic and near field geodetic data (20.).

Other regional studies include continuation by Bob Uhrhammer of the study of Bay Area historical seismicity (12.) and, in particular, scanning of old seismograms with the help of undergraduates (13.); the study by Peggy Hellweg of an unusual sequence of earthquakes near Orinda, CA (11.); and the development of a methodology to reduce long period ocean noise at the broadband ocean bottom station MOBB(21.).

On the topic of relation of oceanography and seismology, Romanowicz and her student Junkee Rhie have continued their study of the relation of ocean storms to the earth's long period noise known as "hum", and followed a particular sequence of storms across the Pacific (22.), showing how the generation of the hum involves a three stage process (ocean waves, infragravity waves, seismic waves).

Deep earth structure studies start in the upper mantle, with work by graduate student Mei Xue with Richard Allen on a regional tomographic model beneath northwestern US, tracking the fate of the Juan de Fuca plate down to 400 km (24.), while post-doc Federica Marone, working with Barbara Romanowicz, has developed a tomographic model of S velocity and anisotropy beneath the entire North American continent, documenting the presence of two layers of anisotropy beneath the stable continent, one in the lithosphere and one in the asthenosphere (26.). Federica has also been working, with collaborators at Northwestern Univ., on a similar model for the Mediterranean region (29.). Also on the regional scale, graduate student Ahyi Kim, working with post-doc Mark Panning and Barbara Romanowicz, has developed a regional upper mantle 3D model for southeast Asia (27.). This model is the first step towards developing a higher resolution model of this region using more sophisticated tools for 3D wave propagation.

As in previous years, Romanowicz and her group have continued their work on refining tomographic models of mantle structure at the global scale (30.,28.) and have started to obtain results from a new approach, combining seismic and mineral physics constraints to map lateral variations of temperature and composition in the upper mantle (23.). Also, graduate student Ved Lekic has started constructing a new global 3D model of attenuation in the upper mantle, using the spectral element method to compute synthetic seismograms in an elastic model (25.). With post-doc Aimin Cao, Romanowicz also continues work on core structure, one example of which is given in this report, documenting the possible presence of short wavelength topography on the inner core boundary (31.).

Finally, combining expertise in seismology and geodynamics, a study of the constraints on the structure of Jupiter's satellite Europa that could be obtained with seismic data has given rise to two publications (32.), while Ved Lekic, working with Michael Manga, has been investigating tidal excitation of free oscillations on Saturn's moon Enceladus (33.).

## 2.2 Infrastructure and Earthquake Notification

Highlights in 2005-06 include the BSL's participation in the commemoration activities of the 1906 earthquake's centennial anniversary (see Chapter 12). These activities included a joint SSA/EERI/DRC conference which was held in San Francisco in April 2006. The BSL, and specifically Dr Peggy Hellweg, were heavily involved in its organization. The BSL also helped develop many exhibits, classes, and a series of public lectures on the UC Berkeley Campus, which were held between October 2005 and April 2006. Richard Allen and Barbara Romanowicz taught a Freshman Seminar on the subject of the 1906 earthquake and earthquake preparedness, which resulted in an informational movie, put together by the students, and targeted at incoming Berkeley freshmen. This movie is available through several websites on Campus, in particular: <http://seismo.berkeley.edu/~rallen/BEAR>

Another new activity began in February 2006, with funding from NSF through the IRIS/GSN program (Global Seismic Network). It is a collaborative project with Tom VanZandt of Metrozet on the design and testing of new electronics for the STS-1 very broadband seismometer which occupies several hundred sites around the world, and in particular 10 of the Berkeley sites. The manufacturer of this sensor of unsurpassed quality has discontinued its production, but no equivalent new instrument of any design is available. Meanwhile the STS-1s, many of which have been around for 15-20 years, are deteriorating with age. In the Spring of 2006, significant effort was deployed at BSL to set up a testbed at the Byerly Vault to test successive iterations of new electronics developed by Metrozet.

As in the previous year, BSL's infrastructure development efforts have centered around several major projects:

- operation and enhancement of the joint earthquake notification system with USGS/Menlo Park.
- the continuing development of the California Integrated Seismic Network
- participation, at various levels, in three components of the national Earthscope program: the deployment in northern California of the *BigFoot* component of USArray, archival of borehole strainmeter data in the framework of the Plate Boundary Observatory (PBO), and the preparation for archival

of the data from the San Andreas Fault Observatory at Depth (SAFOD).

- development of borehole networks at Parkfield and along the Hayward Fault
- operation and further enhancements of the BARD network of continuous GPS
- operation of the Northern California Earthquake Data Center

The main goal of the CISN (see Chapter 5) is to ensure a more uniform system for earthquake monitoring and reporting in California. The highest priority, from the point of view of emergency responders in California, is to improve the robustness of statewide real-time notification and to achieve a uniform interface across the State to the California OES and other emergency responders. This represents a major challenge, as the CISN started as a heterogeneous collection of networks with disparate instrumentation, software systems and culture. Much effort has gone over the past few years to develop coordinated software between southern and northern California and in northern California, between Berkeley and USGS/Menlo Park. These two institutions are joined together in the Northern California Earthquake Management Center (NCEMC). Until now, earthquake processing responsibilities were divided into two components. Responsibility for running the association, location and duration magnitude modules has resided with Menlo Park, while local and moment magnitude, and finite-fault modules run in Berkeley. Redundancy is built into the system by operating two complete systems at all times, the second one as a "hot" backup. Recognizing potential problems associated with the separation of critical system elements across the San Francisco Bay, an effort was launched in 2001 to redesign the Northern California operations. In the new system, which is currently in advanced test mode, two complete systems, which provide processing from detection to location and computation of ground motion parameters and Shakemaps, will operate one in Berkeley and one in Menlo Park. Its implementation is awaiting the retirement of the CUSP real-time earthquake timing system in Menlo Park (see chapter 10). In the past year, CISN funds were also used to complete new broadband stations at Alder Springs, CA (GASB), and at the Marconi Conference Center near Point Reyes (MCCM). FEMA funds made available following the San Simeon earthquake of 2003 are being combined with CISN funds, to purchase equipment for 7 additional new stations that will fill gaps in the present distribution of broadband stations in northern California. This past year the equipment has been ordered and the sites identified among currently operating temporary northern California sites

of the Earthscope/USArray program. BSL staff continue to spend considerable efforts in organizational activities for CISN, notably by participating in the CISN Project Management Group (Neuhauser and Hellweg), which includes weekly 2 hour phone conferences, and the Standards Committee (Neuhauser-chair, Hellweg, Lombard), which strives to define and coordinate software development tasks. Romanowicz and Hellweg serve on the CISN Steering Committee. Doug Neuhauser has also been serving on the CISN Steering Committee in the transition period following Lind Gee's departure in summer 2005. The CISN also represents California as a designated region of ANSS (Advanced National Seismic System) and the BSL is actively involved in planning activities for the ANSS.

The BSL concluded an agreement in June 2004 with IRIS to contribute 19 stations of the BDSN to USArray, while the experiment is deployed in California. This includes 17 existing stations and the two new sites mentioned above: GASB and MCCM. In the past year, BSL has continued to acquire telemetered data from these and other northern California USArray stations and to pay particular attention to the maintenance of those permanent sites which are part of USArray.

The BSL has completed the relocation of the critical operations of data acquisition, processing, archiving and data distribution to 2195 Hearst ("SRB-1"), a recently completed building on Oxford Tract, which was constructed to current seismic codes, with special attention to post-earthquakes operability of the campus computer facility. The computer center contains state-of-the-art seismic bracing, UPS power and air conditioning with generator back-up and extensive security and equipment monitoring. In the past year, BSL has finished moving all of its data acquisition, real-time earthquake processing computers, and data archive and distribution computers to the new facility, including telemetry equipment.

The Parkfield borehole network (HRSN, see chapter 7) undertook an effort to upgrade power modules in early 2005. This has now been completed and has effectively eliminated data drop outs and gaps that had plagued the network during the winter months. The HRSN continues to play a key role in support of the Earthscope SAFOD (San Andreas Fault Observatory at Depth) drilling project, by providing low noise waveforms for events in the vicinity of the target drilling zone. A procedure is underway to refine an automated similar event detection method based on cross-correlation and pattern scanning of the continuous HRSN data, to assist researchers working on repeating micro-earthquakes as well as those working on the target events in the SAFOD drilling zone.

In the past year, infrastructure development for the Northern Hayward Fault Network (NHFN, see chapter 6) has progressed notably. The coverage on the west side of

the Bay has been augmented with the installation of the "Mini-PBO" station MHDL (Marin Headlands), which comprises borehole seismometers and a continuous GPS receiver. It is now part of the NHFN and of the BARD 8 network. Caltrans has provided funding and support for instrumentation of 3 land sites for the NHFN. Station VALB (Vallejo, CA) is operational, whereas PETB (Petaluma River Bridge) is instrumented and awaiting completion of telemetry infrastructure. The third hole has been drilled at St. Mary's College (SMCB) and is nearing completion. On-going network maintenance involves regular inspection of the collected seismic waveform data and spectra for nearby seismic events, and for noise samples, in order to assure that the instruments operate at maximum performance to capture the source spectrum of micro-earthquakes down to negative magnitudes.

The last year has been a transition period for the BARD continuous GPS (C-GPS) network, with the departure of Mark Murray and arrival of Nicolas Houlié. Also, the landscape has been changing in northern California with the construction of the Plate Boundary Observatory (PBO) of Earthscope, which is installing many new C-GPS stations. We are working with PBO to transfer several of our stations to PBO, those that are either not accessible by continuous telemetry or collocated with broadband seismic stations. We are also refocusing BARD on real-time continuous data acquisition at high sampling rates for earthquake hazards applications, responding to a growing interest of our own researchers and of the community. Data from the BARD stations have been traditionally acquired at 15 or 30 s sampling rates, but, for these applications, 1 s or higher sampling rates are needed. Conversion to these higher rates is limited by the telemetry capabilities and nature of receivers at each individual station. We started collecting 1 Hz data at 2 stations in 2003. In the last year, we progressively upgraded nine additional stations to continuous 1 Hz telemetry. These data are made publicly available at the NCEDC, while we develop methods to combine them with seismic data in our real-time earthquake notification system. We have recently acquired 5 new receivers (Ashtech  $\mu Z$ ) which will enable us to upgrade several of the sites collocated with BDSN stations.

The NCEDC (see Chapter 9), continues archival and on-line distribution of data from expanding BDSN, NHFN, HRSN, BARD, Mini-PBO, and other networks and data collections in northern California and Nevada, including telemetered continuous data from USArray stations in northern California and vicinity. We are continuing to receive data from the SAFOD pilot hole and main hole, and data from 15 SCSN (southern California) broadband sites as part of the CISN robust "backbone". Previously, only event data were archived from the 1000+ components of the Northern California Seismic Network

(NCSN) operated by USGS/Menlo Park. As a major accomplishment in the past year, we have developed the necessary software and procedures and are now archiving continuous NCSN seismograms at NCEDC. We have developed software and are retroactively working our way to transfer older data from tapes to complete the on-line collection. Having easy access to these continuous data is important, in particular, for scientists working on non-volcanic tremors. It is also of interest to global seismologists working on body waves from large teleseisms. The change from event archiving to continuous archiving has significantly increased the amount of data archived (from 35GB/year to  $\sim 1750$  GB/year). This was accomplished with no additional NCEDC staff, and was made possible by our work to automate the data delivery and archival process, and by the significant decrease in the cost of RAID disk systems.

Finally, with seed funding from the USGS to Prof. Richard Allen, we have started work on the establishment and testing of a prototype earthquake early warning system.

### 3. BSL staff news

This past year has seen many changes in BSL personnel. Following Eleanor Blair's retirement, Kristen Jensen joined BSL as our new Manager in February 2006. Kristen previously worked as senior analyst in the office of the VCR. We are very fortunate to have her. Jenny Pehl left BSL in July 2006 to follow her husband to a new job in Las Vegas. Nicolas Houlié was hired as a post-doc in February 2006 to take responsibility for our continuous GPS program.

Four graduate students associated with BSL completed their PhD's in the past year: Aimin Cao, Junkee Rhie, David Dolenc and Ingrid Johannson. Ingrid joined the USGS/Menlo Park on a Mendenhall Post-doc, David is in Minnesota (Univ. of Minnesota in Duluth), while Aimin and Junkee are staying on as post-doc's at BSL. Mark Panning, who had stayed as post-doc at BSL after completing his PhD in Fall 2004, left for Princeton in July 2006, where he has a post-doctoral fellowship.

New arrivals have continued through the summer and early Fall of 2006. Kevin Mayeda transferred from LLNL to join BSL research staff in July, while Cyndy Bresloff has been helping with routine processing and data quality control since mid-August. Tina Barber-Riggins joined the business office in September. Alexei Kireev and Mario Aranha joined the programming team in September and October, respectively. They will assist Doug Neuhauser with tasks related to the CISN, the Early Warning Project and the NCEDC.

This year has also been marked by very sad news: Professor Bruce Bolt, who was Director of the Seismographic Stations from 1963 to 1989, passed away after a brief ill-

ness on July 21, 2005, just a few months before the start of the celebrations of the 1906 San Francisco earthquake centennial. A memorial, attended by over 500 people, was held for him at the Faculty Club on July 29, 2005. We include in this report a copy of the obituary (draft version as of 10/17/06) which we have been putting together for UC Berkeley.

## 4. Acknowledgements

I wish to thank our technical and administrative staff, scientists and students for their efforts throughout the year and their contributions to this Annual Report. Individual contributions to activities and report preparation are mentioned in the corresponding sections, except for the Appendix section, prepared by Kate Conner and Kristen Jensen.

I also wish to specially thank the individuals who have regularly contributed to the smooth operation of the BSL facilities: Rich Clymer, Doug Dreger, John Friday, Jarrett Gardner, Peggy Hellweg, Nicolas Houlié, Bill Karavas, Rick Lelling, Pete Lombard, Rick McKenzie, Mark Murray, Bob Nadeau, Doug Neuhauser, Charley Paffenbarger, Bob Uhrhammer, and Stephane Zuzlewski, and in the administrative office, Kristen Jensen, Kate Conner, Jenny Pehl and Yolanda Andrade. I particularly wish to thank Doug Dreger for serving as Associate Director of the BSL, Peggy Hellweg for taking on responsibilities for CISN and data analysis coordination, Doug Neuhauser for his efforts to build the Earthscope related archival system, and Bill Karavas for organizing an effective test bed for the refurbishment of the STS-1 electronics.

I also wish to thank our undergraduate assistants, Brian Castriota, Chi Sum Chan, Mehershad Dahmubed, Josh Hunt, Kevin Lee, Rose Li, Tomasz Matlak, Rob Porritt, Jake Siegal, Gretchen Sites and Noi Valera for their contributions to our research and operational activities.

I am particularly thankful to Kate Conner and Peggy Hellweg, for their help in putting together this Annual Report.

The Annual Report of the Berkeley Seismological Laboratory is available on the WWW at [http://www.seismo.berkeley.edu/seismo/annual\\_report/](http://www.seismo.berkeley.edu/seismo/annual_report/).

Barbara Romanowicz  
October 15, 2006

## Chapter 2

# In Memoriam: Bruce Bolt

**David Brillinger, Joseph Penzien and Barbara Romanowicz**

Bruce Alan Bolt, Professor Emeritus of Seismology at the University of California, Berkeley, died suddenly of pancreatic cancer at Kaiser Permanente Medical Center in Oakland, California on July 21, 2005.

Professor Bolt was born on February 15, 1930 in the small town of Largs, New South Wales, Australia. He attended Largs Public School, Maitland Boys High School, Newcastle Technical College, New England University College, Sydney's Teachers College, and the University of Sydney, all located in New South Wales. Majoring in applied mathematics, he received a B.Sc. degree in 1952 from the New England University College, and M.Sc., Ph.D., and D.Sc. degrees in 1955, 1959, and 1972, respectively, from the University of Sydney. In 1953, he received a Diploma of Education from the Sydney Teachers College.

Having decided upon an academic career, Professor Bolt first taught at Sydney Boys High School in 1953, then progressed through the ranks as Lecturer, 1954-1959, and Senior Lecturer, 1959-1962, in the Department of Applied Mathematics at the University of Sydney. During the period 1963-1993, he served as Professor of Seismology in the Department of Geology and Geophysics at the University of California, Berkeley (UCB) and as Director of UCB's Seismographic Stations. In his early years at UCB, Professor Bolt developed strong research interests with faculty members in structural and geotechnical engineering, which resulted in his serving as Professor of Civil and Environmental Engineering during the period 1983-1993. Upon retiring from UCB in 1993, he received the campus' highest honor, the Berkeley Citation, then became Professor Emeritus of Seismology and Professor in the Graduate School, thus continuing his academic activities until his death.

As a graduate student and lecturer at the University of Sydney, Professor Bolt developed outstanding expertise in the specialty areas of applied mathematics, statistics, and geophysics. As a result, he continued to make valuable contributions to advancing knowledge in these areas throughout his career. His strongest desire was to understand natural phenomena, particularly their mathematical and statistical descriptions. He wrote numerous

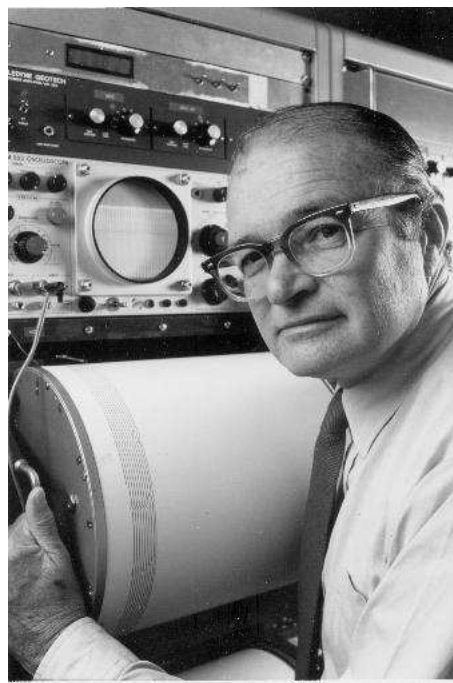


Figure 2.1: Bruce Bolt (1930 - 2005)

novel papers pertaining to the deep earth, dispersion, earthquake engineering, free oscillations, seismology, and statistics. His first published paper was a 1957 note in *Nature*, followed by one in *Geophysical Journal of the Royal Astronomical Society*, on seismic observations of the 1956 atomic explosions in Australia. In 1960, he published a paper with John Butcher on the dispersion of seismic waves, which began his deep involvement with large data sets and digital computing. His creativity in and knowledge of statistical methodologies, with influence from Harold Jeffreys, led to the estimation technique for the revision of earthquake epicenters still in use today (2006). As part of that work, he led statisticians by some ten years in developing the method of robust regression. His many contributions to seismology, including the development of earth models, have involved finite el-

ement methods, elastic wave-propagation theory, broadband and digital recording, strong-motion array development, data collection and interpretation, attenuation relations, and earthquake statistics.

Professor Bolt's numerous publications on topics in seismology include four very popular books: (1) *Earthquakes: A Primer*, 1978, (2) *Inside the Earth: Evidence from Earthquakes*, 1982, (3) *Earthquakes and Geological Discovery*, 1993, and (4) five editions of *Earthquakes*, 5th Edition, 2003. In recognition of his many contributions to seismology, he was elected Fellow of the American Geophysical Union and the Geological Society of America, Associate of the Royal Astronomical Society, and Overseas Fellow of Churchill College, Cambridge. He served as President of the Seismological Society of America in 1974 and editor of its *Bulletin* from 1965 to 1972, President of the International Association of Seismology and Physics of the Earth's Interior from 1980 to 1983, President of the Consortium of Organizations for Strong-Motion Observation Systems (COSMOS), and President of the California Academy of Sciences.

Notably, Professor Bolt was actively involved from the early 1960's through the mid-1980's in the development of reference earth models and towards this goal. contributed many measurements of body wave travel times as well as free oscillation eigenfrequencies and attenuation. He was particularly interested in constraining the average earth structure near two major interfaces: the solid/liquid core mantle boundary (CMB) and the liquid/solid inner core boundary (ICB) and focused many of his studies on the challenging topic of density. He provided some of the first robust measurements of the density jump at the ICB (1970) and also confirmed the density jump at the CMB (1985) and provided insights on the resolution of the density profile throughout the earth's interior (1975). He studied the shear velocity structure near the CMB, and the compressional velocity profile in the outer core, with a continued interest in characterizing resolution and uncertainty, which developed through a fruitful collaboration with Professor David Brillinger in Statistics. He was one of the proponents of the existence of an anomalous layer at the bottom of the outer core. His prominent observations of compressional waves (PKnKP) bouncing multiple times inside the outer core were illustrated in his textbook "Inside the Earth". These observations demonstrated that the CMB must be very spherical.

Many of Dr Bolt's observations were made on records from the Berkeley Seismographic Stations (BSS), which, in the good tradition of previous Directors, he modernized over the years and kept apace of current technology. He introduced broadband recording at Berkeley in 1963 and started replacing paper recording by magnetic tape recording in 1964. Continuing in the innovative vein, under his directorship, the BSS developed a regional

broadband digital network based on inexpensive PC microcomputers, with telemetry to Berkeley over ordinary phone lines, and including three stations equipped with state-of-the-art broadband seismometers at Berkeley, Mt Hamilton and the San Andreas Geophysical Observatory near Hollister. Because of his involvement in the BSS and the related information service on northern California earthquakes, Dr Bolt's research interests gradually shifted towards characterizing ground motions from regional earthquakes in relation to earthquake hazards in the built environment.

In addition to many contributions to seismology, Professor Bolt has made invaluable contributions to the field of earthquake engineering through teaching of basic seismology to graduate students in structural and geotechnical engineering, conducting research characterizing strong ground motions for engineering design purposes, serving as consultant on important engineering projects, and participating as a member of numerous panels, boards, and commissions. He has been an active participant in the UCB Earthquake Engineering Research Center.

Professor Bolt's consulting work focused primarily on setting seismic criteria for new and retrofit designs of important critical structures, such as dams, nuclear power plants, large bridges, underground structures, and pipelines. These structures have included the Aswan Dam, Diablo Canyon Nuclear Power Plant, Golden Gate Bridge, Bay Area Rapid Transit (BART) underground stations, BART transbay tube, and the Alaska Pipeline. His consulting work in 2005 included characterizing the controlling seismic sources and assessing tsunami risk for use in designing the now-planned (2006) suspension bridge crossing the Messina Strait between Italy and Sicily.

His setting of seismic design criteria for critical structures has involved identifying seismic-source zones, guiding the conduct of seismic hazard analyses, generating site-specific response spectra and corresponding free-field ground motions, characterizing the spatial variations of ground motions, and predicting expected future fault offsets. Further, he has participated in evaluating the seismic performance of such structures. His strong background in applied mathematics and mechanics has made it possible for him to effectively communicate with structural and geotechnical engineers on seismic-design and damage-assessment related issues.

The numerous seismic-related panels, boards, and commissions on which Professor Bolt has served include the California Department of Water Resources Consulting Board, California Department of Transportation Seismic Advisory Board, San Francisco Bay Conservation and Development Commission (BCDC) Engineering Criteria Review Board, Metropolitan Transportation Commission (MTC) Engineering and Design Advisory Panel

(EDAP), Golden Gate Bridge Seismic Instrumentation Panel, and the California Seismic Safety Commission (CSSC). As a member of CSSC, he actively participated in the Commission's sponsoring of numerous bills introduced into the legislature which became California law, thus greatly enhancing seismic hazard mitigation in the State.

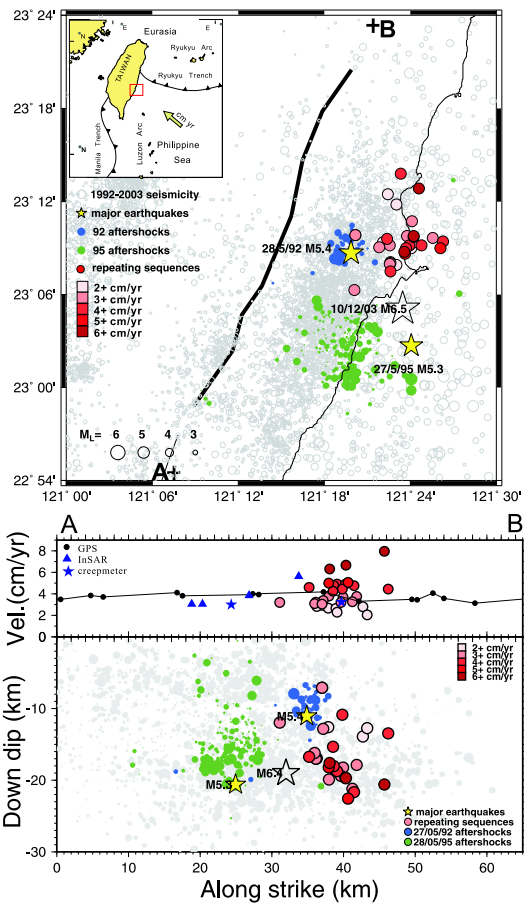
In recognition of Professor Bolt's many valuable contributions to earthquake engineering, he received the Earthquake Engineering Research Institute's 1990 George W. Housner Medal, the California Earthquake Safety Foundation's 1995 Alfred E. Alquist Medal, and was elected to the National Academy of Engineering (NAE) in 1978. His NAE citation reads as follows: "For the application of the principles of seismology and applied mathematics to engineering decisions and public policy."

Having served many years as Chair of the UCB Academic Senate and as President of the Men's Faculty Club, Professor Bolt seemed to know everyone on the Berkeley campus. His close relationship with individuals extended to a myriad of scientists and engineers worldwide. He was sought after as a speaker. Always in meeting one of his many close friends, he would extend a warm greeting with a big smile. His personal character has been admired by all who have had the pleasure of knowing him. He will be greatly missed by his friends, colleagues, students, and all who knew him.

Professor Bolt is survived by his wife Beverley (Bentley) of Berkeley, CA; three daughters, Gillian Bolt Kohli of Wellesley, MA, Helen Bolt Juarez of Fremont, CA, and Margaret Bolt Barber of Rumson, NJ; a son, Robert Bolt of Hillsborough, CA; a sister, Fay Bolt of Sydney, Australia, and fourteen grandchildren.

# Chapter 3

# Research Studies



# 1. Is Earthquake Rupture Deterministic?

Richard M Allen and Erik L Olson (University of Wisconsin, Madison)

## 1.1 Introduction

Understanding the earthquake rupture process is key to our understanding of fault systems and earthquake hazards. Over the past 15 years, multiple hypotheses concerning the nature of fault rupture have been proposed but no unifying theory has emerged. The conceptual hypothesis most commonly cited is the cascade model for fault rupture. In the cascade model, slip initiates on a small fault patch and continues to rupture further across a fault plane as long as the conditions are favorable. Two fundamental implications of this domino-like theory are that small earthquakes begin in the same manner as large earthquakes, and that the rupture process is not deterministic, i.e., the size of the earthquake cannot be determined until the cessation of rupture. Here we show that the frequency content of radiated seismic energy within the first few seconds of rupture scales with the final magnitude of the event. Therefore the magnitude of an earthquake can be estimated before the rupture is complete. This finding implies that the rupture process is to some degree deterministic and has far-reaching implications for the physics of the rupture process.

## 1.2 $\tau_p$ and $\tau_d$ observations

The frequency content of P-wave arrivals is measured through the parameter  $\tau_p$  (Allen and Kanamori, 2003; Olson and Allen, 2005). We calculate  $\tau_p$  in a recursive fashion from a vertical velocity timeseries to generate  $\tau_p$  as a function of time,  $\tau_p(t)$ . Figure 3.1 shows the vertical velocity waveform recorded during a  $M_L$  4.6 earthquake in southern California and the  $\tau_p$  timeseries derived from it. Figure 3.2 shows a similar example but for the  $M_w$  8.3 Tokachi-oki earthquake. In this case, only acceleration records are available, which have been recursively integrated in a causal fashion to derive the velocity trace from which  $\tau_p(t)$  is derived. We define the parameter  $\tau_p^{max}$  as the maximum  $\tau_p(t)$  data point between 0.05 and 4.0 sec after the P-wave trigger as shown in Figures 3.1 and 3.2.

A total of 71 earthquakes producing 1,842 waveforms recorded within 100 km are used in this study. When  $\tau_p^{max}$  is plotted against  $M$  on a log-linear scale, a scaling relation emerges as shown in Figure 3.3a. The  $\tau_p^{max}$  observations from waveforms at individual stations can exhibit large variability for a single earthquake, which is likely due to measurement error, station and path effects (Lockman and Allen, 2005). Figure 3.3a shows the average  $\tau_p^{max}$  observation for each earthquake using all

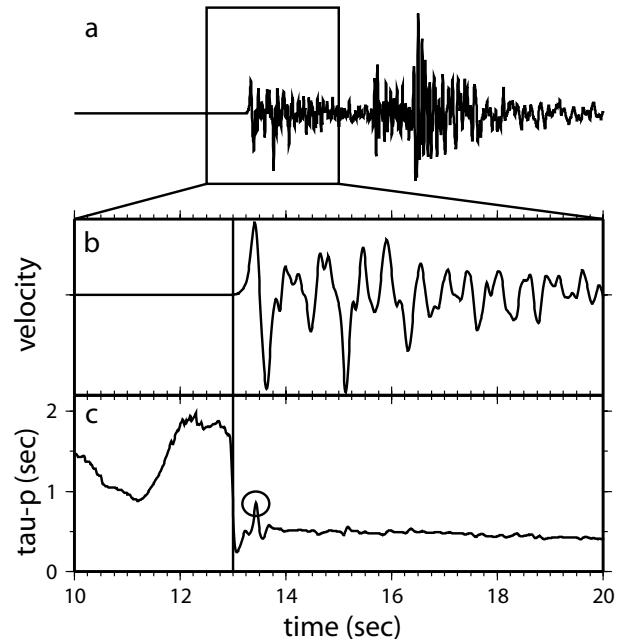


Figure 3.1: Example waveform and  $\tau_p$  calculation for a  $M$  4.6 earthquake in southern California recorded at station GSC 74 km from the epicenter. a) The raw vertical component waveform recorded by a broadband velocity sensor. b) Ten seconds of the velocity waveform after low-pass filtering at 3 Hz. The P-wave trigger time is shown by the vertical line at 13.01 sec. c)  $\tau_p(t)$  trace calculated in a recursive fashion from the waveform in b showing the change in the frequency content from the pre-trigger noise to the post-trigger P-wave. The  $\tau_p^{max}$  observation is circled (equal to 0.86 sec in this case),  $\tau_d$  is the delay of  $\tau_p^{max}$  with respect to the trigger (0.43 sec in this case).

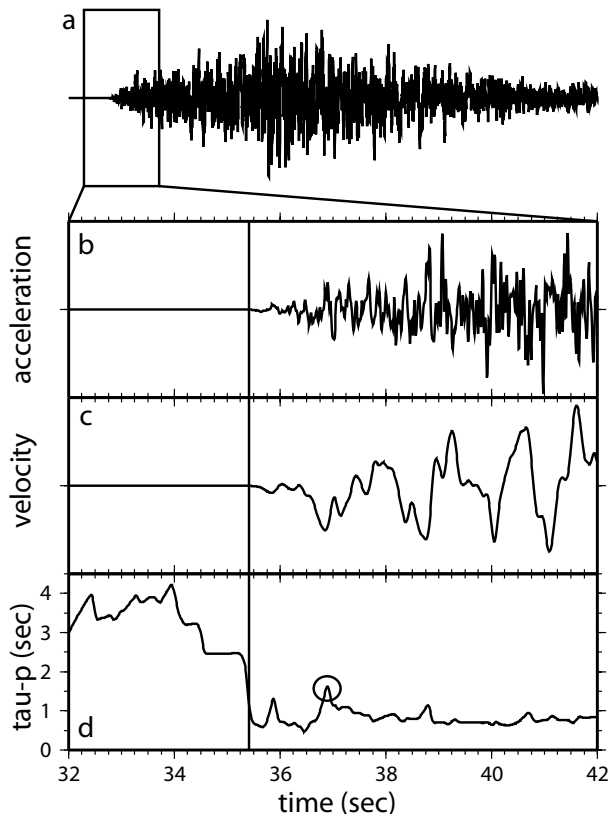


Figure 3.2: Example waveform and  $\tau_p^{max}$  calculation for the  $M_w$  8.3 Tokachi-oki earthquake recorded at station HKD112 71 km from the epicenter. a) The raw vertical component waveform recorded on an accelerometer. b) Ten seconds of the raw acceleration waveform. The P-wave trigger is shown by the vertical line at 35.41 sec. c) Ten seconds of the velocity waveform determined from the acceleration recording using recursive relations only. It has also been low-pass filtered at 3 Hz. d)  $\tau_p(t)$  trace calculated in a recursive fashion from the waveform in c. The  $\tau_p^{max}$  observation is circled ( $\tau_p^{max} = 1.62$  sec,  $\tau_d = 1.49$  sec), it has a longer period and is observed later than the example in Figure 3.1c due to the larger magnitude of the earthquake.

available data. The best-fit linear relation to the event averages is  $\log \tau_p^{max} = 0.14M - 0.83$ , and the average absolute deviation is 0.54 magnitude units. The dataset has a high linear correlation coefficient of 0.9. Although there is variability in  $\tau_p^{max}$  observations equivalent to  $\pm 1$  magnitude unit, a scaling relation is clear, implying that information about the final magnitude of an earthquake is available within the first few seconds of its initiation irrespective of the total rupture duration.

A second parameter,  $\tau_d$ , is also measured from the  $\tau_p$  timeseries.  $\tau_d$  is the delay of the  $\tau_p^{max}$  observation with respect to the P-wave trigger and is, therefore, in the range of 0.05 to 4 sec (see Figures 3.1 and 3.2). Figure 3.3b plots the event-averaged  $\tau_d$  observations versus magnitude, which shows a general increase in  $\tau_d$  with magnitude. Also indicated on Figure 3.3b is the typical rupture duration as a function of magnitude. The relation shown is only approximate as the rupture duration for a given magnitude event can vary by a factor of 2 or 3. Despite the uncertainty in the rupture duration of the specific earthquakes included in this study, it is clear that for earthquakes with  $M > 4$  the  $\tau_p^{max}$  observation is made before the rupture has ceased. While up to 4 sec of data are used to determine  $\tau_p^{max}$ , the average time window of the P-wave required to determine  $\tau_p^{max}$  is less than 2 sec for almost all earthquakes in our study.

### 1.3 Discussion

While there is a 1 magnitude unit scatter in the  $\tau_p^{max}$  data, the observations show that the rupture process is at least partly deterministic, i.e. the final magnitude of an event is to some degree controlled by processes within the first few seconds (typically  $< 2$  sec) of rupture. The scatter could be due to source processes and/or local site and measurement errors. If the scatter is non-source related, then removal or correction for site and path effects could reduce the scatter in the data points of Figure 3.3a to a single line, implying that the final magnitude of an earthquake is entirely determined within the first few seconds of rupture. Variability in the quality of the  $\tau_p^{max}$  observations at different stations has already been observed, indicating that site effects do play a role (*Lockman and Allen, 2005*). Nevertheless, it seems unlikely that all the scatter is due only to site effects. Instead, source related processes including rupture behavior, stress heterogeneity and other on-fault variability probably also play a role.

We propose that the final magnitude of an earthquake is partially controlled by the initiation process within the first few seconds of rupture, and partially by the physical state of the surrounding fault plane. The role played by the initiation process can be understood by considering the energy balance of fault rupture. A rupture can only propagate when the available energy is sufficient to supply the necessary fracture energy (*Nielsen and Olsen,*

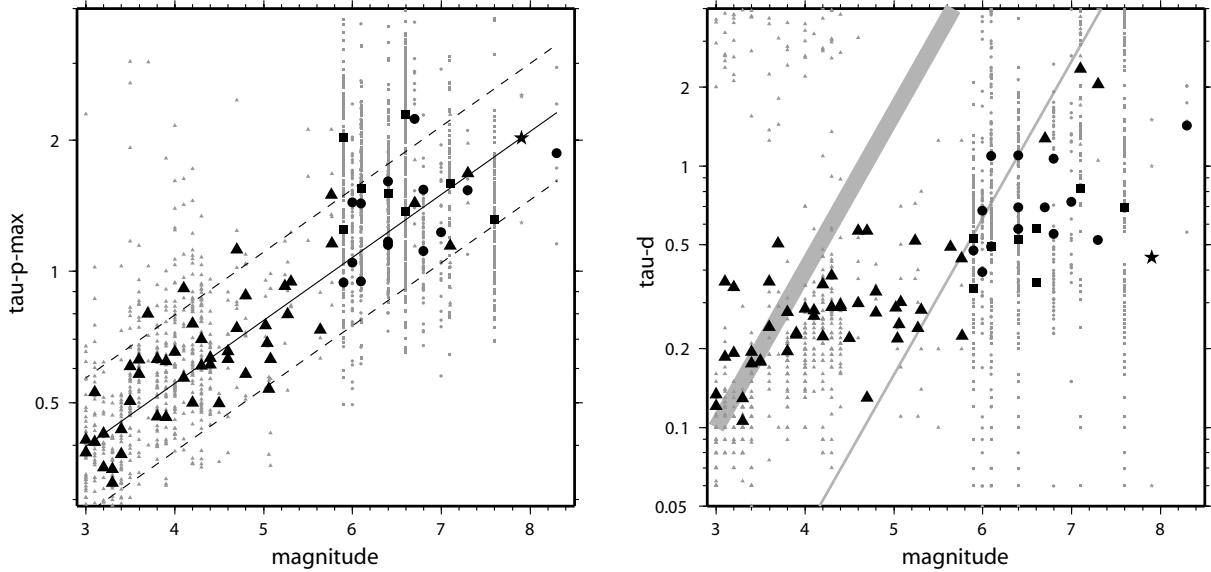


Figure 3.3: The relation between  $\tau_p^{max}$ ,  $\tau_d$  and magnitude. a) The scaling relation between event averaged  $\tau_p^{max}$  and magnitude for earthquakes in southern California (triangles), Japan (circles), Taiwan (squares) and Alaska (star). Observations at individual stations can show large scatter for a given event (small grey shapes). The event averaged values are also shown (large black symbols). The best fit line to the averages is also shown (solid). The average absolute deviation of the observations is 0.54 magnitude units; plus and minus two times the average absolute deviation is shown as dashed lines. b)  $\tau_d$  plotted against magnitude showing the general increase in the time required to make the  $\tau_p^{max}$  observation with increasing magnitude. The symbols are the same as in a. Grey shapes show individual station observations, black is the event average. The thick grey bar shows the approximate rupture duration as a function of magnitude indicating that the  $\tau_p^{max}$  observation is made before rupture ceases for all  $M > 4$  earthquakes in this study. The thin grey line indicates one tenth the rupture duration and is crossed by the trend of the  $\tau_d$  data.

2000; *Oglesby and Day, 2002*). When a propagating fracture encounters a patch with a lower stress-drop, the total energy in the system will begin to decrease. Depending on the size of the patch, it may cause the rupture to terminate. The total rupture energy available increases with the amount of slip, so a large-slip rupture will propagate further across a heterogeneous fault plane. Therefore, if the rupture pulse initiates with large slip, it is more likely to evolve into a large earthquake. This explanation is consistent with the observation that large earthquakes do not nucleate at shallow depths, but instead at greater depths where the frictional strength and stress drop are greater (*Das and Scholz, 1983*). A recent study (*Mai et al., 2005*) also shows that hypocenters are preferentially located within or close to regions of large slip.

## 1.4 Acknowledgements

We thank Hiroo Kanamori and Stefan Nielsen for helpful discussions, and Yih-Min Wu and Roger Hansen for making waveform data available for the study. Funding for this work was provided by USGS/NEHRP awards 03HQGR0043 and 05HQGR0074.

## 1.5 References

- Allen, R. M. and H. Kanamori, The potential for earthquake early warning in southern California, *Science*, *300*, 786-789, 2003.
- Das, S. and C. H. Scholz. Why large earthquakes do not nucleate at shallow depths, *Nature*, *305*, 621-623, 1983.
- Lockman, A. and R. M. Allen. Single station earthquake characterization for early warning, *Bull. seism. Soc. Am.*, *95*, 2029-2039, 2005.
- Mai, P. M., P. Spudich and J. Boatwright. Hypocenter locations in finite-source rupture models, *Bull. seism. Soc. Am.*, *95*, 965-980, 2005.
- Nielsen, S. B. and K. B. Olsen. Constraints on stress and friction from dynamic rupture models of the 1994 Northridge, California, earthquake, *Pure And Applied Geophysics*, *157*, 2029-2046, 2000.
- Oglesby, D. D. and S. M. Day, Stochastic fault stress: Implications for fault dynamics and ground motion, *Bull. seism. Soc. Am.*, *92*, 3006-3021, 2002.
- Olson, E. and R. M. Allen, The deterministic nature of earthquake rupture, *Nature*, *438*, 212-215, 2005.

## 2. Periodic Pulsing of the San Andreas Fault: An Update

Robert M. Nadeau

### 2.1 Slip Rates from Micro-quakes

A characteristically repeating micro-earthquake sequence (CS) is a sequence of small earthquakes ( $M \sim < 3.5$ ) whose seismograms, locations and magnitudes are nearly identical. Each earthquake in the sequence represents a repeated rupture of the same patch of fault, and the times between the ruptures (i.e., their recurrence intervals) are, in general, inversely proportional to the average tectonic loading rate on the fault (Nadeau and McEvilly, 1999). These unique properties allow CSs to be used to infer slip rates deep within fault zones, and they have been used to particular advantage for this purpose in regions where geodetic measurements are limited in their spatial and temporal coverage.

### 2.2 Repeating Quake Analysis along the Central SAF

Along much of the 175 km stretch of the San Andreas Fault (SAF) separating the rupture zones of California's two great earthquakes (i.e., the  $\sim$  M8 1906 San Francisco and 1857 Fort Tejon events), geodetic measurements have been done relatively infrequently in campaign mode. Along this stretch, however, over 500 CSs have been identified with events occurring between 1984 and 1999 (inclusive), and analysis of these sequences reveal: 1) that the recurrence intervals within any given CS vary significantly through time, 2) that among different CS on a localized fault segment, the recurrence variations are coherent through time, and 3) that in many cases, the coherent variations recurred quasi-periodically (Nadeau and McEvilly, 2004).

Here we report results based on an analysis of the CSs that extend the period studied by (Nadeau and McEvilly, 2004) by an additional 5 years. A primary objective of this extended analysis is to see if systematics in time-varying patterns reported in the 2004 study (i.e., the periodic pulsing of deep slip and its correlation to variations in rates of larger earthquakes) are ongoing phenomena.

### 2.3 Correlation with Larger Earthquakes

Recurrence variation information for the CSs was used to construct a profile of deep fault slip rate histories along the 175 km study zone for the 1984-2005.25 study period. The profile reveals that along the northwestern-most 80 km segment of the study zone (Figure 3.4), deep fault slip rates commonly vary by over 100% and their variation patterns (i.e., pulse patterns) recur with a periodicity of  $\sim 3$  years. Shown at the right in Figure 3.4 is a com-

parison of this large-scale periodic deep slip pattern with the occurrence times of M3.5 to M7.1 earthquakes (i.e., magnitudes larger than those of the CS events) and with the occurrence times of three known slow slip events in the area (Gwyther *et al.*, 2000). The comparison reveals a significant correlation between the onset periods of the repeating deep slip signals and the occurrence rates of the larger events. Nadeau and McEvilly (2004) observed this pattern for CS data during the period 1984-1999. With the additional 5+ years of CS data, the pattern and correlation observed by Nadeau and McEvilly appears to be continuing (Figure 3.4, right).

Excluding Loma Prieta aftershocks, 66 earthquakes with  $M > 3.5$  occurred in region during the 1984-1999 study period, and a general correlation is also observed between the occurrence times of these events and the 1-year onset periods of the pulses (i.e. the time interval where pulse slip velocities transition from low to high values). Forty-two of the 66 events were found to occur during the onset periods, this represents an occurrence rate that is 3.7 times larger than the rate observed during the non-onset periods. When Loma Prieta aftershocks are included into the analysis the onset period rate increased to 4.6 times that of the non-onset period rate.

To the resolution of the characteristic microearthquake slip rate data, the M7.1 Loma Prieta mainshock also occurred coincident with the onset of the P2 timed pulse. The times of the next two largest non-aftershock events in the area and study period (i.e., M5.4 San Juan Bautista mainshock in 1998 and a M4.7 event in 1986) are also coincident with the onset of pulses P5 and P1, respectively, and the P3, P4, and P5 pulse onsets correspond closely to the times of the three slow slip events in the area whose aseismic moment magnitudes were estimated to be  $\sim 5M_w$  (Gwyther *et al.*, 2000).

### 2.4 Implications

Earthquake triggering induced by velocity weakening effects (Dietrich, 1986) associated with increasing fault slip velocities during pulse onsets may provide an explanation for the corresponding rate increases of the larger earthquakes. It is also possible that increased quake rates occur quasi-periodically due to some other mechanism, such as the accelerated rate of loading to failure during onsets of the quasi-periodic deep slip pulses.

Regardless of the causes, the success of predictions of time periods with increased likelihood for larger quakes during the additional 5+ year period, based on the pattern of pulsing that occurred prior to the end of 1999

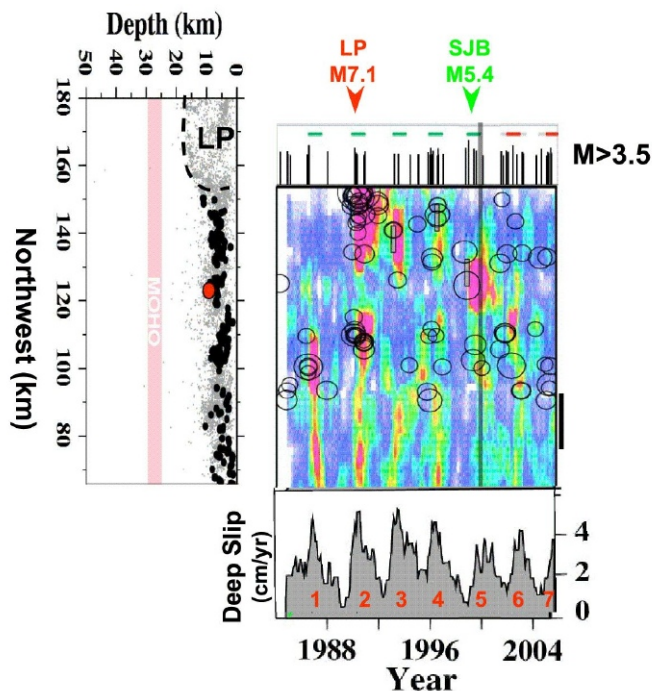


Figure 3.4: (Left) Along fault depth section of background seismicity (gray points) and SAF CS locations (black circles) for an 80 km segment of the central SAF. Rupture zone of the 1989, M7.1 Loma Prieta earthquake is labeled LP. (Right, center) Profile of the 1984-2005.25 deep slip history for the segment from the CS data. Rates (in color) are in percent difference from the 1984-2005.25 average. Color intensity give 95% confidence bounds. Open circles are along fault locations and times of  $M > 3.5$  earthquakes. Their sizes are keyed to relative magnitudes, but are significantly larger than their actual rupture dimensions. Vertical gray line is start time of the extended analysis. (Right, bottom) Deep slip rates history for a representative 15 km sub-segment showing the 7 pulses (labeled 1 through 7) observed to date. (Right, top) Occurrence times and magnitudes of the  $M > 3.5$  earthquakes in the 80 km zone. Time of Loma Prieta and San Juan Bautista events are labeled at top (LP and SJB, respectively). Horizontal green bars are pulse onset periods before 2000. Horizontal red bars are predicted pulse onset periods based on the green bars. Gray extensions of the red bars are prediction uncertainties.

(Figure 3.4), suggests that significant potential for refinement of time-dependent earthquake forecasts models exists for this area (WGCEP, 1999) on time scales comparable to the average pulse cycle duration of  $\sim 3$  years.

## 2.5 Acknowledgements

Thanks are given to Roland Bürgmann and Mark H. Murray for stimulating conversations and insightful comments regarding this work. This research was supported by the National Science Foundation through award EAR-0337308.

## 2.6 References

Dieterich, J.H., A model for the nucleation of earthquake slip, in *Earthquake Source Mechanics*, S. Das, J. Boatwright, and C.H. Scholz (Editors), *American Geophysical Monograph 37*, American Geophysical Union, Washington, D.C., 37-47, 1986.

Gwyther, R.L., C.H. Thurber, M.T. Gladwin, and M. Mee, Seismic and Aseismic Observations of the 12th August 1998 San Juan Bautista, California, M5.3 Earthquake, in *Proceedings of the 3rd Conference on tectonic problems of the San Andreas Fault system*, G. Bokelmann and R. Kovach, Eds., *Stanford California School of Earth Sciences, Stanford University*, 2000.

Nadeau, R.M., and T.V. McEvilly, Fault slip rates at depth from recurrence intervals of repeating microearthquakes. *Science*, 285, 718-721, 1999.

Nadeau, R. M. and T. V. McEvilly, Periodic Pulsing of Characteristic Microearthquakes on the San Andreas Fault, *Science*, 303, 220-222, 2004.

Working Group on California earthquake Probabilities (WGCEP). Earthquake probabilities in the San Francisco Bay Region: 2000 to 2030—a summary of findings, *U.S. Geol. Surv. Open-File Rept. 99-517*, 36 pp., 1999.

## 3. Monitoring Nonvolcanic Tremor on the San Andreas Fault

Robert M. Nadeau

### 3.1 Introduction

Nonvolcanic tremor activity (i.e., long-duration seismic signals with no clear P or S waves (Figure 3.5) may provide important clues to the rheology and processes responsible for the nucleation and seismic cycles of large earthquakes. Previously, nonvolcanic tremors had only been observed in subduction zones (i.e., thrust fault plate boundaries) (e.g., *Obara, 2002; Rogers and Dragert, 2003*), where fluids from subduction processes were believed to play an important role in generating these tremors.

### 3.2 SAF Tremors

Because subduction has not occurred along the central San Andreas Fault (SAF) for several million years, fluids from active subduction are not present, and nonvolcanic tremor activity was not expected along the the central SAF zone.

Recently, however, data from Berkeley's borehole High Resolution Seismic Network (HRSN) at Parkfield, California revealed tremor-like signals originating in the vicinity of Cholame, California (*Nadeau and Dolenc, 2005*). The tremors appear to be confined largely to an 25 km segment of the SAF beneath Cholame at depths of between 20 to 40 km. The depths, frequency content (generally 1 to 10 Hz), S-wave propagation velocity, and waveform character of the SAF tremors were similar to those of the subduction zone tremors; however, the SAF tremors are less frequent, of shorter duration, of smaller amplitude, and of lower seismic energy release.

Our discovery of these nonvolcanic tremors is important for three reasons: 1) they occur along a transform rather than a subduction plate boundary zone, 2) no obvious source for fluid re-charge exists in the Cholame area to aid in tremor genesis, and 3) the highest level of tremor activity in the region occurs beneath the inferred epicentral region of the moment magnitude (M)  $\sim 7.8$  1857 Fort Tejon earthquake, whose rupture zone is currently locked.

The Cholame segment of the SAF has an estimated earthquake recurrence time of 140 years (+93, -69) (*WGCEP, 1995*), and it is now over 140 years since the Fort Tejon event. Because stress changes from ETS events may trigger large earthquakes, future increases in SAF tremor activity may signal periods of increased probability for the next large earthquake on the segment.

An apparent correlation between tremor and local micro-earthquake rates at Cholame (*Nadeau and Dolenc, 2005*) also suggests that deep deformation associ-

ated with the Cholame tremors (i.e., ETS) may also be stressing the shallower seismogenic zone in this area.

Further evidence for stress-coupling between the deep tremor zone and the seismogenic SAF is observed in the correlation between tremor and the 28 September 2004, M6 Parkfield earthquake ( $\sim 10$  km NW of Cholame) (Figure 3.6). Between 1 and 3 months before the Parkfield earthquake, tremor activity was extremely low. Then 20 to 22 days prior to the Parkfield quake, tremor activity showed an anomalously large rate of activity (fore-tremor). This is consistent with the observations of *Nadeau and Dolenc (2005)*, which suggest a relationship between the deep tremor and shallower seismogenic zones in which stress changes in one of these zones induces stress changes in the other with a lag time of a few weeks.

Immediately following the Parkfield mainshock an even larger rate increase in tremor activity occurred, and elevated tremor rates persisted for over 500 days. This elevated rate appears now to have subsided and tremor rates are again low. It is too early to say whether or not the low activity rates now being observed are representative of another precursory quiescent period, but given the critical location of the tremors relative to the Fort Tejon locked zone, and the evidence for coupling of tremor rates and earthquake activity seen so far, we are compelled to continue monitoring the tremors for signs of anomalous activity that may signal an increased likelihood for another large event in the area.

### 3.3 Acknowledgements

This research was supported by U.S. Geological Survey award no. 06HQGR0167.

### 3.4 References

- Nadeau, R.M. and D. Dolenc, Nonvolcanic Tremors Deep Beneath the San Andreas Fault, *Science*, 307, 389, 2005.
- Obara, K., Nonvolcanic Deep Tremor Associated with Subduction in Southwest Japan, *Science*, 296, 1679-1681, 2002.
- Rogers, G. and H. Dragert, Episodic Tremor and Slip on the Cascadia Subduction Zone: The Chatter of Silent Slip, *Science*, 300, 1942-1943, 2003.
- Working Group on California Earthquake Probabilities (WGCEP), Seismic hazards in southern California: probable earthquakes, 1994 to 2024, *Bull. Seism. Soc. Am.*, 85, 379-439, 1995.

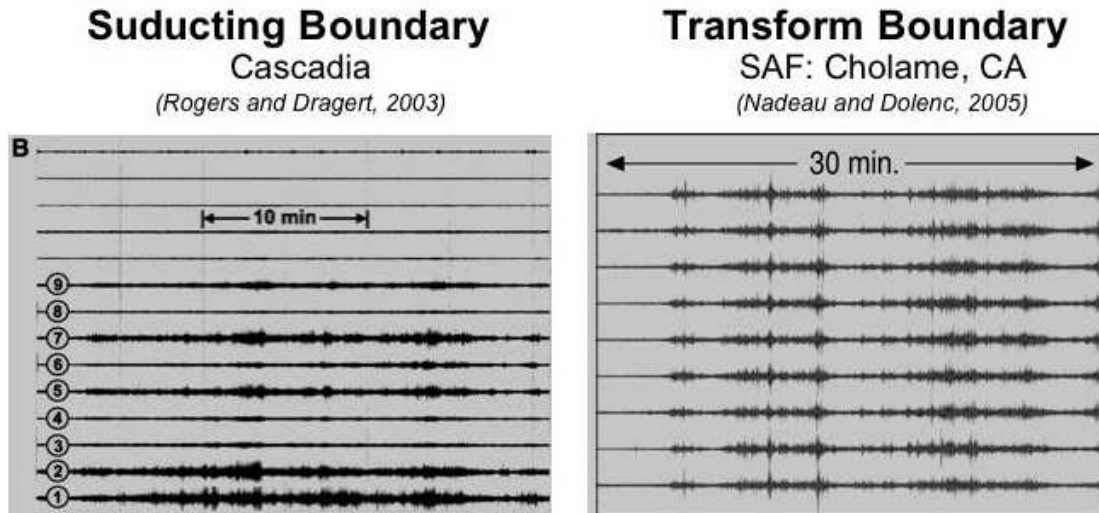


Figure 3.5: Comparison of Cascadia and San Andreas Fault Tremors. In Cascadia, a significant correlation between subduction zone tremor activity and subseismogenic zone (i.e. beneath the upper  $\sim 15$  km of Earth's crust where earthquakes occur) slow slip events (referred to as episodic tremor and slip (ETS, *Rogers and Dragert, 2003*)) has been observed, suggesting that stress changes from ETS events may increase stress and possibly trigger earthquakes in the shallower seismogenic fault zone. No correlation between tremor and deformation changes have yet been observed along the SAF, however, variations in earthquake activity does correlate.

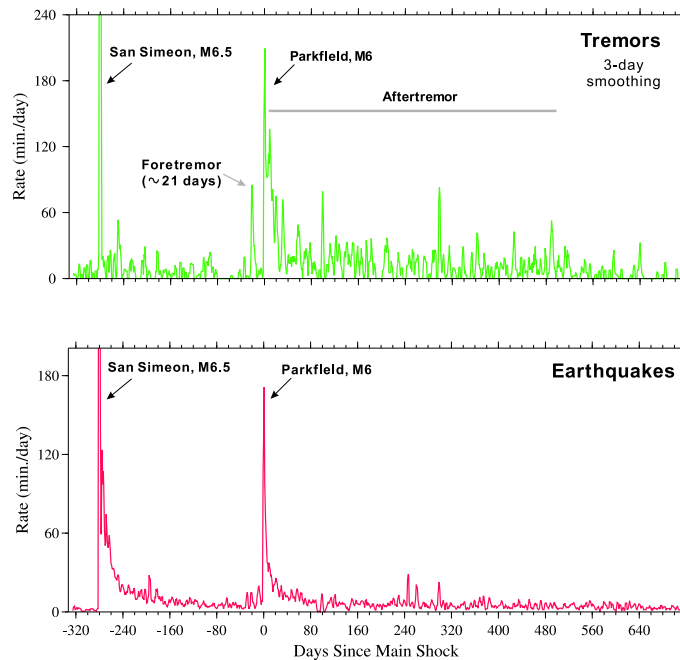


Figure 3.6: Activity rate history of nonvolcanic tremors (green, top) and microearthquakes (red, bottom) detected by the borehole High Resolution Seismic Network (HRSN) at Parkfield, CA. History spans 40 days prior to the San Simeon Earthquake through Sept. 13, 2006 (i.e., 716 days after the Parkfield mainshock). Tremor activity rates were not strongly influenced by the San Simeon event that occurred some 50 km to the west. However, the Parkfield earthquake whose epicenter was about 10 km from the tremor zone had a strong impact. Parkfield aftershocks decayed more rapidly than the tremor activity, suggesting some lag between stress changes in the deep tremor zone relative to that in the seismogenic zone above.

## 4. Repeating Earthquakes on an Imbricated Thrust Fault in the Arc-Continent Collision Boundary of Eastern Taiwan

Kate H. Chen (National Cheng Kung University), Robert M. Nadeau, and Ruey-Juin Rau (National Cheng Kung University)

### 4.1 Introduction

The Chihshang fault in eastern Taiwan, characterized by  $\sim 3$  cm of surface slip per year, is one of the most rapidly creeping thrust faults known in the world (*Angelier et al.*, 2000; *Lee et al.*, 2003). Other than a recent ML 6.4 earthquake on the Chihshang fault on 10 December 2003, and a ML 6.0 earthquake in 1951, no significant earthquakes are known to have occurred on this fault. Strike-slip faults that produce both large earthquakes and near surface creep have been studied (i.e., the Hayward fault in central California). They are believed to have zones of locked and creeping fault at depth and only creep near the surface (*Savage and Lisowski*, 1993; *Bürgmann et al.*, 2000). In contrast, the Chihshang fault exhibits mainly by reverse slip and may, therefore, have greater overall strength. However, due to limited geodetic coverage and difficulties in obtaining deformation information from Interferometric Synthetic Aperture Radar (InSAR) in the area (*Hsu and Bürgmann*, 2006), the picture of slip at depth on the Chihshang fault is poorly resolved, and the distribution of locked and creeping fault at depth is, therefore, difficult to determine. A technique for inferring fault slip rate at depth using repeating microearthquakes has recently been developed (*Nadeau and McEvilly*, 1999; *Nadeau and Johnson*, 1998) and has been applied in a variety of tectonic settings. Because the Chihshang fault has many small quakes and is creeping, it may also generate repeating earthquakes. In this study, we search for repeating earthquakes and characterize their behavior in space and time, and use this information to develop a conceptual model of the Chihshang fault.

### 4.2 Data

We used 3387 earthquakes from the Central Weather Bureau Seismic Network (CWBSN) catalog in our analysis. The events occurred in the Chihshang fault region between 01 January 1991 and 9 December 2003, the day before the 6.4 ML earthquake. The relatively sparse, one-sided coverage of the CWBSN stations in the Chihshang area coupled with poor noise characteristics, complicate the task of defining complete and accurate repeating event sequences in the region. To resolve this problem, we use the threshold criteria in S-P differential time and waveform similarity to identify repeating earthquakes in the Chihshang area.

### 4.3 Spatial distribution of repeating earthquakes

Using time waveform similarity criteria, we identify 113 repeating events in the Chihshang fault zone, about 3% of the M1.9 to 5.4 earthquakes from the study period. They are organized into 31 repeating sequences with magnitudes ranging from 1.9 to 3.7. Fig. 1 shows examples of the waveforms for one repeating sequence. Locations of the 31 repeating sequences are shown in Fig. 2. All the sequences occur between depths of 7 to 23 km, and tend to concentrate on the northern section of the fault segment.

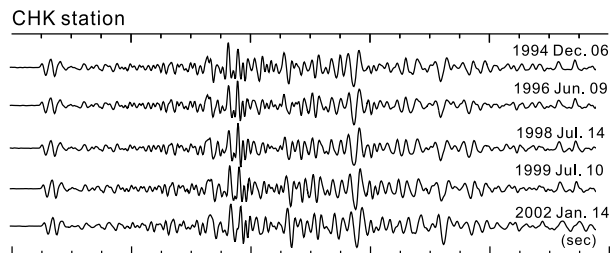


Figure 3.7: Waveforms recorded at station CHK from one of the 31 repeating sequences. Each trace was normalized by its maximum amplitude.

### 4.4 Deep slip rates

To study the spatial distribution of fault-slip rates, we first compute the sum of slip loads for each sequence site. These sums were then divided by the corresponding sums of recurrence intervals for the sequences, giving the average deep slip rate surrounding each sequence during the study period. The results of deep slip rates are shown in Fig. 2. The slip rate estimates range from 2.0 - 7.9 cm/yr with an average of 4 cm/yr. The coefficient of variation in the slip rates is 0.33. The highest slip rates (above 6 cm/yr) are found on the deep portion of the fault, between 18 and 20 km. Slip rates of less than 3 cm/yr are found above 15 km depth. However, overall slip rates estimates do not reveal a systematic depth-dependent behavior. In the upper panel of Fig. 2, we compare the along-strike variation of deep slip rates with surface observations. The GPS data shown by black dots are a combination of the average uplift rate from 1985-1994 leveling data and horizontal deformation rate from 1992-1999 GPS data (*Liu and Yu*, 1990; *Yu and Kuo*, 2001).

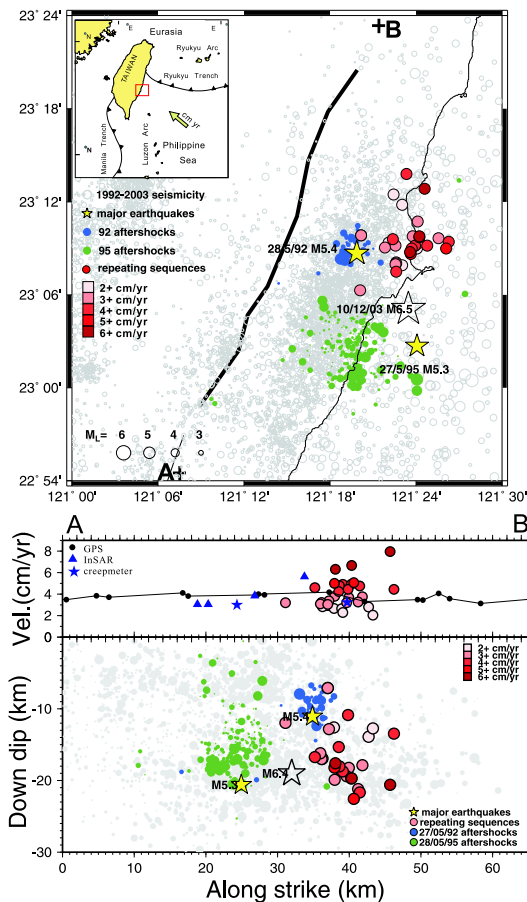


Figure 3.8: The spatial distribution of repeating sequence derived slip rates in mapview (top) and along-strike cross-section (bottom). Filled circles with a black rim represent locations of repeating sequences. Fill colors/shades are keyed to the slip rates. Yellow stars indicate major events occurred during the study time period from 1992 - 2003 December. Open star indicates the event that occurred on 10 December 2003 just after the study period. Background seismicity are shown as gray circles. Aftershock sequences from the 1992 and 1995 M5+ events are shown as blue and green circles without a rim, respectively. (Bottom) Filled circles with a black rim in the upper panel indicate a projection of repeaters on the along-strike distance and their corresponding slip rates. Black dot shows a combined surface slip rates from GPS and leveling data measurement. Blue solid triangles and stars are along-dip projection of InSAR data (Hsu and Bürgmann, 2006) and creepmeter data (Lee et al., 2003), respectively. See color version of figure at front of Research Studies.

The InSAR data (Hsu and Bürgmann, 2006) and creep-meter data (Lee et al., 2003) are projected into along-dip direction assuming a fault dip angle of 60 at near surface. The above surface measurements are consistent with the deep repeating earthquake slip rates ( $\sim 4$  cm/yr).

## 4.5 Conclusion

The Chihshang repeating sequences are concentrated on the northern half of the Chihshang fault zone at 7 - 23 km depth. Their average deep slip rate, 4 cm/yr, are consistent with three types of geodetic measurements at surface. We, therefore, infer the contrasting deep fault slip behavior from north to south on the Chihshang fault. The northern segment is likely creeping and southern segment is likely locked with higher earthquake potential.

(Kate Chen has been a visiting scholar in BSL since March 2006)

## 4.6 References

- Angelier, J., H. T. Chu, J. C. Lee, and J. C. Hu, Active faulting and earthquake hazard: the case study of the Chihshang Fault, Taiwan, in *J. Geodyn.*, 29, 151 - 185, 2000.
- Bürgmann R., D. Schmidt, R. M. Nadeau, M. d'Alessio, E. Fielding, D. Manaker, T. V. McEvelly, and M. H. Murray, Earthquake potential along the Northern Hayward Fault, California, in *Science*, 289, 1178-1182, 2000.
- Hsu, L and R. Bürgmann, Surface creep along the longitudinal Valley fault, Taiwan from InSAR measurements, in *Geophys. Res. Lett.*, 33, doi:10.1029/2005GL024624, 2006.
- Lee, J. C., J. Angelier, H. T. Chu, J. C. Hu, F. S. Jeng, and R. J. Rau, Active fault creep variations at Chihshang, Taiwan, revealed by creep meter monitoring, 1998-2001, in *J. Geophys. Res.*, 108, doi:10.1029/2003JB002394, 2003.
- Liu, C. C., and Yu, S. B., Vertical crustal deformations in eastern Taiwan and its tectonic implications, in *Tectonophysics*, 183, 111-119, 1990.
- Nadeau, R. M. and L. R. Johnson, Seismological studies at Parkfield VI: moment release rates and estimates of source parameters for small repeating earthquake, in *Bull. Seism. Soc. Am.*, 88, 790 - 814, 1998.
- Nadeau, R. M. and T. V. McEvelly, Fault slip rates at depth from recurrence intervals of repeating microearthquakes, in *Science*, 285, 718-721, 1999.
- Savage, J. C., M. Lisowski, Inferred depth of creep on the Hayward fault, central California, in *J. Geophys. Res.*, 98, 787 - 793, 1993.
- Yu, S. B. and L. C. Kuo, Present-day crustal motion along the Longitudinal Valley Fault, eastern Taiwan, in *Tectonophysics*, 333, 199-217, 2001.

# 5. Subsurface Creep From Repeating Earthquakes at the Juncture of the San Andreas and Calaveras Faults

Dennise Templeton, Robert Nadeau, and Roland Bürgmann

## 5.1 Introduction

We investigate fault creep at depth at the juncture of the San Andreas and Calaveras faults using repeating earthquake data from 1984 to 2005. We are interested in studying how creep is partitioned as a fault system transitions from having a single fault accommodate slip to having multiple, sub-parallel fault strands accommodate slip. In the San Francisco Bay Area, the juncture between the San Andreas fault and the Calaveras fault illustrates such a transition. This juncture region is highly complex as the seismically active portions of the Calaveras fault do not illuminate a straight, contiguous fault plane. Additionally, a shorter secondary fault structure, the Quien Sabe fault zone, is more seismically active than the neighboring Calaveras fault. If repeating earthquakes also occur on the Quien Sabe fault zone, this could suggest that this fault is accommodating, at least at depth, some of the total slip associated with the plate boundary.

## 5.2 Methodology and Results

We identify repeating earthquake sequences by cross-correlating the first 5 seconds of local event waveforms recorded by the Northern California Seismic Network at the surface. Pairs of events which have a cross-correlation coefficient greater than 0.90 are then visually inspected for quality assurance and identified as belonging to the same repeating earthquake sequence. By using this methodology in our study area, we identified 99 repeating earthquake sequences. Repeating sequences were found on all three faults within the study area.

Assuming that these sequences represent a stuck patch in an otherwise creeping fault, we employ the empirical formula of *Nadeau and McEvilly (1999)* to determine the total amount of fault slip at each sequence location by using the number of times a sequence repeats and the average moment magnitude of the repeating sequence as inputs (Figure 3.9). Filled circles indicate the hypoDD location and amount of total slip in centimeters associated with the repeating sequence. Open circles indicate the catalog location of a repeating earthquake sequence not included in the hypoDD relocated dataset. The amount of total slip at a small number of repeating earthquake locations along the southern portion of the Quien Sabe fault zone was greater than 25 cm over the observation period, comparable to total slip amounts along portions of the San Andreas fault. The number of times an earthquake repeats in a sequence depends on a number of factors, including the background loading rate

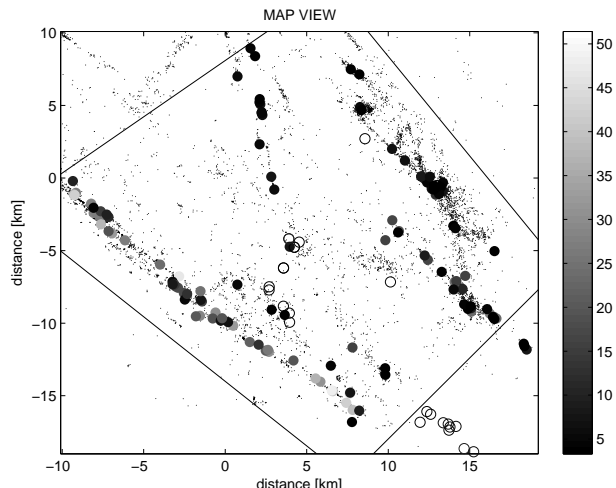


Figure 3.9: Map view of San Andreas fault on the left, Calaveras fault in the middle, and Quien Sabe fault zone on the right. HypoDD relocated background seismicity as small black dots. Filled circles indicate the hypoDD location and amount of total slip in centimeters associated with a repeating earthquake sequence. Open circles indicate the catalog location of a repeating earthquake sequence not included in the hypoDD relocated dataset.

of the fault. This explains why, in general, sequences on the San Andreas fault repeat more often or have greater moment magnitudes, and thus greater amounts of total slip, than sequences on the Calaveras or Quien Sabe fault zone. Preliminary results show that creep is as heterogeneous at depth as it appears on the surface. Locations of repeating earthquake sequences of significantly different total slip amounts can be located close to each other on the fault plane.

## 5.3 Acknowledgements

Special thank you to USGS-NEHRP for funding this project.

## 5.4 References

Nadeau, R. M. and T.V. McEvilly, Fault Slip Rates at Depth from Recurrence Intervals of Repeating Microearthquakes, *Science*, 285, 718-721, 1999.

## 6. Kinematic Modeling of the 2004 Parkfield Earthquake

Ahyi Kim and Douglas Dreger

### 6.1 Introduction

The September 28, 2004 Mw6.0 Parkfield earthquake (epcenter 35.815N, 129.374W and depth 8.1km) is probably the best recorded moderate sized earthquake to date. The regional broadband geodetic monitoring arrays, InSAR, as well as densely spaced local-distance strong motion instruments provide unprecedented coverage enabling detailed analysis of the kinematic rupture process. In-depth examination of kinematic rupture models, their resolution, and reconciliation with peak ground motion distribution is necessary for better understanding earthquake rupture physics as well as applications of such models for rapid ground motion hazard reporting.

### 6.2 Data

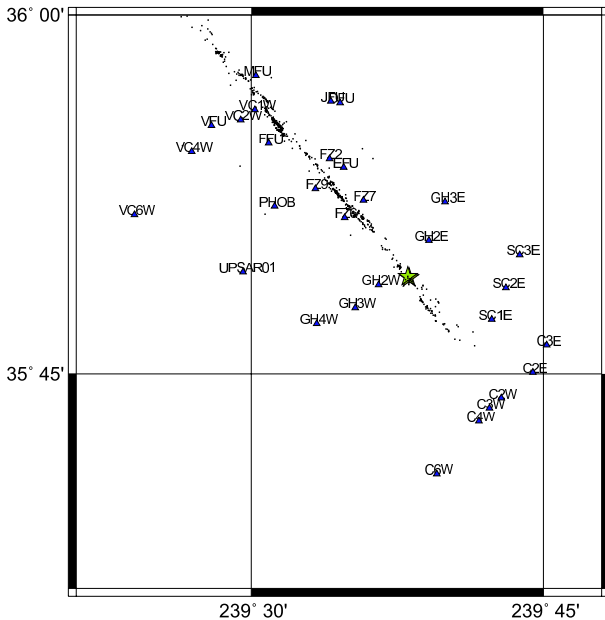


Figure 3.10: Location of the 2004 Parkfield earthquake. The near-fault strong motion stations are plotted as the triangles. Red star indicates the hypocenter and Black dots represents the aftershocks.

To obtain the kinematic model for 2004 Parkfield earthquake, we carried out a joint inversion combining the near-fault strong motion records and geodetic data sets. We used 60 near-fault horizontal-component strong motion records from 30 stations (Figure 1). Each record was integrated to velocity, band-pass filtered using a Butterworth filter with a corner frequency of 0.5 Hz, and re-sampled to 10 samples per second. The distance range

between the fault and the stations is 0.4-7.9km.

Coseismic GPS deformation from 13 sites was obtained from 1 sample per second GPS time histories. To obtain the coseismic deformation, the GPS time histories were averaged from 15 minutes before the event to 2-10 minutes afterward.

The coseismic deformation from ENVISAT InSAR data was obtained from a pre-event scene on 7/3/2003 and post event scene on 9/30/2004. We used the interferogram which was processed by Johanson *et al.* (in press). Johanson *et al.* removed the part of the interferogram affected by non-tectonic effects, especially atmospheric changes.

### 6.3 Inverse Method

For the inversion, we used the method of Harzell and Heaton (1983), which is a linear, multiple time window approach to invert the data for the spatio-temporal distribution of fault slip, the average rupture velocity and its variation, and the slip rise time. Green's functions for the seismic data were calculated using the FK integration method (Saikia, 1994) for frequencies up to 0.5 Hz with the two 1D velocity models reported in Liu *et al.* (2006), representing the velocity contrast across the SAF.

To generate the Geodetic green's function, we followed the method of Wang *et al.* (2003), assuming the GIL7 layered elastic structure model (Dreger and Romanowicz, 1994).

We assumed the fault plane dimension is 44kmx18km, which is divided into 1kmx1km subfaults. The rise time was allowed to vary from 0.6 sec to 3.6 sec, which is based on the preliminary regional distance results (Dreger *et al.*, 2005). The strike (140°) and dip (89°) were obtained from the aftershock distribution and some trial and error waveform fitting.

### 6.4 Inversion results

Figure 2a), 2b), and 2c) show slip models obtained from seismic, GPS, and InSAR data sets independently. They show some common features: (1) rupture propagated mainly to northwestward from the hypocenter, and (2) high slip value 10-20km northwest of the hypocenter. In detail, however, these three models are quite different. Basically, the inversion results from the geodetic data are dominated by the shallow slip northwest of hypocenter and some deep slip in southern part of the fault. The kinematic model obtained from the seismic only data shows much more complexity compared to those of geodetic data sets. The results using near-fault strong motion

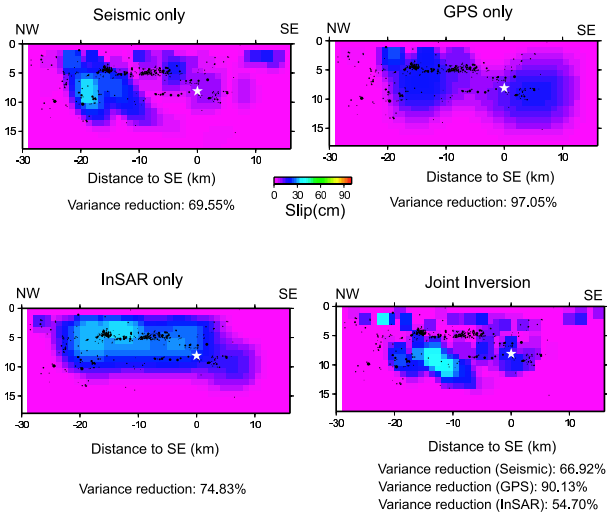


Figure 3.11: Slip models obtained independently from the a) seismic waveforms, b) GPS, and c) InSAR data sets. The model shown in d) compares the result when the three data sets are inverted simultaneously. These models are view NE and the left side is to the NW and the right to SE. The hypocenter is plotted as a white star. In the preferred model most of the slip is around hypocenter and between 10-20km NW of the hypocenter. After shocks are plotted as black dots. The x and y axes show along strike distance and depth in km. The slip located 10km to the SE is needed to fit the large amplitudes observed at the Cholame array.

data show a slip distribution that is consistent with what we obtained previously with the regional seismic waveform and near-fault GPS data in that there is a high slip patch at hypocenter and 10-20km north terminating near Middle Mountain ( Dreger *et al.*, 2005). This model also has some low levels of slip to the south that are needed to explain the waveforms and the high peak amplitudes at stations located south of the epicenter. Due to the non-uniqueness of this type of source inversion, it is important to obtain model that simultaneously fit different types of data. The joint inversion results are seen to show similarity with each of the independent inversions and the level of fit to each data set is acceptable.

The joint inversion and preferred model (Figure 2d) indicates a slight bilateral rupture, which is dominated by northward rupture. This model has two primary asperities: one near the hypocenter, and the other 10-20km northward of the hypocenter, which is consistent with our preliminary model with local and regional seismic and GPS data ( Dreger *et al.*, 2005). The best rupture velocity was found to be 2.6km/s, and the average rise time was 1.6 sec. The relatively higher slip in the InSAR only model might be due to included postseismic deformation, since the post-event scene is 2 days after the mainshock. In the preferred model, the scalar seis-

mic moment was found to be  $1.10 \times 10^{25}$  dyne-cm (Mw 6.03), while the peak slip was found to be 45.03cm. Slip model from the joint inversion showed us that the use of the geodetic data in the inversion places considerable additional constraint on the slip distribution.

## 6.5 References

- Dreger, D. S., and B. Romanowicz, Source characteristics of events in the San Francisco Bay region, *U. S. Geol. Surv. Open-File Rept.*, 94-176, 301-309, 1994
- Dreger, D., L. Gee, P. Lombard, M. Murray, and B. Romanowicz, Rapid Finite-source Analysis and Near-fault Strong Ground Motions: Application to the 2003 Mw 6.5 San Simeon and 2004 Mw 6.0 Parkfield Earthquakes, *Seis. Res. Lett.*, V.76, 40-48 2005
- ns: Application to the 2003 Mw 6.5 San Simeon and 2004 Mw 6.0 Parkfield Earthquakes, *Seis. Res. Lett.*, V.76, 40-48 2005 . Dreger D., Murray M., Nadeau R., and Kim A., Kinematic Modeling of the 2004 Parkfield Earthquake, *SSA 2005 annual meetin g abstract* 2005.
- Harzell, S. H. and T.H. Heaton, Inversion of strong ground motion and teleseismic waveform data for the fault rupture history of the 1979 imperial Valley, California earthquake, *Bull. Seism. Soc. Am.*, 73, 1553-1583 1983.
- Johanson, I., E. Fielding, F. Rolandone, and R. Burgmann, Coseismic and Postseismic Slip of the 2004 Parkfield Earthquake from Space-Geodetic data, *Bull. Seism. Soc. Am.*, (in press)
- Liu, P., S. Cautodiodo, and R. J. Archuleta, Kinematic Inversion of the 2004 Mw6.0 Parkfield Earthquake Including site effects, *Bull. Seism. Soc. Am.*, (in press)
- Saikia, C. K., Modified frequency-wave-number algorithm for regional seismograms using Filon's quadrature - modeling of L(g) waves in eastern North America, *Geophys. J. Int.*, 118, 142-158, 1994.
- Wang, R., F. Martin, and F. Roth, Computation of deformation induced by earthquakes in multi-layered elastic crust - FORTRAN programs EDGRN/EDCMP, *comp. Geosci.*, 29, 195-207 2003.

## 7. Identifying Isotropic Events Using an Improved Regional Moment Tensor Inversion Technique

Sean R. Ford, Douglas S. Dreger, William R. Walter (Lawrence Livermore National Laboratory)

### 7.1 Introduction

Identification of events with demonstrably significant non-double-couple components can aid in understanding the source processes of seismic events in volcanic and geothermal areas (e.g. *Dreger et al.*, 2000), and in nuclear event screening and possibly discrimination (*Dreger and Woods*, 2002). We implement the time-domain full regional waveform inversion for the complete moment tensor devised by *Minson and Dreger* (2006) after *Herrman and Hutchensen* (1993) based on the work of *Langston* (1981). The complete moment tensor allows for a characterization of the relative amounts of deviatoric and isotropic source components, the similarity of those components with prior events in the source region, and a constraint on the source depth. This information can aid in the discrimination of events.

### 7.2 Data and Methods

In general, synthetic seismograms are represented as the linear combination of fundamental Greens functions where the weights on these Greens functions are the individual moment tensor elements. Synthetic displacement seismograms are calculated with a frequency-wavenumber integration method (*Saikia*, 1994) for a one-dimensional (1-D) velocity model of eastern California and western Nevada (*Song et al.*, 1996). The synthetic data is filtered with a 4-pole acausal Butterworth filter between 0.02 and 0.05 Hz. At these frequencies, where the dominant wavelengths are approximately 100 km, we assume a point source for the low-magnitude ( $M_W \leq 5.6$ ) regional events investigated in this study. Data are collected from the TERRAScope network stations, ISA, PAS, and PFO. We remove the instrument response, rotate to the great-circle frame, integrate to obtain displacement, and filter similarly the synthetic seismograms.

We calibrate the algorithm by calculating the full and deviatoric moment tensor for the 1992 Little Skull Mountain event (Figure 3.12a). The deviatoric solution is obtained by constraining the trace of the moment tensor to be zero. Our result fits the data very well and is highly similar to the double-couple solution of *Walter* (1993), the deviatoric solution of *Ichinose et al.* (2003), and the full solution of *Dreger and Woods* (2002), where we assume a source depth of 9 km. The deviatoric component of the full moment tensor is decomposed to a double-couple and compensated linear vector dipole (CLVD) that shares the orientation of the major axis. The 1992

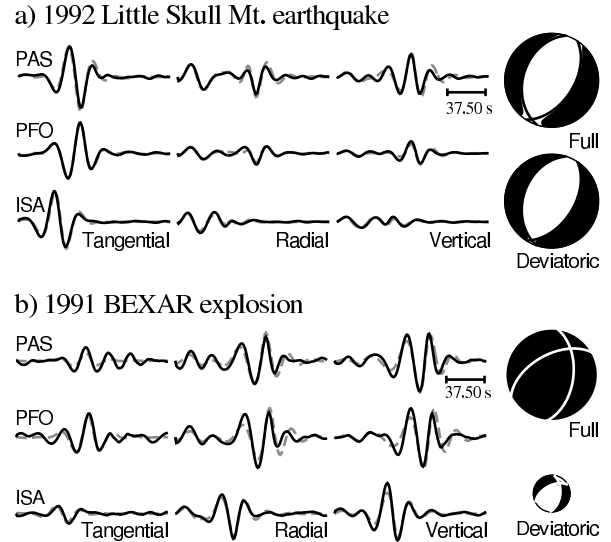


Figure 3.12: Moment tensor analysis of the (a) 1992 Little Skull Mt. earthquake and (b) 1992 BEXAR Nevada Test Site explosion. Data (solid line) and synthetics (dashed grey line) produced by inversion in the 20-50 s passband and resulting full and deviatoric (zero trace) focal spheres with best-fit double-couple planes (black lines), where the radius of the deviatoric sphere is relative to the total scalar moment contribution.

Little Skull Mountain event is almost purely double-couple and there is little change between the full and deviatoric solutions. The best-fit double-couple mechanism produces source parameters of strike  $35^\circ$  and  $196^\circ$ , rake  $-78^\circ$  and  $-104^\circ$ , and dip  $50^\circ$  and  $42^\circ$ , for the two focal planes, respectively. The total scalar moment ( $M_0$ ) is  $2.92 \times 10^{24}$  dyne-cm, which results in an  $M_W$  of 5.58.

With the same algorithm we calculate the full and deviatoric moment tensor for the 1991 Nevada nuclear test site explosion, BEXAR ( $m_b = 5.6$  and  $M_S = 4.2$ , NEIC; Figure 3.12b). The solution fits the data well and is similar to the full solution of *Minson and Dreger* (2006), where we assume a source depth of 1 km. The moment tensor has a large isotropic component, and the ratio of deviatoric moment ( $M_{DEV}$ ) to isotropic moment ( $M_{ISO}$ ) is 0.65, where the  $M_0$  is  $4.79 \times 10^{22}$  dyne-cm ( $M_W$  of 4.39).  $M_{ISO}$  and  $M_{DEV}$  are defined according to *Bowers and Hudson* (1999) and  $M_0 = M_{ISO} + M_{DEV}$ .

It is difficult to grasp the source-type from the standard focal mechanism plot. Following the source-type

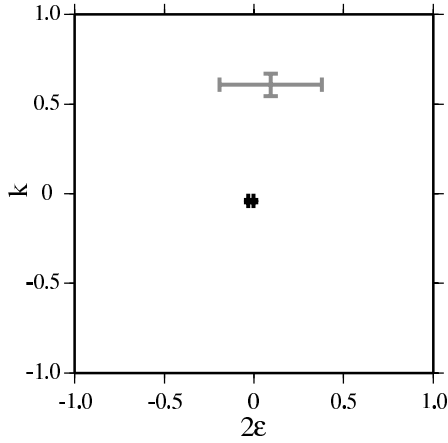


Figure 3.13: Source type plot for the 1992 Little Skull Mt. earthquake (black) and 1991 BEXAR NTS explosion (grey), with standard error (bars).

analysis described in *Hudson et al.* (1989) we calculate  $2\sigma$  and  $k$ , which are given by

$$\sigma = \frac{-m_1}{|m_3|},$$

and

$$k = \frac{M_{ISO}}{|M_{ISO}| + |m_3|},$$

where  $m_1$  and  $m_3$  are the deviatoric principal moments which are ordered  $|m_1| \leq |m_2| \leq |m_3|$ .  $\sigma$  is a measurement of the departure of the deviatoric component from a pure double-couple mechanism, and is 0 for a pure double-couple and  $\pm 0.5$  for a pure CLVD.  $k$  is a measure of the volume change, where +1 would be a full explosion and  $-1$  a full implosion.  $\sigma$  and  $k$  for the Little Skull Mountain earthquake and NTS explosion, BEXAR are given in Figure 3.13. Error in the values is derived from the standard error in the moment tensor elements given by the estimated covariance matrix obtained in the weighted least-squares inversion. Figure 3.13 shows that the Little Skull Mountain earthquake is within the error of being a perfect double-couple event ( $2\sigma = 0$ ) with no volume change ( $k = 0$ ). The BEXAR test, on the other hand, has a large volume increase with a large variance in the deviatoric source.

Error in the principal axes is analyzed by plotting the best-fit and scatter density of the axes of minimum compression (T), maximum compression (P) and null (N). The scatter density plot is obtained by randomly selecting moment tensor elements assuming a normal distribution for each element described by the standard error (given by the estimated covariance matrix), and diagonalizing the resulting moment tensor to obtain the principal axes. Principal axes plots for the Little Skull Mountain earthquake and NTS explosion, BEXAR are given

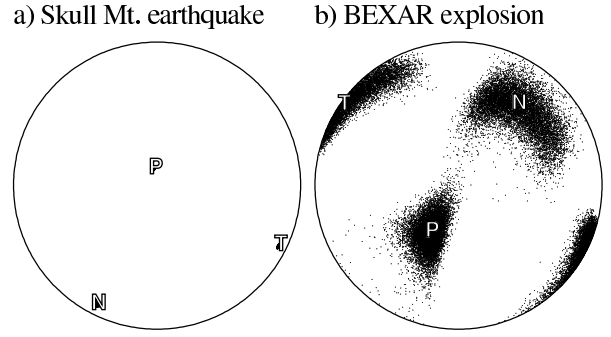


Figure 3.14: Scatter density of principal axes with best fit axes marked by the T, P, and N for the (a) Little Skull Mt. earthquake and (b) BEXAR explosion.

in Figure 3.14. The axes for the Little Skull Mountain event are well constrained, while those for the BEXAR test are more variable. However, the BEXAR test axes do not deviate greatly from the axes of the Little Skull Mountain event, which is likely due to the similar tectonic stresses.

In an effort to better characterize the source significance we adopt the source convention described in *Riedesel and Jordan* (1989). Vectors are defined describing the general,

$$MT = \sum_{i=1}^3 M_i \hat{M}_i,$$

double-couple,

$$DC = \hat{M}_1 - \hat{M}_3,$$

isotropic,

$$ISO = \sum_{i=1}^3 \hat{M}_i,$$

and CLVD sources,

$$CLVD1 = \hat{M}_1 - \frac{\hat{M}_2}{2} - \frac{\hat{M}_3}{2}; \quad CLVD2 = \frac{\hat{M}_1}{2} + \frac{\hat{M}_2}{2} - \hat{M}_3,$$

where  $\hat{M}_1$ ,  $\hat{M}_2$ , and  $\hat{M}_3$  are the T, N, and P axes, respectively, and  $M_1$ ,  $M_2$ , and  $M_3$  are the principal moments. The T, N, and P axes are chosen as in the double couple case, so that  $M_1 \geq M_2 \geq M_3$ . The source vectors are subspaces of the space defined by the principle axes of the moment tensor. The vectors are plotted on the focal sphere (similar to the T, N, and P axes) for the Little Skull Mountain earthquake and NTS explosion, BEXAR in Figure 3.15. The general source vector, MT, for the Little Skull Mountain event lies on the great-circle connecting the double-couple and CLVD sources. This great-circle defines the subspace on which MT must lie if the source is purely deviatoric. The MT vector is also collinear with the DC vector, which is to say that

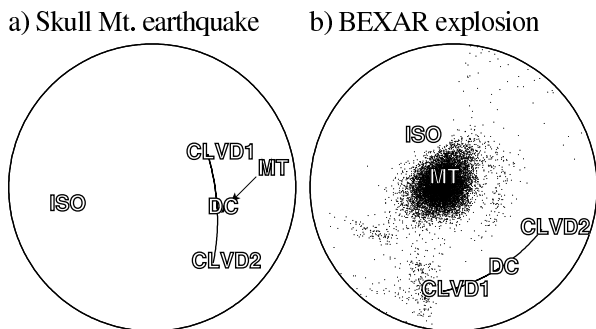


Figure 3.15: Source vector plot with density plot of general source vector, MT, for the (a) Little Skull Mt. earthquake and (b) BEXAR explosion. See text for definition of vectors. The great-circle line connecting the CLVD1, DC, and CLVD2 vectors defines the purely deviatoric solution space.

the source is almost purely double-couple. The MT vector for the BEXAR test lies well off the line defining the deviatoric solution space. The scatter density of possible MT vectors is also plotted and none of them intersect the deviatoric solution space, which is to say that the solution has a significant isotropic component.

## Discussion and Conclusions

The 1992 Little Skull Mountain event is a well-constrained, highly double-couple earthquake with an  $M_W$  of 5.6. The 1991 NTS nuclear test, BEXAR ( $m_b=5.6$  and  $M_S=4.2$ , NEIC), has a significant positive isotropic component with an  $M_W$  of 4.4. The deviatoric components of both events may be responding to the same general Basin and Range stress field of NW-SE extension. Analysis of  $\sigma$  versus  $k$  and the source vectors described above allows for an interpretation of the source with error. There are several sources of error in the moment tensor inversion, and the probabilistic method used in this study has the ability to incorporate those sources and produce empirical probability densities of the analyzed parameters (i.e.,  $\sigma$ ,  $k$ , and the source vectors). For example, several velocity models could be used to create the Greens functions for the linear inversion. Each of the moment tensor solutions and their associated scatter density could then be plotted as in Figures 4-6. These types of plots would aid in the understanding of how parameterization choice nonlinearly affects the moment tensor solutions, and help map the solution space of best-fit moment tensors.

The analysis presented here shows that high quality solutions can be obtained for sparsely-recorded events at regional distances, and that these solutions have the potential to discriminate between volume changing (explosions) and double-couple (earthquakes) sources. In the

future, we will test the sensitivity of the inversion to noise and non-ideal station spacing. We will also increase the population of moment tensors for man-made and natural events that deviate from the well recorded, large magnitude, small tectonic release cases presented here. Only an analysis of a wide range of events in different environments will allow for a true comparison of explosion and earthquake moment tensor populations.

## 7.3 Acknowledgements

Figures were made with Generic Mapping Tools (*Wessel and Smith, 1998*). This research is sponsored by the Department of Energy through the National Nuclear Security Administration, Office of Nonproliferation Research and Development, Office of Defense Nuclear Nonproliferation.

## 7.4 References

- Bowers, D. and J. A. Hudson, Defining the scalar moment of a seismic source with a general moment tensor, *Bull. Seism. Soc.*, 89(5) 1390-1394, 1999.
- Dreger, D., and B. Woods, Regional distance seismic moment tensors of nuclear explosions, *Tectonophysics*, 356(1-3) 139-156, 2002.
- Dreger, D., H. Tkalic, and M. Johnston, Dilational processes accompanying earthquakes in the Long Valley Caldera, *Science*, 288 122-125, 2000.
- Herrmann, R. B., and K. Hutchensen, Quantification of  $m_{Lg}$  for small explosion, *Phillips Laboratory Report PL-TR-93-2070*, 1993.
- Hudson, J. A., R. G. Pearce, and R. M. Rogers, Source type plot for the inversion of the moment tensor, *J. Geophys. Res.*, 94(B1) 765-774, 1989.
- Ichinose, G. A., J. G. Anderson, K. D. Smith, and Y. Zeng, Source parameters of Eastern California and Western Nevada earthquakes from regional moment tensor inversion, *Bull. Seism. Soc.*, 89 XX-XX, 2003.
- Julian, B.R., A. D. Miller, and G. R. Foulger, Non-double-couple earthquakes 1: Theory, *Rev. Geophys.*, 36 525-549, 1998.
- Langston, C. A., Source inversion of seismic waveforms: The Koyna, India, earthquakes of 13 September 1967, *Bull. Seism. Soc. Am.*, 71(1) 1-24, 1981.
- Minson, S. and D. Dreger, Improved seismic moment tensor inversion, to be submitted to *Geophys. J. Int.*, 2006.
- Riedesel, M. A., and T. H. Jordan, Display and assessment of seismic moment tensors, *Bull. Seism. Soc.*, 79(1) 85-100, 1989.
- Saikia, C. K., Modified frequency-wavenumber algorithm for regional seismograms using Filon's quadrature: modelling Lg waves in eastern North America, *Geophys. J. Int.*, 118 142-158, 1994.
- Sileny, J., G. F. Panza, and P. Campus, Waveform inversion for point source moment tensor retrieval with

variable hypocentral depth and structural model, *Geophys. J. Int.*, 109 259-74, 1992.

Song, X. J., D. V. Helmberger, and L Zhao, Broad-band modelling of regional seismograms: The basin and range crustal structure, *Geophys. J. Int.*, 125(1) 15-29, 1996.

Walter, W. R., Source parameters of the June 29, 1992 Little Skull Mountain earthquake from complete regional wave-forms at a single station, *Geophys. Res. Lett.*, 20(5) 403-406, 1993.

Walter, W. R., K. D. Smith, J. L. OBoyle, T. F. Hauk, F. Ryall, S. D. Ruppert, S. C. Myers, R. Abbot, and D. A. Dodge, An assembled western United States dataset for regional seismic analysis, *Lawrence Livermore National Laboratory Report, UCRL-TR-206630*, 2003.

Wessel, P. and W. H. F. Smith, New, improved version of generic mapping tools released, *Eos Trans. AGU*, 79 579 - 579, 1998.

## 8. 3D Simulations of Ground Motions of the 1989 Loma Prieta Earthquake Using the USGS SF06 Velocity Model

David Dolenc, Doug Dreger, and Shawn Larsen (LLNL)

### 8.1 Introduction

The United States Geological Survey has recently released an updated 3D velocity model (USGS SF06) of the greater San Francisco Bay Area that will be used to evaluate shaking hazard for possible future events in the region. In this study we used the 3D model and the 3D finite-difference code E3D (Larsen and Schultz, 1995) to simulate ground motions of the 1989  $M_w$  6.9 Loma Prieta event. Comparison of simulated ground motions with observations served to validate the velocity model for scenario studies of future large earthquakes in the region. This work was done as part of the SF06 Simulation Project Group modeling of the 1906  $M_w$  7.8 San Francisco earthquake (<http://www.sf06simulation.org>).

### 8.2 Modeling

The modeling of the great 1906 San Francisco earthquake for the event's 100th anniversary was one of the reasons for the USGS SF06 velocity model release. The model extends to 45 km depth and consists of a detailed model with approximate dimensions of  $290 \times 140$  km. This detailed model is nested inside an extended model which has approximate dimensions of  $650 \times 330$  km. The extended model was provided mainly to accommodate the 1906 San Francisco earthquake simulations and as a buffer zone for the simulations with either sources or stations close to the edge of the detailed model. The model's main improvement over the previous model versions is that more realistic material properties were assigned to individual geologic units (Brocher, 2005). Also, the model now includes topography and material properties of water for the Pacific Ocean and the San Francisco Bay.

To use the USGS SF06 model with the finite-difference code, we queried the model to extract values on a grid with a 125-m spacing. For the Loma Prieta earthquake, we employed Wald *et al.* (1991)'s strong motion and strong motion/teleseismic finite-source models. In addition, we used the Beroza (1991) strong motion finite-source model as a comparison. The dimensions of the simulation were  $220 \times 135 \times 50$  km and the grid spacing was 125 m. Because of computation limitations, the slowest velocities in the model were increased to a minimum S-wave velocity of 500 m/s, corresponding to a maximum modeled frequency of 0.8 Hz. In our simulations we included water (S-wave velocity 0.0 m/s), but not topography or attenuation. The computations were performed on the BSL Linux cluster. We compared re-

sults obtained with the three different finite-source models to observations. In addition, we compared the recent results to those obtained with the previous version of the USGS (ver. 2) and UCB velocity models (Stidham *et al.*, 1999) that had 250-m grid spacing and 1 km/s minimum S-wave velocity.

### 8.3 Results

Maximum horizontal velocity maps for the Loma Prieta simulations with the USGS SF06 velocity model and three different finite-source models are shown in Figure 3.16 (top). Results show strong NW directivity of the Wald *et al.* SM/T finite-source model. Amplification of the ground motions over the basins is well observed for all three models.

Recorded and synthetic waveforms at some of the stations that were included in the simulations are compared in Figure 3.16 (bottom). Velocity waveforms were low-pass filtered at 0.8 Hz. The traces from top to bottom are observations (gray), followed by the USGS SF06 velocity model synthetics for the three different finite-source models (Beroza, Wald SM/T, Wald SM). The results showed that the overall agreement between the USGS SF06 model simulations and the observations is very good. Comparison to the results obtained with the previous USGS (ver. 2) model and the UCB model showed that the results obtained with the new USGS SF06 model better matched the observations. Important differences between the results obtained with the three different finite-source models can also be observed. The results obtained for the Loma Prieta event as well as for other smaller events in the region (Dolenc *et al.*, 2006; Rodgers *et al.*, 2006) indicate that the remaining misfit between the simulations and the observations at some stations requires further model refinement.

### 8.4 References

- Beroza G. C. (1991). Near-source modeling of the Loma Prieta earthquake: Evidence for heterogeneous slip and implications for earthquake hazard, *Bull. Seism. Soc. Am.* 81, 1603-1621.
- Brocher, T. M., Compressional and shear wave velocity versus depth in the San Francisco Bay Area, California: Rules for USGS Bay Area Velocity Model 05.0.0, *U.S. Geol. Surv. Open-File Report 2005-1317*, 2005.
- Dolenc, D., D. Dreger, and S. Larsen, 3D simulations of ground motions in Northern California using USGS SF06 velocity model, *Seism. Res. Lett.*, 77, 300, 2006.

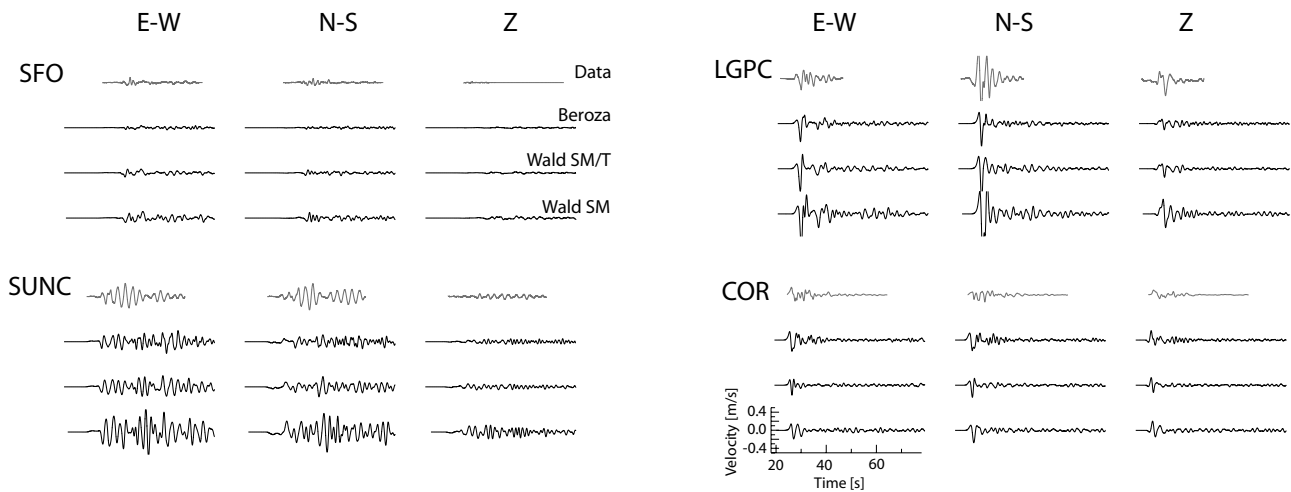
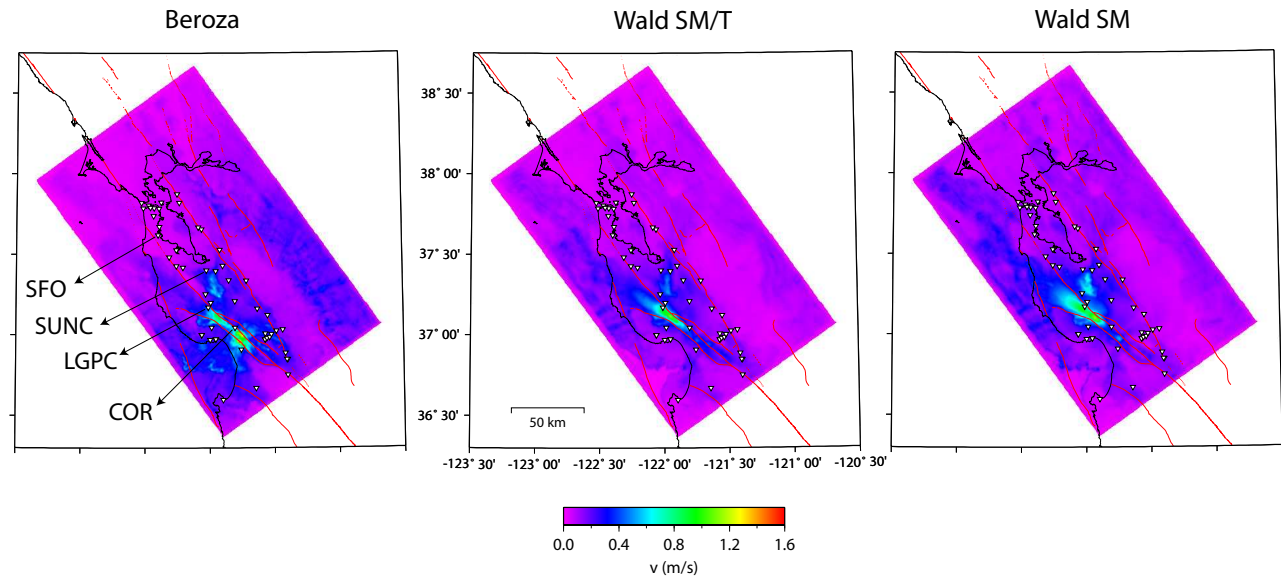


Figure 3.16: *Top*: Maximum horizontal velocity maps for the Loma Prieta simulations with the USGS SF06 velocity model and three different finite-source models. *Left*: Beroza (1991) strong motion model; *Center*: Wald et al. (1991) strong motion/teleseismic model; *Right*: Wald et al. (1991) strong motion model. *Bottom*: Recorded and synthetic waveforms at some of the stations that were included in the simulations. Velocity waveforms were lowpass filtered at 0.8 Hz. The traces from top to bottom are observations (gray), and USGS SF06 velocity model synthetics for the three finite-source models (Beroza, Wald SM/T, Wald SM).

Larsen S. and C. A. Schultz (1995). ELAS3D: 2D/3D elastic finite-difference wave propagation code, *Technical Report No. UCRL-MA-121792*, 19 pp.

Rodgers, A., A. Petersson, S. Nilsson, B. Sjogreen, and K. McCandless, Ground predictions using the USGS seismic velocity model of the San Francisco Bay Area: Evaluating the model and scenario earthquake predictions, *Seism. Res. Lett.*, 77, 281, 2006.

Stidham, C., M. Antolik, D. Dreger, S. Larsen, and B. Romanowicz, Three-dimensional structure influences on the strong-motion wavefield of the 1989 Loma Prieta

earthquake, *Bull. Seism. Soc. Am.*, 89, 1184-1202, 1999.

Wald D. J., D. V. Helmberger, and T. H. Heaton (1991). Rupture model of the 1989 Loma Prieta earthquake from the inversion of strong-motion and broadband teleseismic data, *Bull. Seism. Soc. Am.* 81, 1540-1572.

## 9. Toward Earthquake Early Warning in Northern California

Gilead Wurman and Richard M. Allen

### 9.1 Introduction

Although there have been recent advancements in the theory behind Earthquake Early Warning (EEW), there remain several challenges to the implementation of such EEW systems in Northern California. We have been working toward a functional EEW system since August 2005, and as of February 2006 an offline version of ElarmS (Earthquake Alarm System) has been running automatically, in a non-interactive fashion, following every event of  $M \geq 3$  in Northern California.

The non-interactive processing of these events has provided us with valuable data regarding the performance of ElarmS in real scenarios, particularly for events in and around the Bay Area. We present the statistical performance of this non-interactive processing, and discuss two specific events which reflect possible major earthquake scenarios.

### 9.2 Challenges of Northern California

Implementing EEW in Northern California presents specific challenges that have required improvements to the ElarmS methodology used in Southern California. We must integrate data from broadband velocity instruments and strong-motion accelerometers spread across two networks: the Northern California Seismic Network (NCSN) and the Berkeley Digital Seismic Network (BDSN). The disposition of stations in Northern California is shown in Figure 3.17.

The methodology by which ElarmS estimates an earthquake's magnitude relies in part on the measurement of maximum predominant period,  $\tau_p^{max}$  (Olson and Allen, 2005). However, this method is very susceptible to noise pollution, which is particularly problematic for events smaller than  $M \sim 4.5$ . To help constrain the magnitudes of small events, we have incorporated a second metric using the peak amplitude of either the displacement ( $P_d$ ) or velocity ( $P_v$ ) record following similar work in Taiwan (Wu, *et al.*, 2005). The linear average of the two metrics ( $P_d$  and  $\tau_p^{max}$  or  $P_v$  and  $\tau_p^{max}$ ) has proven to significantly improve our magnitude estimates for events of all sizes. The  $P_d$  or  $P_v$  metric is less susceptible to noise at low magnitudes, but tends to saturate at higher magnitudes. As  $\tau_p^{max}$  is susceptible to noise but not to saturation, the two metrics complement one another across all magnitudes.

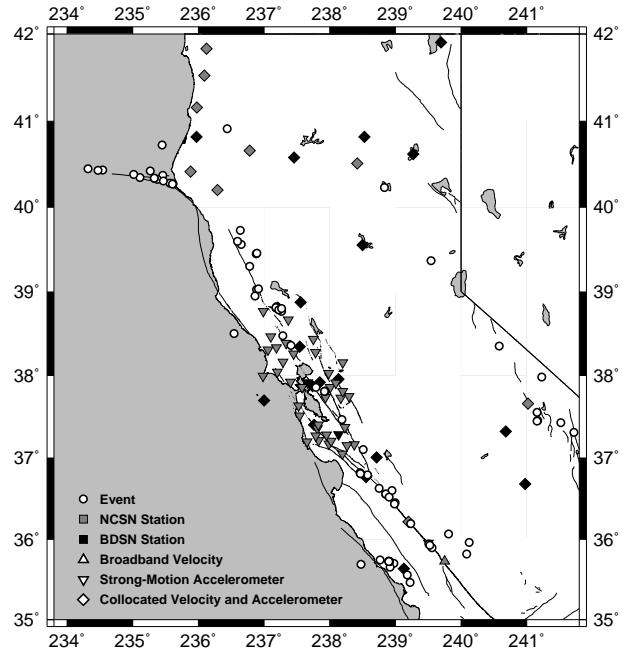


Figure 3.17: Map of Northern California showing NCSN and BDSN stations, and 68 events since February 2006.

### 9.3 Results of non-interactive processing

Since February of 2006, ElarmS has been running offline, in a non-interactive fashion (meaning with no human input or oversight), after every event in Northern California of  $M \geq 3$ . The processing is triggered automatically ten minutes after the event notification is received, to allow time for the necessary data to be recorded. Periodically, significant improvements to the ElarmS methodology are incorporated into the non-interactive processing. At that time all the events are reprocessed using the most current version of the code. The reprocessing is done using only the data available at the time of the initial processing, and is still performed non-interactively. Thus, while the reprocessed data does not reflect the fully automated performance of the system, it does reflect how the system would have performed, had the most current version of the code been in place at the time of the events.

As of this writing, a total of 70 instances of non-interactive processing have occurred. Of these, one is a duplicate event, due to the email notification system posting an update to an existing event. One instance was a false event. This was not the result of a false de-

tection by ElarmS, but of an erroneous email notification. The geographic distribution of the remaining 68 events is shown in Figure 3.17. Of these, one event was offshore Mendocino, with no stations within 100 km of the source, and two events suffered system-related processing errors (not resulting from the ElarmS code).

The remaining 65 events range in magnitude from  $M_d$  2.86 to  $M_L$  4.67. The results for these 65 events are presented in Figure 3.18. This figure shows the magnitude errors (with respect to network-based magnitudes, usually  $M_w$  or  $M_L$ ) produced by ElarmS at three different times for each event. The initial magnitude error refers to the magnitude estimation based on only the first second of p-wave data at the first station(s) to detect the event. This is the earliest possible magnitude determination, which can be used to give the maximum warning time. The initial magnitude has a significant scatter ( $\sigma \sim 0.8$  magnitude units) due to its reliance often on a single station's data.

The second plot in Figure 3.18 shows the errors at "alarm-time", which we define to be the time at which at least four seconds of p-wave data are available from at least four different channels. This definition is meant to reflect a confidence level in the magnitude which is sufficient to disseminate a public alarm. The magnitude error at this time is considerably less than in the first second ( $\sigma \sim 0.5$  magnitude units). Note that there are fewer events represented in this plot (42 events vs. 65 in the other plots), because not all of the events are ever detected in enough channels to meet the alarm criteria. This is primarily due to the weak signal from small ( $M \sim 3$ ) events, and in some cases results from a lack of enough stations within 100 km of the epicenter.

The lowermost plot in Figure 3.18 shows the error in the final magnitude determination for each event, using all available data from stations within 100 km of the source. Note that the scatter has increased over the previous plot ( $\sigma \sim 0.6$  magnitude units) due to the incorporation of events which did not meet the alarm criteria.

## 9.4 Two scenario events

Among the 65 events processed non-interactively by ElarmS, two moderate events represent likely hazardous earthquake scenarios for the Bay Area, and thus provide some insight into what can be expected of ElarmS in a real situation. For these two events we use  $M_L$  as a reference, even though  $M_w$  values exist for both. This is because  $M_L$  is sensitive to the same frequencies ( $\sim 1$ -2 Hz) as ElarmS, and because  $M_L$  is more directly related to the severity of the event in terms of damage to persons and property.

The first event is a  $M_L$  4.67 event near Gilroy, CA on 15 June, 2006. This event is located near the southern Calaveras fault, close to the likely epicenter of a Calaveras or Southern Hayward fault event. Figure 3.19 shows the

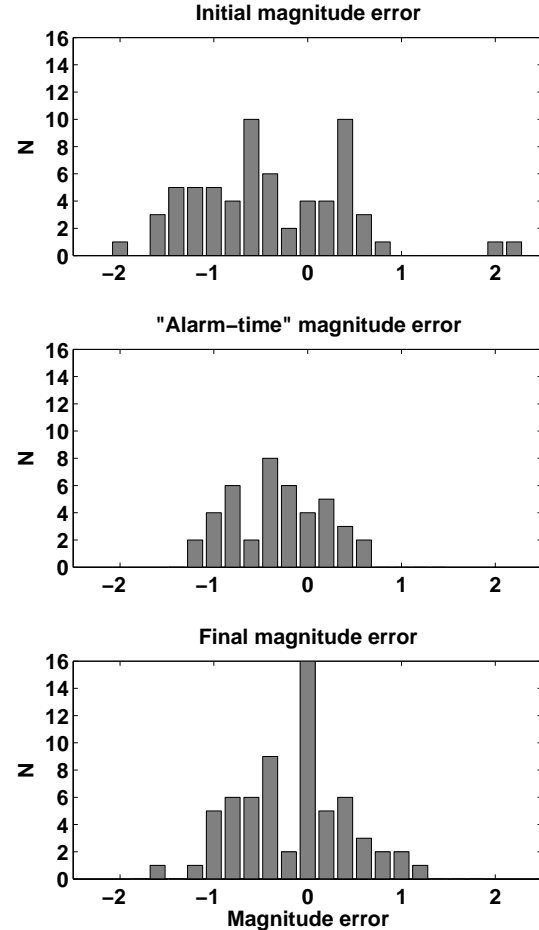


Figure 3.18: Magnitude errors from non-interactive processing. Top: magnitude estimate following first second of p-wave data. Middle: "alarm-time" magnitude error, using at least 4 seconds of p-wave data from 4 channels. Bottom: final magnitude error, using all available stations within 100 km.

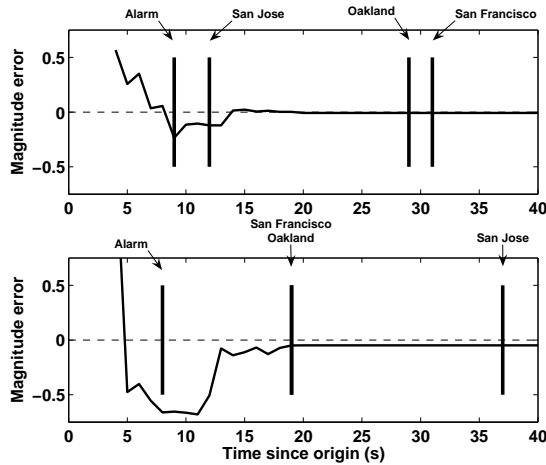


Figure 3.19: Plots of magnitude error vs. time for two representative events. Top:  $M_L$  4.67 Gilroy Earthquake of 15 June, 2006. Bottom:  $M_L$  4.7 Santa Rosa Earthquake of 2 August, 2006. Vertical bars represent (as notated) the “alarm time” for the event, or the time of arrival of severe ground motions at major urban centers in the Bay Area. Arrival times are based on a velocity of 3.55 km/s.

magnitude error vs. time for this event in relation to the arrival time of significant shaking at San Francisco, Oakland and San Jose.

Initial detection of this event by ElarmS occurred 3 seconds after origin, and the initial magnitude estimate was 5.2 one second later. The magnitude estimate came down over the following five seconds due to the incorporation of more data, until the alarm criteria were met at 9 seconds after origin. At that time, the magnitude estimate was 4.44, only 0.23 magnitude units below the actual  $M_L$ . The vertical lines on the plot represent the arrival of severe ground shaking at the three major urban centers in the Bay Area, based on a move-out of 3.55 km/s. San Jose experienced peak ground shaking only 12 seconds after event origin, meaning San Jose would have had about 3 seconds warning time in this event, not considering telemetry and dissemination delays. However, Oakland and San Francisco would have had 20 and 22 seconds of warning, respectively for this event. These warning times depend primarily on the disposition of stations around the epicenter, so they would be comparable for a magnitude 7 event.

The second scenario event is a  $M_L$  4.7 event near Santa Rosa on 2 August (local time), 2006. This event is located near the Rodgers Creek fault, near the likely epicenter of a southward-rupturing Rodgers Creek/Hayward fault event. The bottom plot in Figure 3.19 shows the history of this event in the same manner as above.

This event was initially detected 3 seconds after event origin. The initial magnitude, one second later, was rather high, at 6.4. This is a large error, which highlights the utility of waiting for more data to become available rather than issuing the alarm immediately. In the next second, the magnitude dropped to 4.2, and by the time the alarm criteria were met at 8 seconds after origin, the magnitude had dropped further to 4.0. At alarm time, both San Francisco and Oakland had 11 seconds until the arrival of severe ground shaking. However, the magnitude estimate at that time was low, and only rose to about 4.6 at 13 seconds after the origin, leaving only 6 seconds of warning for San Francisco and Oakland. San Jose experienced severe ground motions 37 seconds after origin, so even with the additional 5 second delay for the magnitude estimate to rise, it still had 24 seconds of warning in this instance.

The poor initial estimation of the magnitude of the latter event is primarily because most of the stations to the north of the Bay Area are NCSN strong motion stations, which are susceptible to noise pollution below  $M \sim 5$ . For large earthquakes this is not a problem, but in smaller events high-gain broadband velocity sensors yield superior data.

## 9.5 Conclusion

We are now beginning the process of moving ElarmS from the offline development stage to real-time testing at the Berkeley Seismological Laboratory. Based on its performance on 65 events in a non-interactive offline setting, we expect that ElarmS will perform well under real-time testing, without major modification from its present version.

## 9.6 Acknowledgements

We would like to thank Doug Neuhauser and Bob Uhrhammer for information and discussions related to station equipment and networks. This research was funded by USGS/NEHRP Grant #05HQGR0074.

## 9.7 References

- Olson, E.L. and R.M. Allen, The deterministic nature of earthquake rupture, *Nature*, 438, doi:10.1038/nature04214, 212-215, 2005.
- Wu, Y.-M., H.-Y. Yen, L. Zhao, B.-S. Huang, and W.-T. Liang, Magnitude determination using initial  $P$  waves: A single-station approach, *Geophys. Res. Lett.*, 33, doi:10.1029/2005GL025395, 2006.

# 10. Identifying and Removing Noise from the Monterey Ocean Bottom Broadband Seismic Station (MOBB) Data

David Dolenc, Barbara Romanowicz, Bob Uhrhammer, Paul McGill (MBARI), Doug Neuhauser, and Debra Stakes (MPC)

## 10.1 Introduction

The Monterey ocean bottom broadband station (MOBB) was installed in April 2002, 40 km offshore in the Monterey Bay, at a water depth of 1000 m, through a collaborative effort between the Monterey Bay Aquarium Research Institute (MBARI) and the Berkeley Seismological Laboratory (BSL; *Romanowicz et al., 2003*). The MOBB includes a 3-component Guralp CMG-1T broadband seismometer, a differential pressure gauge (DPG) and a current meter. Prior to the deployment, the seismometer system was extensively tested and insulated at the BSL to minimize the long-period noise due to the sensitivity of the instrument to air movement within the titanium pressure vessel. During the deployment, further steps were taken to minimize the background noise that could be generated by the flow of water around the pressure vessel housing the seismometers (*Uhrhammer et al., 2002; Dolenc et al., 2006*). The remaining long-period background noise observed at MOBB is primarily due to pressure forcing from the infragravity ocean waves (*Dolenc et al., 2005*). Infragravity waves are ocean surface waves in the frequency band between 0.002 and 0.05 Hz. Results from a previous study (*Dolenc et al., 2005*) showed that the long-period noise data recorded at MOBB can be used to better understand where and when the infragravity waves are generated. But for the study of seismic signals, additional processing is needed to remove the long-period noise from the MOBB data.

## 10.2 Background noise removal

To remove the long-period background noise from the MOBB data we employed two methods. In the first one we subtracted the simultaneously recorded ocean bottom pressure signal from the vertical seismic acceleration in time domain. The scale factor by which the pressure signal was multiplied was assumed to be frequency independent and was linearly estimated from the data. This method has previously been used to remove atmospheric pressure signal from the vertical seismic data recorded at land stations (*Zürn and Widmer, 1995*). Figure 3.20a,b shows that this method can also be used to remove long-period background noise from the ocean bottom seismic data. The presented results are for a 5.5-hour period for which the pressure signal was removed from the vertical seismic acceleration signal in time domain. The result is shown in frequency domain to illustrate the successful removal of the infragravity “hump”.

In the second approach we combined the pressure observations with measurements of the transfer function between vertical seismic and pressure recordings to predict the vertical component deformation signal. The predicted signal was then removed from the vertical seismic data in either frequency or time domain (*Crawford and Webb, 2000*). The transfer function was calculated from periods without earthquakes. Since it is only a function of structure at the MOBB location, it does not change with time and can be applied to all data from this site. Figure 3.20c-f shows an example of the transfer-function method to remove noise from the earthquake free vertical MOBB data. An example of the long-period background noise removal for a period that included an earthquake is shown in Figure 3.21a-d. The 1-hour period used in the calculation now included the 12/06/2004  $M_w$  6.8 Hokkaido, Japan event. The same transfer function as described above and shown in Figure 3.20d was used. The result shows that the method successfully recovers the seismic phases that were previously hidden by the long-period background noise and that the result is similar to the waveforms from the nearby land station SAO (Figure 3.21d).

## 10.3 Signal-generated noise removal

The other type of noise observed at MOBB is the signal-generated noise. It is due to reverberations of seismic waves in the shallow sedimentary layers and may be unavoidable in buried ocean bottom installations. It is particularly strong following the arrival of sharp and strong seismic phases that are characteristic of large deep teleseismic events. We used two methods to remove the signal-generated noise. The first one employs the empirical transfer function constructed from MOBB data and nearby land station data that do not show the signal-generated noise. Results obtained with this method for the Fiji Islands event are presented in Figure 3.21g. Island station FARB was used as a reference land station to obtain the empirical transfer function. To demonstrate that the empirical transfer function from one event can be used to remove signal-generated noise from another event, we used the empirical transfer function obtained from the 11/17/2002  $M_w$  7.3 Kurile event to “clean” the Fiji Islands event data. The results in Figure 3.21h show that most of the signal-generated noise at MOBB was removed. This suggests that to routinely clean smaller events, we will not need to compute the empirical transfer function every time, but rather use one from a previous

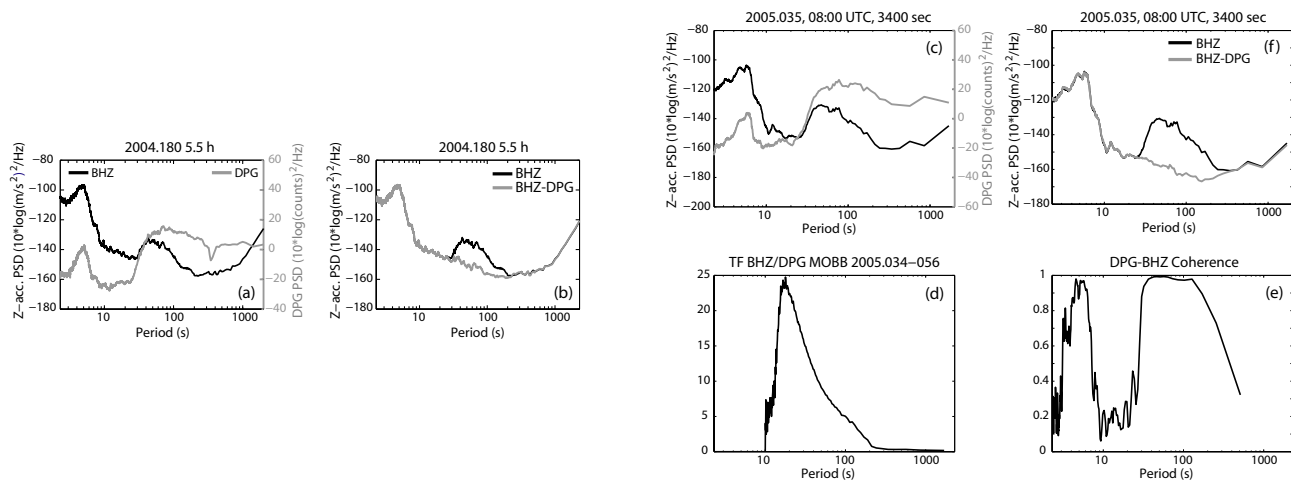


Figure 3.20: *Left*: Example of the time-domain method to remove noise from the earthquake-free vertical data. (a) Power spectral density (PSD) calculated for a 5.5-hour period without earthquakes for the vertical seismic channel (black) and the DPG (gray). At periods longer than 20 s the infragravity “hump” is observed for both datasets. (b) PSD for the vertical seismic channel before (black) and after (gray) the time-domain subtraction of the DPG signal. *Right*: Example of the transfer-function method to remove noise from the earthquake-free vertical data. (c) Power spectral density (PSD) for 1-hour period without earthquakes for the vertical seismic channel (black) and DPG (gray). (d) Transfer function between vertical seismic and DPG signal calculated from 144 1-hour long data windows within 2005.034-056 period. (e) Coherence between the vertical seismic and DPG channel for the selected 1-hour period on day 2005.035. (f) PSD for the vertical seismic channel before (black) and after (gray) the noise removal using the transfer function shown in (d).

strong event.

The second method uses a synthetic transfer function computed by modeling the response of shallow layers at the MOBB location. The response of the sedimentary layers is modeled using the propagator matrix approach (*Kennett and Kerry, 1979*). To obtain the response of the 1-D structure we used a previously published 1-D crustal model for this region (*Begnaud, 2000*) and replaced the top 350 m with a slower sedimentary layer. The synthetic transfer function was obtained by the spectral division of the result obtained with the 1-D model with the additional sedimentary layer and the result obtained with the original 1-D crustal model. The synthetic transfer function was then used to deconvolve the signal-generated noise from the MOBB vertical channel (Figure 3.21i).

Results presented in Figure 3.21e-i show that both methods can successfully remove the signal-generated noise from the MOBB data and that the obtained results are similar to the waveforms observed at the nearby land station (Figure 3.21f).

## 10.4 Conclusions

The described methods are an important tool to remove noise from the seismic data recorded at the ocean bottom buried broadband installations. Both methods used to remove the long-period background noise require

the locally recorded pressure signal at the seafloor. It is therefore important to have a reliable pressure sensor collocated with the ocean bottom seismometer. It is also important that the sampling rate for the DPG and other environmental data (e.g. temperature, ocean current speed and direction) is high enough so that they can be used in the post-processing for the complete seismic frequency band.

## 10.5 Acknowledgements

The MOBB instrumentation, deployment, and maintenance were supported by Lucile and David Packard Foundation funds to MBARI, NSF grant OCE9911392, and UC Berkeley funds.

## 10.6 References

- Begnaud, M. L., K. C. McNally, D. S. Stakes, and V. A. Gallardo, A crustal velocity model for locating earthquakes in Monterey Bay, California, *Bull. Seism. Soc. Am.*, *90*, 1391-1408, 2000.
- Crawford, W. C. and S. C. Webb, Identifying and removing tilt noise from low-frequency ( $< 0.1$  Hz) seafloor vertical seismic data, *Bull. Seism. Soc. Am.*, *90*, 952-963, 2000.
- Dolenc, D., B. Romanowicz, D. Stakes, P. McGill, and D. Neuhauser, Observations of infragravity waves

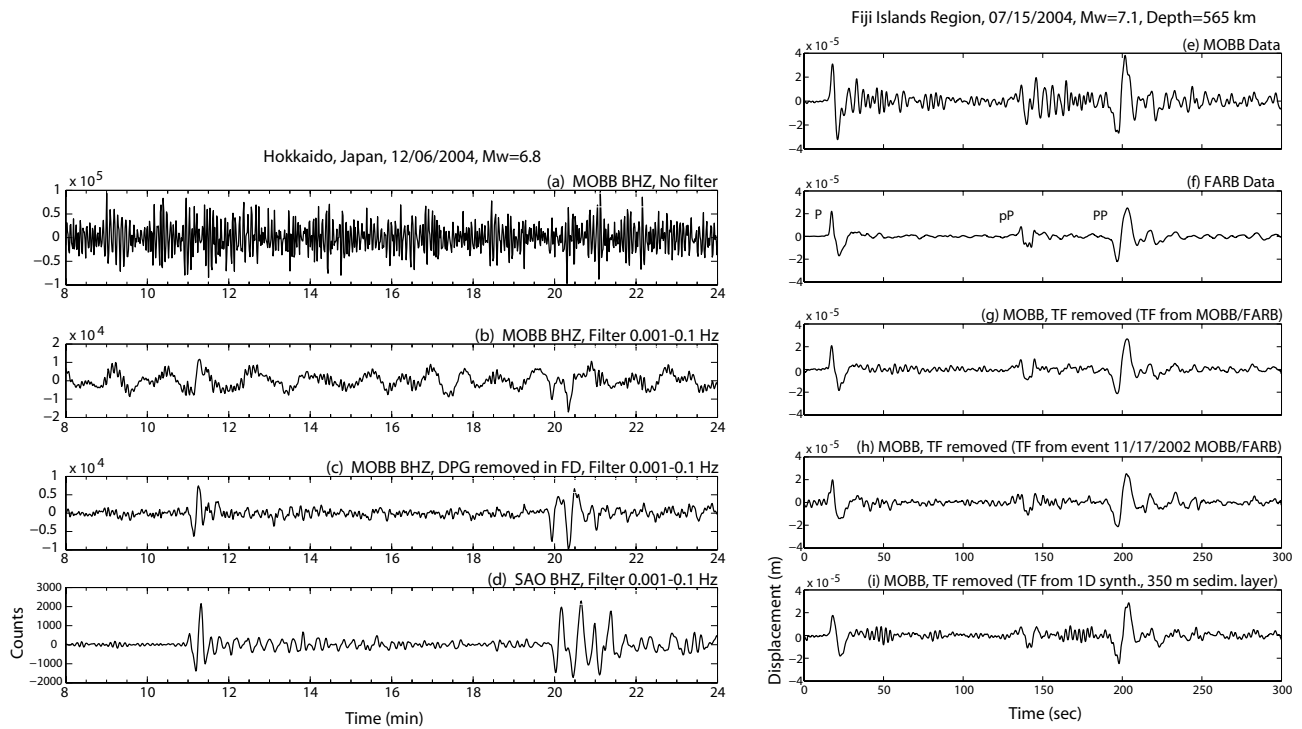


Figure 3.21: *Left*: Example of long-period background noise removal for the 12/06/2004  $M_w$  6.8 Hokkaido, Japan earthquake using the transfer function shown in Figure 3.20d. (a) Original MOBB vertical data. (b) MOBB data bandpass filtered between 0.001 and 0.1 Hz. (c) MOBB data after removal of the coherent DPG signal and bandpass filtered between 0.001 and 0.1 Hz. (d) Land station SAO data bandpass filtered between 0.001 and 0.1 Hz. *Right*: Three examples of deconvolution of the signal-generated noise at MOBB for the Fiji Islands event. (e) Original MOBB data. (f) Original FARB data. (g) MOBB data after removing empirical transfer function constructed using MOBB and FARB data. (h) Same as (g), only that empirical transfer function obtained from the 11/17/2002  $M_w$  7.3 Kurile Islands event was used. (i) MOBB data after removing a synthetic transfer function obtained by 1-D modeling of the shallow structure with a 350 m sedimentary layer ( $v_p = 0.324\text{km/s}$ ,  $v_s = 0.196\text{km/s}$ , and  $\rho = 1.3\text{g/cm}^3$ ).

at the Monterey ocean bottom broadband station (MOBB), *Geochem., Geophys., Geosys.*, 6, (9), 1-13, doi:10.1029/2005GC000988, 2005b.

Dolenc, D., B. Romanowicz, B. Uhrhammer, P. McGill, D. Neuhauser, and D. Stakes, Identifying and removing noise from the Monterey Ocean Bottom Broadband seismic station (MOBB) data, Submitted to *Geochem. Geophys. Geosys.*, 2006.

Kennett, B. L. N., and N. J. Kerry, Seismic waves in a stratified half space, *Geophys. J. R. Astr. Soc.*, 57, 557-583, 1979.

Romanowicz, B., D. Stakes, R. Uhrhammer, P. McGill, D. Neuhauser, T. Ramirez, and D. Dolenc, The MOBB Experiment: A prototype permanent off-shore ocean bottom broadband station, *Eos Trans., AGU*, 84, (34), 325, 331-332, 2003.

Uhrhammer, R., B. Romanowicz, D. Neuhauser, D. Stakes, P. McGill and T. Ramirez, Instrument testing and first results from the MOBB Observatory, *Eos Trans., AGU*, 83, (47), Fall Meet. Suppl., F1008, 2002.

Zürn, W. and R. Widmer, On noise reduction in vertical seismic records below 2 mHz using local barometric pressure, *Geophys. Res. Lett.*, 22, 3537-3540, 1995.

# 11. The Orinda Earthquake Sequence: Complexity in Small Earthquakes

Margaret Hellweg

## 11.1 Introduction

How different are large and small earthquakes? In large earthquakes, such as the 2004 Sumatra event, we expect a long lasting rupture process with several episodes of energy release. We usually imagine that earthquakes with magnitudes smaller than 4 are point sources in space and time. The events in sequence of earthquakes which occurred near Orinda, California offers an opportunity to explore this question. On October 19 a  $M_L$  3.5 earthquake (MS) occurred almost directly below Berkeley Seismological Laboratory's station BRIB (37.92 N, 122.15 W). At the surface are a broadband seismometer and an accelerometer. In addition, there is a borehole at the station, with a 3-component geophone and a 3-component accelerometer sampled at 500 sps at a depth of 119 m. The sequence began on 19 Oct 2003 at 14:35:27 UTC, about an hour before the MS with a  $M_d$  2.5 foreshock, and included more than 4000 aftershocks ranging in magnitude from - 2.5 to 3.4 over the course of the next 3 months.

## 11.2 Event Complexity

The record of the mainshock (15:32:52 UTC on October 19 with  $M_L$  3.53 (Figure 3.22A) is quite simple, as we expect from a point source. However, the slightly smaller aftershock the next day (October 20, 17:50 UTC,  $M_L$  3.4, Figure 3.22B) exhibits a number of P-wave pulses before the arrival of the S-waves. Even smaller events exhibit similar complexity (Figure 3.22C), with several P pulses of similar amplitude arriving before the first S-wave. For each P pulse, there is a corresponding S pulse. Using time-domain polarization analysis to find the azimuth and incidence angles (Plesinger *et al.*, 1986, Abercrombie, 1995), the direction to the source of the waves can be determined. The distance to the source can be derived from the delay between the P- and S-waves from the same source. I performed this analysis for a selection complex events to see if the P-waves came from different locations. Figure 3.23 shows the locations of three P-wave sources for the  $M_L$  3.4 aftershock of October 20 and two for a  $M_L$  0.5. The mainshock location and the locations of the foreshock and a number of other small, simple aftershocks are also shown. Each P-wave pulse from each these events clearly stems from a different location.

## 11.3 Perspectives

The source of the complexity observed in these two events, as well as in other small events of the Orinda sequence, is as yet undetermined. There are three possible causes for the complexity observed here. The simplest explanation is that several earthquakes of similar size occur with in a very short time of each other, thus that the events are independent. It is also possible that the rupture process of the event is uneven, and P-wave pulses are generated as the rupture propagates through the medium, releasing energy in separate episodes. Finally, the later events may be triggered in the stressed medium by the passing waves of the first event. Further investigations of the timing of the later arrivals may provide insights. However, an important remaining unknown which can influence the interpretation is the velocity structure in the source region.

## 11.4 References

Abercrombie, R.E., Earthquake locations using single-station deep borehole recordings: Implications for microseismicity on the San Andreas fault in southern California. *J. Geophys. Res.*, 100, 24003-24014, 1995.

Plesinger, A., M. Hellweg and D. Seidl, Interactive high-resolution polarization analysis of broad-band seismograms. *J. Geophysics*, 59, 129-139, 1986

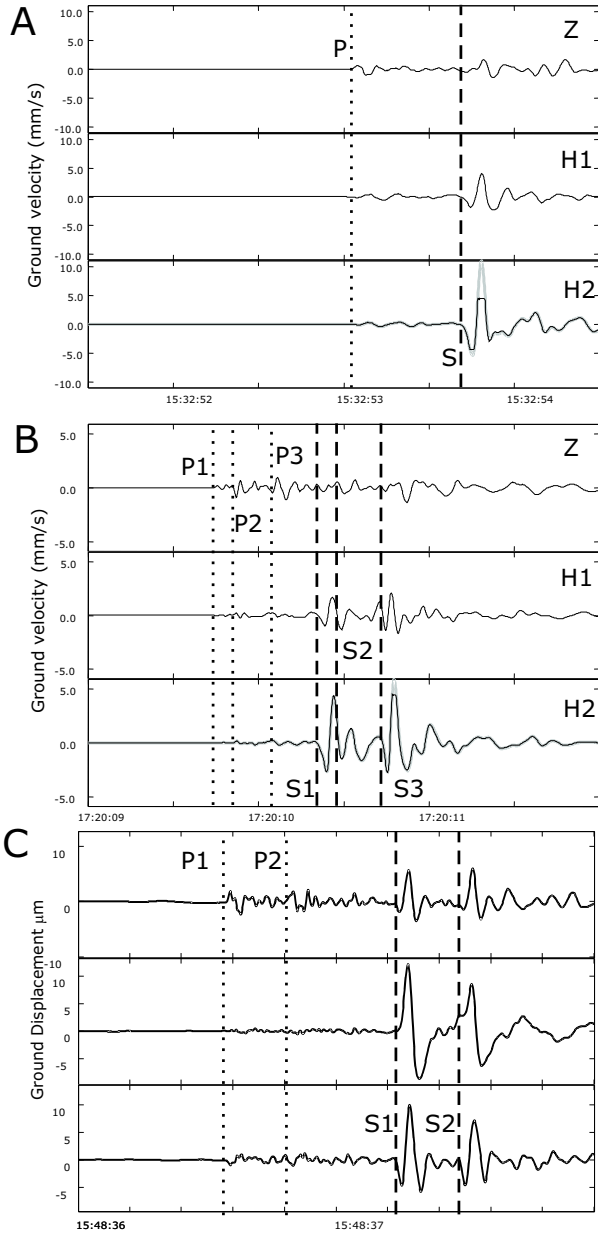


Figure 3.22: Waveforms for the mainshock (A), largest aftershock (B) and a  $M_L$  0.5 aftershock of the Orinda sequence. Note that there are three P-wave pulses in the large aftershock, and at least two in the small one. It may be that these are because several events happen within a short time, or this may be due to rupture propagation.

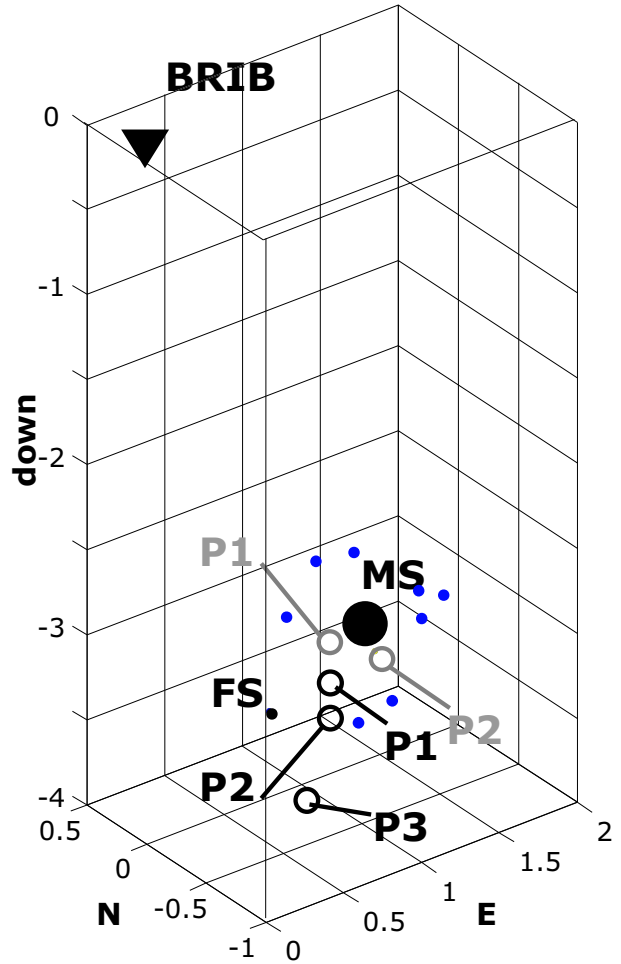


Figure 3.23: Locations of the mainshock (large, solid circle), and a number of small, simple aftershocks (small, solid circles). P-wave locations for the largest aftershock are indicated by the black, open circles (P1, P2, P3). For the small aftershock in Figure 3.22C they are marked by gray, open circles.

## 12. Northern California Seismicity Project

Robert A. Uhrhammer

### 12.1 Introduction

The Northern California Seismicity Project (NCSP) is a counterpart to the San Francisco Bay Region (SFBR) - Historical Earthquake Re-analysis Project (HERP), which has been reported upon in previous annual reports. The initial objective of this project, which commenced in August, 2000, is to transcribe the pre-1984 data for  $M_L \geq 2.8$  earthquakes, which have occurred in Northern and Central California (NCC) (outside of the SFBR covered by HERP), from the original reading/analysis sheets, kept on store in the Berkeley Seismological Archives, to a computer readable format.

Characterization of the spatial and temporal evolution of NCSP seismicity during the initial part of the earthquake cycle as the region emerges from the stress shadow of the great 1906 San Francisco earthquake is the long term goal. The problem is that the existing BSL seismicity catalog for the SFBR, which spans most of the past century (1910-present), is inherently inhomogeneous because the location and magnitude determination methodologies have changed as seismic instrumentation and computational capabilities have improved over time. As a result, NCC seismicity since 1906 is poorly understood.

Creation of a NCC seismicity catalog that is homogeneous, that spans as many years as possible, and that includes formal estimates of the parameters and their uncertainty is a fundamental prerequisite for probabilistic studies of the NCC seismicity. The existence of the invaluable BSL seismological archive, containing the original seismograms as well as the original reading/analysis sheets, coupled with the recently acquired BSL capability to scan and digitize historical seismograms at high resolution allows the application of modern analytical algorithms towards the problem of determining the source parameters of the historical SFBR earthquakes.

### 12.2 Background and Motivation

Although the 1910 to present BSL catalog of earthquakes for NCC appears to be a simple list of events, one must remember that it really is a very complex data set. It is easy to misinterpret observed variations in seismicity if we do not understand the limitations of this catalog. The existing 1910 to present BSL catalog of earthquakes for NCC is inhomogeneous in that it suffers from the three types of man-made seismicity changes identified by *Habermann* (1987), namely detection changes, reporting changes, and magnitude shifts. The largest change in the detection capability of the BSL seismic station net-

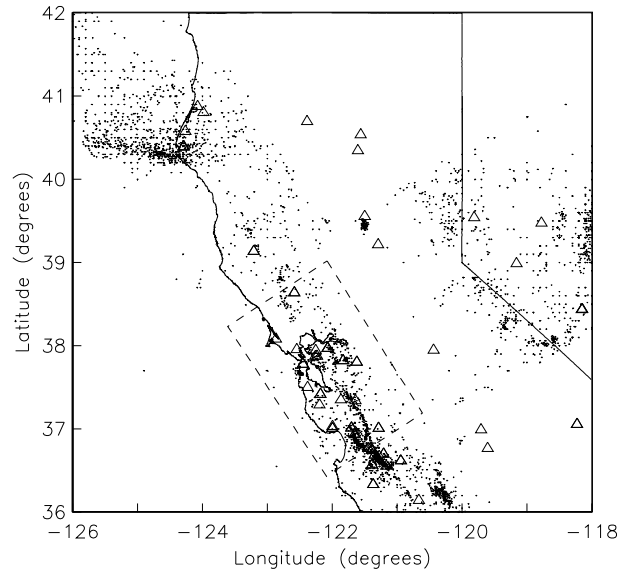


Figure 3.24: Map of the NCC Region showing the 1951-1983  $M_L \geq 2.9$  seismicity (small dots). The triangles are the seismic stations, operated by Berkeley and adjacent networks between 1951 and 1983, for which data are available. Events occurring in the dashed inset box were transcribed and analyzed as a part of the San Francisco Bay Region: Historical Earthquake Re-analysis Project (HERP).

work occurred starting circa 1927 with the installation of the Wood-Anderson and Benioff seismometers at several sites in NCC (see Figure 3.24) and the resulting increase in sensitivity lowered the threshold for detection of NCC earthquakes by about 2  $M_L$  units. The most significant reporting change occurred circa 1942 when the BSL began determining  $M_L$  for some earthquakes and by 1948  $M_L$  was routinely determined and reported for all SFBR earthquakes listed in the BSL Bulletin (*Romney and Meeker*, 1949).

The lack of a homogeneous catalog of earthquake for the SFBR that spans most of the past century, the availability of the invaluable BSL seismological archive, the interest in the Working Group on California Earthquake Probabilities (WGCEP, 1999), the funding of an initial effort with support from the USGS-PG&E CRADA, and the purchase and loan of a high-resolution wide-format digitizer by the USGS, combine to provide both an incentive and a unique opportunity to systematically re-process, using modern algorithms, the BSL seismo-

graphic records and data for SFBR earthquakes and to produce a homogeneous catalog of earthquakes for the region.

### 12.3 Initial Effort

To begin and expedite the transcription process, we first converted all relevant available data from the online NCEDC event catalogs and the in-house phase data to a flat transcription file format for the years 1951 through 1983. We also acquired a copy of the International Data Center (ISC) CDROM which contains events and associated station data published in the ISC Bulletins from January 1964 through December 1977 (Version 1.2). This ISC data set includes event and station data for the subset of Berkeley stations that were contributed to the ISC. The CDROM also contains an algorithm to search the database and extract and translate the ISC coded phase Berkeley data to a readable print format for years 1963 through 1977. This enabled us to start with transcription files that contained approximately half the data that is on the original reading/analysis sheets for the years 1964 through 1983. The primary data from the original reading/analysis sheets that was not included in this process was the Wood-Anderson maximum trace amplitude data that is crucial for the determination of local magnitude.

### 12.4 Current Effort

During the past year, five students worked on the process of transcribing and verifying the transcription of the data from the original BSL reading/analysis sheets to computer readable form. The verification process had two components: the first step is perform a detailed syntactical check of the transcribed information format using an ad hoc syntactical algorithm, and the second is to obtain an initial location for the event and check for anomalous observations. Syntactical errors were subsequently corrected, and anomalous observations were verified and corrected if necessary. To date, they have transcribed and verified data for over 5200 earthquakes that occurred in NCC between 1951 and 1983. They started by verifying the transcription of the original reading/analysis sheets and locating the earthquakes starting in 1983, and they worked back in time. More detailed felt reports and comments were added when available. Owing largely to the computer readable information that was available from the ISC, processing the 1964 to 1983 files took the least amount of time. Since none of the data on the pre-1964 reading/analysis sheets existed in a computer readable form, all data has to be transcribed, and, consequently, it takes more time to transcribe each event. We have now completed the transcription and verification process for over 5200 NCC ML 2.9+ earthquakes that occurred between 1951 and 1983.

The pre-1951 reading/analysis sheets data do not contain Wood-Anderson maximum trace amplitude data,

which is used in the calculation of local magnitude, so that the original Wood-Anderson seismograms will have to be retrieved from the archive and the amplitudes read. This quite labor intensive component of the project is planned for the coming year.

### 12.5 Acknowledgements

UC Berkeley students Vicky Chi Sum Chan, Rose Li, Sean Tsai, Noli Valera, and visiting U Pennsylvania student Carmen Rodriguez participated in this project during the past year, and we thank them for their efforts.

This project was partially supported by the USGS funding of the Northern California Earthquake Data Center.

### 12.6 References

Habermann, R. E., Man-made changes of seismicity rates, *Bull. Seism. Soc. Am.*, 77, 141-159, 1987.

Romney, C. F. and J. E. Meeker, Bulletin of the Seismographic Stations, *University of California Press*, 18, pp. 89, 1949.

## 13. Seismogram Scanning Project

Robert A. Uhrhammer

### 13.1 Introduction

This aim of Seismogram Scanning Project (SSP) is to scan selected analog seismograms kept on store in the Berkeley Seismological Laboratory (BSL) Seismogram Archive and generate digital image files for studying microseismic source areas and distribution in relation to wave climate. The Berkeley Seismogram Archive, where approximately 1.2 million analog seismograms dating back to 1910 are stored, contains seismograms recorded at the seismic stations located on the UC Berkeley Campus (BRK and BKS), dating back to 1930, which are crucial for this project. This scanning project is being undertaken in collaboration with Dr. Peter Bromirski of the University of California, San Diego/Scripps Institution of Oceanography on his project funded by the California Department of Boating and Waterways. The corresponding digitization of the scanned seismograms is being done at the Scripps Institution of Oceanography.

### 13.2 Background and Motivation

The photographic and smoked paper seismograms kept on store in the BSL Seismogram Archive are gradually deteriorating over time, and scanning the seismograms into a computer readable format is essential if they are to be preserved for the future. BSL has a wide format scanner, and whenever the opportunity and funding allows, we make an effort to scan seismograms.

### 13.3 Initial Effort

The initial effort was to systematically digitize the November-March vertical component Sprengnether seismograms and also the November-March Berkeley vertical component Wilip-Galitzin seismograms for selected "El Nino and La Nina" winters. The seismograms were scanned at a resolution of 400 dots per inch on an Contex Scanning Technology Ideal FSS 18000 DSP Full Scale Scanner using their interactive WIDEimage scanning software package (available via URL: <http://www.contex.com>). The scanned images are stored as Tag Image Format (TIF) bitmap image files. To substantially reduce the storage requirements, a histogram analysis is employed to interactively set an appropriate threshold and the scanned seismograms are stored as 1-bit resolution line-art images. An example of a scanned SPR seismogram is shown in Figure 3.25.

### 13.4 Current Effort

During the past year we have completed the task of systematically scanning the available November-March Berkeley vertical component Sprengnether seismograms for the winters of 1962 through 1991 and also the available November-March Berkeley vertical component Wilip-Galitzin seismograms for the winters of 1930 through 1964 (a total of approximately 9,300 seismograms). We are also finalizing a paper "Comparison of Wilip-Galitzin, Strengnether and Streckisen Seismographic Recordings at Berkeley" to be submitted to the Bulletin of the Seismological Society of America.

### 13.5 Digitization Procedure

Digitization of the photographic seismograms has two components. The seismograms are first scanned at a resolution of 400 dots per inch on an Contex Scanning Technology Ideal FSS 18000 DSP Full Scale Scanner. The scanned images are stored as Tag Image Format (TIF) bitmap image files. To substantially reduce the storage requirements, a histogram analysis is employed to interactively set an appropriate threshold, and the scanned seismograms are stored as 1-bit resolution line-art images. The traces on the scanned seismogram image are then digitized at nominally 4 samples per second using the SeisDig software package (*Bromirski and Chuang, 2003*) available for download at URL: <http://www.ucsg.edu/~bromirski>. The resulting digitized seismogram has an amplitude resolution of 0.0635 mm (i.e. the pixel resolution and equivalent to a data logger sensitivity of 15748 DU/M) and a time resolution of 0.254 seconds for the SPR seismograms recorded at 15 mm/min and 0.127 seconds for the W-G seismograms recorded at 30 mm/min (also the pixel resolution). The effective dynamic range is approximately 64 dB ( $20 \log_{10}(100\text{mm}/0.0635\text{mm})$ ). An example of a digitized SPR seismogram is shown in Figure 3.25.

### 13.6 Calibration of Wilip-Galitzin, Sprengnether and Streckisen Seismographs

As seismic instrumentation has evolved, three different three-component sets of long-period/broadband seismographs have been installed and operated, with overlapping intervals, at Berkeley since the 1930's. Wilip-Galitzin (W-G) seismographs were operated on the northern most seismic piers in the basement of Haviland Hall on the Berkeley Campus (BRK) from August

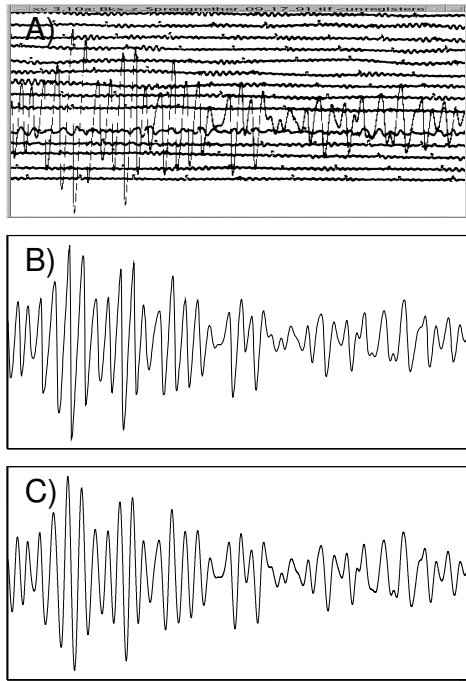


Figure 3.25: A comparison of: A) the scanned BKS Sprengnether Z-component seismogram; B) the corresponding digitized waveform, and; C) the corresponding waveform synthesized from the co-sited Streckeisen STS-1 broadband seismograph. The seismic signal is from a M 5.7 teleseism which occurred 4000 km SE of Berkeley (1991/09/18,09:48:13; 14.65N, 90.99W) in Guatemala. All three plots are at the same scale with the horizontal axis spanning 511.25 seconds and the vertical axis spanning 175 mm. That all three waveforms are highly similar is verification of the accuracy of the digitization procedure and the accuracy of the Sprengnether transfer function.

28, 1930 until February 1, 1965. World Wide Standardized Station (WWSS) Sprengnether (SPR) long-period seismographs were operated in the Byerly Seismic Vault (BKS), located in Strawberry Canyon behind the Botanical Garden, from June 8, 1962 until September 30, 1991. Streckeisen (STS-1) broadband seismographs began recording in the Byerly Seismic Vault (BKS) on May 11, 1987 with a 16-bit PC-based recording system (*Bolt et al.*, 1988) and a 20 second pendulum configuration and by August 8, 1991 they had evolved into the current 24-bit Quanterra Q680 data logger and 360 second very-broadband (VBB) pendulum configuration. The W-G and SPR seismographs operated concurrently, but not co-sited, from June 8, 1962 until February 1, 1965. The SPR

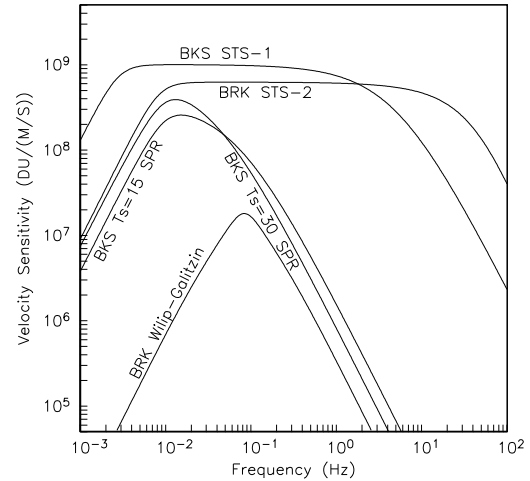


Figure 3.26: A comparison of the velocity responses of the BRK W-G and STS-2 and the BKS SPR and STS-1 seismographs operated at Berkeley. The W-G and SPR instruments recorded galvanometrically on photographic paper, and the paper seismograms are scanned at a resolution of 400 dots per inch. The STS-1 and STS-2 instruments record digitally via a high-resolution data logger. The velocity sensitivity is given in digital units per meter per second (DU/(M/S)). Two responses are given for the SPR because its natural period ( $T_s$ ) was changed from 30 seconds to 15 seconds on May 12, 1965.

and STS-1 seismographs operated concurrently at BKS from August 8, 1991 until September 30, 1991. Comparison of selected seismograms from these intervals allow us to verify the calibration and response of these seismographs, and to demonstrate that, within appropriate passbands, the earlier instrument seismograms can be reliably synthesized from later instrument seismograms, and that absolute ground motions can be reliably estimated. An example of a SPR seismogram, synthesized from the corresponding STS-1 seismogram, is shown in Figure 3.26. A Streckeisen STS-2 seismograph has operated at BRK since January 1, 1993 and a comparison of selected seismograms from the BKS STS-1 and the BRK STS-2 is used to quantify differences in their site responses. A comparison of the responses of these seismographs is shown in Figure 3.26.

## 13.7 Acknowledgements

UC Berkeley student Kevin Lee participated in this project during the past year, and we thank him for his efforts.

This project was funded by sub-award of the California Department of Boating and Waterways Contract 03-106-105.

## 13.8 References

Bolt, B. A., J. E. Friday and R. A. Uhrhammer, A PC-based Broadband Digital Seismograph Network, *Geophysical Journal*, 93, 565-573, 1998.

Bromirski, P. D. and S. Chuang, SeisDig Software to Digitize Scanned Analog Seismogram Images: User's Manual, *Scripps Institution of Oceanography Technical Report*, Scripps Institution of Oceanography, Integrative Oceanography Division, UC San Diego, 28 pp., July 2, 2003.

# 14. Regional Attenuation Method Comparison for Northern California

Sean R. Ford, Douglas S. Dreger, Kevin Mayeda, William R. Walter (Lawrence Livermore National Laboratory), Luca Malagnini (Istituto Nazionale di Geofisica e Vulcanologia), and William S. Phillips (Los Alamos National Laboratory)

## 14.1 Introduction

Understanding of regional attenuation ( $Q^{-1}$ ) can help with structure and tectonic interpretation, and correcting for the effects of attenuation can lead to better discrimination of small nuclear tests. Present threshold algorithms for event identification rely on  $Q$  models that are derived differently, and the models can vary greatly for the same region. It is difficult to learn the cause of such discrepancies because the methods and parameterizations change for each analysis. In order to better understand the effects of different methods and parameterizations on  $Q$  models, we implement four popular methods and one new method to measure  $Q$  of the regional seismic phase,  $Lg$  ( $Q_{Lg}$ ), using a high-quality dataset from the Berkeley Digital Seismic Network (BDSN). With this knowledge, it will be possible to better assess the results of published attenuation studies, and future efforts can benefit from the outlined comprehensive analysis procedure.

## 14.2 Methods, Comparisons, and Sensitivity Tests

The dataset consists of 158 earthquakes recorded at 16 broadband (20 sps) three-component stations of the BDSN between 1992 and 2004. The wide distribution of data parameters allows for sensitivity testing to a given dataset. We calculate  $Q_{Lg}$  by fitting the power-law model,  $Q_0 f^\alpha$ , in Northern California using five different methods. The first two methods use the seismic coda to correct for the source effect. These methods can produce best-fit power-law parameters for specific stations. The last three methods use the spectral ratio technique to correct for source, and possibly site effects. These methods produce best-fit power-law parameters for specific inter-station paths.

### Coda normalization method (CNM)

CNM uses the coda as a proxy for the source and removes it from the  $Lg$  spectrum (Aki, 1980; Yoshimoto *et al.*, 1993). The amplitude is then least-squares fit as a function of distance in small frequency bands for each station, where the slope is related to path attenuation,  $Q^{-1}$ .  $Q^{-1}$  at the center frequency of each band then reveals a power-law  $Q$  model for each station.

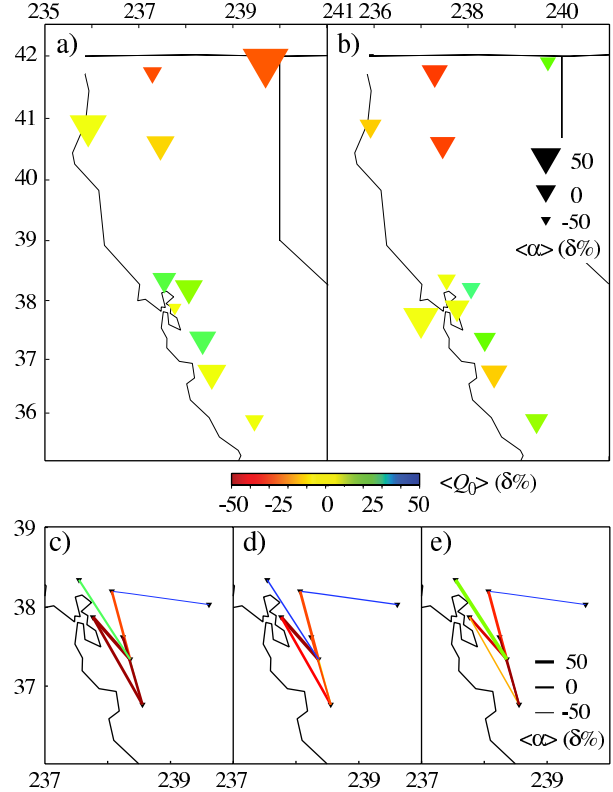


Figure 3.27: Spatial variability in the percent deviation from the method average power-law fit parameters ( $Q_0 f^\alpha$ ) for the (a) coda normalization method, (b) coda-source normalization method, (c) two-station method, (d) reverse two-station method, and (e) source-pair / receiver-pair method. The average models are  $104f^{0.61}$ ,  $172f^{0.57}$ ,  $132f^{0.53}$ ,  $121f^{0.52}$ ,  $76f^{0.76}$ , respectively

### Coda-source normalization method (CSM)

CSM uses the 1-D coda-source spectra previously calculated in the study by Mayeda *et al.* (2005) and removes it from the  $Lg$  spectrum in small frequency bands (Walter *et al.*, 2006).  $Q^{-1}$  is calculated for each of these bands for each event-station path. In this application of CSM, all paths to a common station are fit to find a power-law  $Q$  model for each station.

### Comparison of CSM and CNM

Since both CNM and CSM give a result for each station, we compare these results by finding the percent deviation of each station from the average  $Q_0 f^\alpha$  produced

for each method. Comparisons are mapped in Figure 3.27a-b when a solution was calculated for both methods. The average  $Q_{Lg}$  model given by the CNM is  $104f^{0.61}$ , while the CSM produces an average of  $172f^{0.57}$ . The absolute difference in  $Q_{Lg}$  models may be due to the absence of a site correction in the CSM. There is overall relative agreement in the two methods, with low  $Q$  in the northern part of the study region and variable  $Q$  in the Bay Area. This Bay Area variance may be due to paths crossing different tectonic regimes to reach these stations and forming an average fit. Stations MOD, FARB, and POTR appear to have a strong difference in measured  $Q_0f^\alpha$ . However, the fit to a power-law model is poor at frequencies  $> 2$  Hz, and the comparison for a power-law model may be flawed for these stations. Stations BKS and MHC are consistently lesser or greater, respectively, than the average for each method, but there is a large percent deviation for the two stations.

### Two-station method (TSM)

TSM takes the spectral ratio of  $Lg$  recorded at two different stations along the same narrow path from an event (Xie, 2002; Xie and Mitchell, 1990). We restricted the path to fall in an azimuthal window of  $15^\circ$ . The ratio removes the common source term and the amplitude is fit in the log domain so that the slope is  $\alpha$  and the intercept is  $Q$ .

### Reverse two-station method (RTSM)

RTSM uses two TSM setups where an event is on either side of the station pair in a narrow azimuthal window (Chun et al., 1987; Fan and Lay, 2003). The two ratios are combined to remove the common source and site terms and the amplitude is fit in the log domain so that the slope is  $\alpha$  and the intercept is  $Q$ .

### Source-pair / receiver-pair method (SPRPM)

SPRPM is basically the RTSM with a relaxation on the narrow azimuthal window requirement (Shih et al., 1994).

### Comparison of TSM, RTSM, and SPRPM

Since TSM, RTSM, and SPRPM give a result for interstation paths, we compare these results by finding the percent deviation of each interstation path from the average  $Q_0f^\alpha$  produced for each method. Comparisons are mapped in Figure 3.27c-e when a solution was calculated for all methods. The average  $Q_{Lg}$  model given by the TSM is  $132f^{0.53}$ , by RTSM is  $121f^{0.52}$ , and by SPRP is  $76f^{0.76}$ . Values of  $Q_0$  are fairly uniform with greater than average and lesser than average values consistent across each of the respective methods. A notable exception is the path from MHC to SAO, where the TSM calculates a greater than average  $Q_0$  and the other methods find a

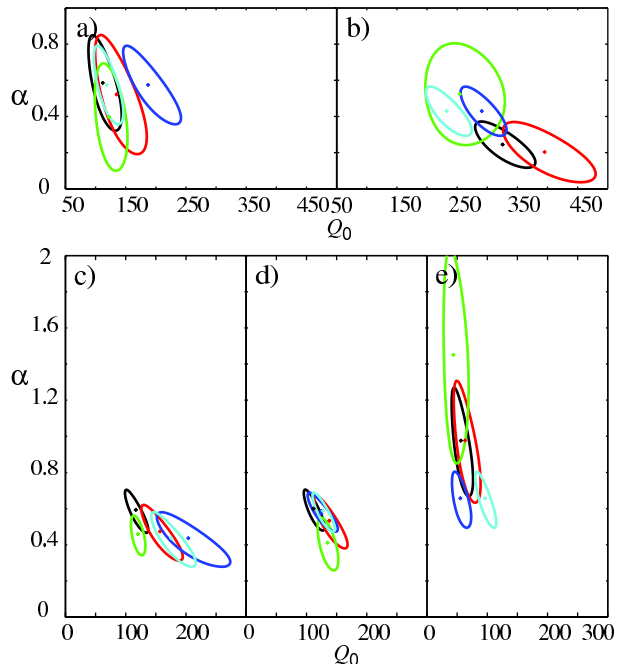


Figure 3.28: 95% confidence ellipses for the power-law model parameters for station PKD calculated by the (a) coda normalization, (b) coda-source normalization, (c) two-station, (d) reverse two-station, and (e) source-pair/receiver-pair methods obtained by the original parameterization (black), and by varying the spreading exponent (red), bandwidth (green), distance (dark blue), and time window (light blue). The small cross is the best-fitting parameter estimate. The coda-based methods are for station PKD, and the spectral ratio-based methods are for the path from MHC to POTR.

less than average  $Q_0$ . The mean value of  $Q_0$  and  $\alpha$  for SPRPM are very low for the region, and the power-law exponent,  $\alpha$ , varies widely among all methods. This may be due to the variance in the spectral amplitudes, and robust methods of spectrum estimation may reduce the variance.

### Sensitivity tests

We investigated how the choice of parameterization affects the results. In each test, only one parameter was varied, and  $Q_0f^\alpha$  was calculated with each of the methods. The varied parameters were geometrical spreading dependence ( $r^{0.5}$  to  $r^{0.83}$ ), measurement bandwidth (0.25-4 Hz to 0.5-8 Hz), epicentral distance of the data (100-400 km to 100-700 km), and the  $Lg$  window (2.6-3.5 km/s to 3.0-3.6 km/s). The range of parameterization was chosen based on the values used in previous studies.

All methods were affected by a change in spreading exponent, where there is a systematic increase in both  $Q_0$  and  $\alpha$  as the spreading exponent increases. Also,

when more of the spectrum below 1 Hz is sampled,  $\alpha$  can change significantly. The methods that use a maximum  $Lg$  amplitude in the time domain to measure  $Q_{Lg}$ , CNM and SPRP, are less sensitive to  $Lg$  window choice than the other methods. However, CNM is affected by epicentral distance, which may be due to the fixed time that the coda is sampled for all distances. The RTSM is the most robust and resistant to changes in parameterization.

In order to better visualize the sensitivity of the methods to varied parameterization, we produce 1-D power-law  $Q$  models for a common station, PKD, for the coda-based methods (Figure 3.28a-b), and a common path, MHC to POTR, for the spectral ratio based methods (Figure 3.28c-e). Error in these 1-D fits is calculated and we produce 95% confidence ellipses for each of the power-law model parameters (Aster *et al.*, 2005).

Estimates of the power-law parameters,  $Q_0$  and  $\alpha$ , have a complex relationship with parameterization choice. The greatest variance in  $Q_0$  is given by the CSM ( $\sim 200$ -500), while there is a large variance in  $\alpha$  calculated with the SPRPM ( $\sim 0.6$ -1.8). However, for all methods (with the possible exception of the RTSM) the 95% confidence region is large, and the range of the parameter estimates is greater than is given by previous 1-D  $Q_{Lg}$  studies, which often only present one choice of parameterization.

### 14.3 Conclusions

There is lateral variability in  $Q_{Lg}$  at 1 Hz and the power-law dependence on frequency in Northern California. The spatial variability is similar to that found by Mayeda *et al.* (2005), where there is high attenuation in the northern region of the study area and variable attenuation in the Bay Area. Trends in calculated power-law parameters are similar among the methods investigated in this study, though there is large variability in the absolute values for  $Q_0 f^\alpha$ .

The choice of spreading exponent, distance, and measurement window has a large influence on the best-fit power-law parameter estimates. Unless the parameterization choice can be constrained from a priori information, regional attenuation studies should search the entire solution space in order to report useful power-law  $Q$  models.

### 14.4 Acknowledgements

This research is sponsored by the Department of Energy through the National Nuclear Security Administration, Office of Nonproliferation Research and Development, Office of Defense Nuclear Nonproliferation.

### 14.5 References

Aki, K., Attenuation of shear-waves in the lithosphere for frequencies from 0.05 to 25 Hz, *Phys. Earth Planet. Inter.*, 21 50-60, 1980.

Aster, R. C., and B. Borchers, and C. H. Thurber, *Parameter Estimation and Inverse Problems*, San Diego: Elsevier Academic Press, 2005.

Chun, K. Y., G. F. West, R. J. Kokoski, and C. Samson, A novel technique for measuring  $Lg$  attenuation: Results from eastern Canada between 1-Hz to 10-Hz, *Bull Seism Soc.*, 77 398-419, 1987.

Fan, G. W., and T. Lay, Strong  $Lg$  wave attenuation in the Northern and Eastern Tibetan Plateau measured by a two-station/two-event stacking method, *Geophys. Res. Lett.*, 30, 2003.

Mayeda, K., L. Malagnini, W. S. Phillips, W. R. Walter, and D. Dreger, 2-D or not 2-D, that is the question: A northern California test, *Geophys. Res. Lett.*, 32, 2005.

Shih, X. R., K. Y. Chun, and T. Zhu, Attenuation of 1-6 s  $Lg$  waves in Eurasia, *J. Geophys. Res.*, 99 23859-23873, 1994.

Walter, W. R., K. Mayeda, L. Malagnini, L. Scognamiglio, Regional body-wave attenuation using a coda source normalization method: application to MEDNET records of earthquake in central Italy, *Seism. Res. Lett.*, 77 260, 2006.

Xie, J. K.,  $LgQ$  in the eastern Tibetan Plateau, *Bull Seism Soc.*, 92 871-876, 2002.

Xie, J., and B. J. Mitchell, Attenuation of multiphase surface-waves in the Basin and Range Province. 1.  $Lg$  and  $Lg$  coda, *Geophys. J. Int.*, 102 121-137, 1990.

Yoshimoto, K., H. Sato, and M. Ohtake, Frequency-dependent attenuation of P-wave and S-wave in the Kanto area, Japan based on the coda-normalization method, *Geophys. J. Int.*, 114 165-174, 1993.

# 15. Geodetically Constraining Indian Plate motion and Implications for Plate Boundary Deformation

Edwin (Trey) Apel, Roland Bürgmann, and Paramesh Banerjee (Wadia Institute of Himalayan Geology)

## 15.1 Introduction

Traditionally tectonic Indian plate motion has been estimated using closed plate circuit models and summing motions across mid-ocean ridges. More recently *Paul et al.*, (2001), using limited GPS velocity vectors, calculated a pole of rotation that suggested motion slower than that of the rates suggested by sea-floor spreading. *Socquet et al.*, (2006) estimate an India-Eurasia geodetic pole with rates  $\sim 5$  mm/yr slower than *Paul et al.*, (2001). We present new data spanning a larger and more significant portion of the "stable" Indian plate than previous studies. Our preliminary India-Eurasian pole estimates are consistent with *Socquet et al.*, (2006).

In addition to the above mentioned sites, we also include published data from numerous sources. However, many of the sites in this region are on or near plate boundaries (eg. along the Himalayan front or above the Sumatra subduction zone) making it difficult to use them for plate pole parameter determination. We use a block modeling approach to incorporate both rigid block rotation and near-boundary elastic strain accumulation effects in a formal inversion of the GPS velocities. Considered models include scenarios with and without independent microplates and a number of different plate boundary locations and locking depths.

## 15.2 GPS Velocities

The GPS velocities used in our inversion come from a solution of 164 global stations, including some unpublished campaign style sites from central and north-western India. These data were processed using GAMIT/GLOBK and processed by Paramesh Banerjee from the Wadia Institute of Himalayan Geology. Processing details can be found in (*Banerjee and Bürgmann*, 2002).

In addition to our own analysis, we integrate GPS-station velocities from published work along the Himalayans, throughout China, and southeast Asia (*Bettinelli et al.*, 2006; *Bock et al.*, 2003; *Calais et al.*, 2003; *Shen et al.*, 2005; *Socquet et al.*, 2006; *Zhang et al.*, 2004). We integrated these velocities into the reference frame of our own solutions by estimating translation and/or rotation parameters that minimized the differences in horizontal velocities for common sites. Our combined solution contains  $\sim 1800$  global velocities.

## 15.3 Plates

We define our plates as rigid blocks on a spherical earth bounded by dislocations in an elastic halfspace and invert for poles and rates of rotation that minimize the misfit to the GPS velocities using an extension of the block modeling code by *Meade and Hager* (2005). The segments that bound the blocks represent uniformly slipping elastic dislocations locked to some specified depth. Because our inversion combines rigid block rotation with elastic strain accumulation effects, the parameterization of the block boundary geometry is critical. Geometry of the block boundaries is based heavily on seismicity and adopted from prior analyses (eg. *Socquet et al.*, 2006, *Reilinger et al.*, 2006, *Meade*, IN PRESS) or adjusted as indicated by the geodetic data.

We invert the horizontal GPS velocities for poles of rotation constrained by the prescribed block geometry defined above. Systematic patterns in the residual velocities (observed minus predicted) are used as an indicator of where and how the model matches the observed surface velocities. Misfit statistics are used to formally evaluate the statistical significance of the plate kinematic scenarios we test.

## 15.4 Results and Discussion

Our preliminary results constrain a pole of rotation for India with respect to Eurasia to lie at  $29.04^\circ \pm 0.7^\circ$  N  $16.74^\circ \pm 1.6^\circ$  E with a counterclockwise angular velocity of  $0.42^\circ \pm 0.01^\circ$  Myr $^{-1}$ . This pole confirms that the NUVEL-1A rate is 20% too fast and the India-Eurasia convergence rates computed along the Himalaya front range from 34 mm/yr to 45 mm/yr between  $72^\circ$  N and  $96^\circ$  N longitude. Residual velocities from our inversion are shown in figure 3.29 and show near zero motion within uncertainties. The geographic distribution of stations within the Indian plate allows us to generate the most robust realization of Indian plate motion to date.

## 15.5 References

Banerjee, P., and R. Bürgmann, Convergence across the northwest Himalaya from GPS measurements, *Geophysical Research Letters*, 10.1029/2002GL015184, 2002.  
Bettinelli, P. J. Avouac, M. Flouzat, F. Jouanne, L. Bollinger, P. Willis, G. Chitrakar, Plate motion of India and interseismic strain in the Nepal Himalaya from GPS and DORIS measurements *Journal of Geodynamics*, 10.1007/s00190-006-0030-3, 2006.

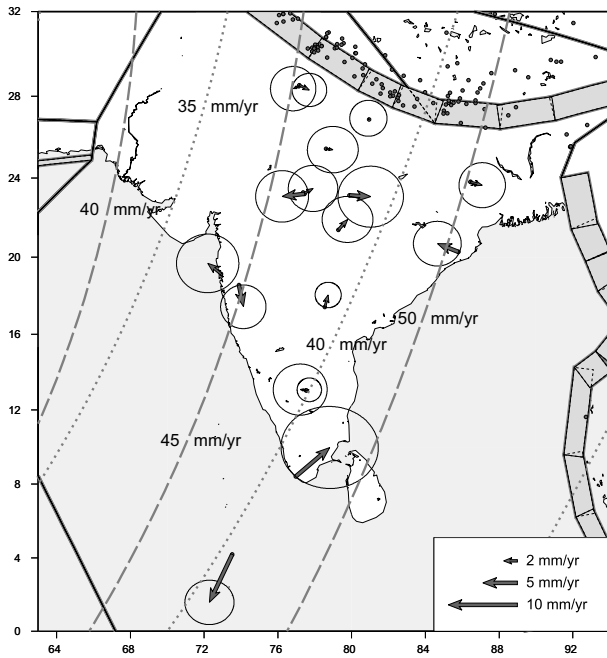


Figure 3.29: Residual velocities on the Indian plate from our robust inversion. Dashed lines show small circle pole traces from the NUVEL-1A IND-EUR pole of rotation, dotted lines are pole traces from this study. Circles show locations of GPS sites along the Himalayan range front however, velocity vectors at these locations have not been shown for the sake of brevity.

Bock, Y., L. Prawirodirdjo, J. F. Genrich, C. W. Stevens, R. McCaffrey, C. Subarya, S. S. O. Puntodewo, and E. Calais, Crustal motion in Indonesia from Global Positioning System measurements, *Journal of Geophysical Research*, 10.1029/2001JB000324, 2003.

Calais, E., M. Vergnolle, V. San'kov, A. Likhnev, A. Miroshnitchenko, S. Amarjargal, and J. Deverchere, GPS measurements of crustal deformation in the Baikal-Mongolia area (1994-2002): Implications for current kinematics of Asia, *Journal of Geophysical Research*, 108(B10), 2003.

Meade, Brendan, Mechanics of the India-Asia Collision Zone, *Geophysical Research Letters*, IN PRESS.

Meade, B. J., and B. H. Hager, Block models of crustal motion in southern California constrained by GPS measurements, *Journal of Geophysical Research*, 110, B03403, 10.1029/2004JB003209, 2005.

Paul, J., Bürgmann, R., Gaur, V. K., Bilham, R. Larson, K. M., Ananda, M. B., Jade, S., Mukal, M., Anupama, T. S., Satyal, G., Kumar, D., The motion and active deformation of India, *Geophysical Research Letters* 28(4), 2001.

Shen, Z.-K., J. Lü, M. Wang, and R. Bürgmann, Contemporary crustal deformation around the southeast borderland of the Tibetan Plateau, *Journal of Geophysical Research*, 10.1029/2004JB003421, 2005.

Socquet, A., Vigny, C., Chamot-Rooke, N., Simons, W., Rangin, C. and Ambrosius, B., India and Sunda plates motion and deformation along their boundary in Myanmar determined by GPS, *Journal of Geophysical Research*, 111, B05406, 10.1029/2005JB003877, 2006.

Zhang, P. Z., Z. Shen, M. Wang, W. J. Gan, R. Bürgmann, and P. Molnar, Continuous deformation of the Tibetan plateau from global positioning system data, *Geology*, 32(9), p. 809, 2004.

## 16. Large Scale Ground Deformation of Etna Observed by GPS Between 1994 and 2001

Nicolas Houlié, Pierre Briole, Alessandro Bonforte and Giuseppe Puglisi

### 16.1 Introduction

Etna is the most active volcano in Europe. Several active tectonic structures are located in its eastern part. Some of these structures, such as the Timpe fault system (extensive fault system trending NNW-SSE belonging to the Maltese escarpment) and the NNE-SSW faults (belonging to the Messina-Comiso line) were inherited from its geodynamic setting (Monaco *et al.*, (1997), Laigle, 1998, Nicolich *et al.*, 2000, Jacques *et al.*, 2001). Others, such as the Valle del Bove (Calvari *et al.*, 1998), the Pernicana fault system (Azzaro *et al.*, 1998, 2001a, 2001b), and the rift zones (Tibaldi and Gropelli, 2002), are linked to Mt. Etna's activity.

The Etna volcano GPS network, conceived in the late eighties, improved and maintained by Istituto Nazionale di Geofisica e Vulcanologia (INGV) research team, is composed of two main parts. Firstly, a local reference frame, relatively far from Mt. Etna's influence and assumed stable. Secondly, a monitoring network on the volcano dedicated to the study of the volcano dynamics (Puglisi *et al.*, 2004). Thus, this network is able to detect both volcanic and tectonic deformations of the area.

The last three flank eruptions of Mt. Etna occurred in 1991-1993, in July 2001 and november 2002 (Branca *et al.*, 2004). The time interval of our study was chosen to investigate the deep magma plumbing system of Etna (Patane *et al.*, 2000) while the GPS network remained stable (Puglisi *et al.*, 2004).

### 16.2 Data and data processing

Between 1994 and early 2001, thirty GPS campaigns were carried out by the INGV research group at twenty-three different benchmarks. All INGV receivers were Trimble 4000 SST/SSI. The various campaigns used in this study were designed for various aims (i.e. monitoring surveys, specific experiment in support to kinematic surveys or photogrammetry). Therefore, they were not homogenous in terms of duration of observations, sampling rates, number of measured benchmarks, number of instruments involved. Typically measurement sessions last two to four hours at 10, 20, or 30 seconds sampling rate. Station 98, located on the roof of the INGV building in Catania, records continuously during the campaigns.

To tie the local network to the European Reference Frame (EUREF), we have processed the available data from permanent sites located in southern Europe with our local dataset using GAMIT software (King and Bock, 1999). All the ambiguities have been fixed for baselines

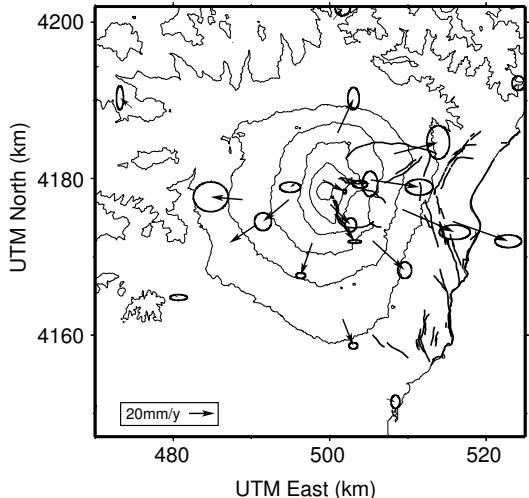


Figure 3.30: Velocities computed from time-series (reference NOTO). The location of the source is symbolized by a black star.

shorter than 500km only. Adjusting the computed baselines for each campaign using the GLOBK software (Herring, 2005), we established a set of coordinates for each campaign for the points measured on Etna as well as for the International GPS Service (IGS) stations.

The velocities are radially distributed (Figure 1) and seem to be organized as the result of a punctual source in a overpressure state located beneath Mt. Etna. As the state of this deep source was already discussed by Patane *et al.*, (2000), we have chosen to model the velocity field associated to the over-pressure of a Mogi point source (Mogi, 1958).

The best-fit solution of the Mogi point is located near the summit of the volcano (East 499.0 km, North 4180.5 km UTM33) located  $9.5 \pm 1\text{km}$  beneath the summit assuming a vertical maximal velocity of  $80 \pm 5\text{mm/y}$  (Figure 2). The depth of this source is in agreement with the results of several studies carried out by modeling ground deformation data (both GPS and INSAR) (Bonaccorso *et al.*, 1996, Lanari *et al.*, 1998, Puglisi *et al.*, 2001, Bonforte *et al.*, 2003, Lundgren *et al.*, 2003, Lundgren *et al.*, 2004). The vertical accuracy of the GPS velocities were not accurate enough to test the impact of the topography of the volcano on our modelling. However, the numerical simulations of the impact of the topography on the deformation field allow us to estimate that the computed vertical maximal inflation were overestimated of 30 per-

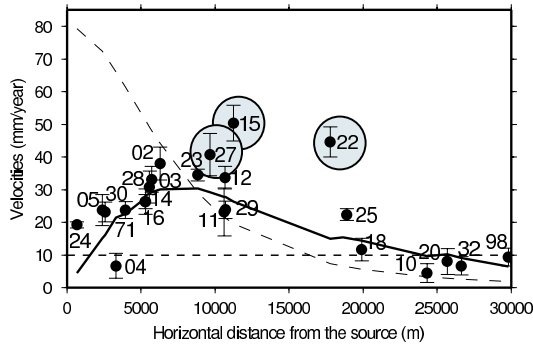


Figure 3.31: Data (black filled circles) and best model (black lines) plotted versus the horizontal distance from the source (Mogi, 1958). The computed horizontal displacements are symbolized by a continuous black line while the vertical one by a dashed one. Three sites dynamics don't fit with the modeled displacements (15, 22 and 27). Those are highlighted by grey filled black circles.

cent near the summit ( $24\text{mm/yr}$ ).

The point source model explains the observations except in the eastern part of the volcano (Sites 15 and 22) and along the Pernicana fault system (Site 27, Figure 3.31). The fact that the model doesn't fit exactly in the eastern part of the network along the Ionian coast is in agreement with the eastward movement of the eastern part of the volcano toward the sea (Rasa et al., 1996, Froger et al., 2001, Puglisi et al., 2003). The magnitude of the site 15's velocity ( $11\text{mm/y}$  to the East) supports the hypothesis of the existence of a large slough located along the Ionian coast limited by the Pernicana fault to the north, Ionian coast to the East and Timpe fault system to the West. The volume of this slough was estimated from  $5$  to  $50\text{km}^3$  (Houlié, 2005) while the mechanism driving the dynamic of these units is not clearly identified yet.

## 16.3 References

Azzaro, R., S. Branca, S. Giammanco, S. Gurrieri, R. Rasà, and M. Valenza (1998), New evidence for the form and extent of the Pernicana fault system (Mt. Etna) from structural and soil-gas surveying, *J. Volcanol. Geotherm. Res.*, *84*, 143–152.

Azzaro, R., S. Barbano, M., R. Rigano, and S. Vinciguerra (2001a), Time seismicity patterns affecting local and regional fault systems in the Etna region; preliminary results for the period 1874–1913, *Journal of the Geological Society of London*, *158*, 561–572.

Azzaro, R., M. Mattia, and G. Puglisi (2001b), Fault creep and kinematics of the eastern segment of the Pernicana fault (Mt. Etna, Italy) derived from geodetic observations and their tectonic significance, *Tectonophysics*, *333*(3–4), 401–415.

Branca, S., and P. Del Carlo (2004), Eruptions of Mt.

Etna During the Past 3,200 Years: A Revised Compilation Integrating the Historical and Stratigraphic Records, in *Mt. Etna: Volcano observatory, Geophysical Monograph Series 143*, pp. 1–27.

Calvari, S., L. H. Tanner, and G. Groppelli (1998), Debris-avalanche deposits of the milo lahar sequence and the opening of the Valle del Bove on Etna volcano (Italy), *J. Volcanol. Geotherm. Res.*, *87*, 193–209.

Jacques, E., C. Monaco, P. Tapponnier, L. Tortorici, and T. Winter (2001), Faulting and earthquake triggering during the 1783 Calabria seismic sequence, *Geophys. J. Int.*, *147*, 499–516.

Herring, T. (2005), *GLOBK: Global Kalman Filter VLBI and GPS Analysis Program, version 10.2*.

Houlié, N. (2005), Mesure et Modélisation de données GPS de volcans. Applications à des études de déformation à diverses échelles et à la tomographie des panaches atmosphériques., Ph.D. thesis, Institut de Physique du Globe de Paris.

King, R., and Y. Bock (1999), *Documentation of the GAMIT software*, MIT/SIO.

Laigle, M., A. Hirn, M. Sapin, J. Lepine, J. Diaz, J. Gallart, and R. Nicolich (2000), Mount etna dense array local earthquake p and s tomography and implications for volcanic plumbing, *J. Geophys. Res.*, *105*, 21.

Mogi, K. (1958), Relations between the eruption of various volcanoes and the deformations of the ground surfaces around them, *Bull. of the Earthquake Research Institute*, *36*, 99–134.

Monaco, C., P. Tapponnier, L. Tortorici, and P. Y. Gillot (1997), Late quaternary slip rates on the acireale-piedimonte normal faults and tectonic origin of mt. etna (sicily), *Earth & Planet. Sc. Lett.*, *147*, 125–139.

Nicolich, R., M. Laigle, A. Hirn, L. Cernobori, and J. Gallart (2000), Crustal structure of the ionian margin of sicily; etna volcano in the frame of regional evolution, *Tectonophysics*, *329*, 121–139.

Patane, D., P. De Gori, C. Chiarabba, and A. Bonaccorso (2003), Magma ascent and the pressurization of mount etna's volcanic system, *Science*, *299*, 2061–2063.

Puglisi, G., P. Briole, M. Coltelli, A. Ferretti, C. Prati, and R. Rocca (2003), ERS SAR PS analysis provides new insights on the long-term evolution of Mt. Etna volcano, *Fringes 2003 proceedings*.

Puglisi, G., P. Briole, and B. A. (2004), Twelve Years of Ground Deformation Studies on Mt. Etna Volcano Based on GPS Surveys, in *Mt. Etna: Volcano observatory, Geophysical Monograph Series 143*.

Tibaldi, A., and G. Groppelli (2002), Volcano-tectonic activity along structures of the unstable NE flank of Mt. Etna (Italy) and their possible origin, *J. Volcanol. Geotherm. Res.*, *115*, 277–302.

## 17. Parkfield-Hollister Electromagnetic Monitoring Array

Karl Kappler, H. Frank Morrison, Gary D. Egbert

### 17.1 Introduction

The primary objective of the UC Berkeley electromagnetic (EM) monitoring array is to identify EM fields or changes in ground conductivity that might be associated with earthquakes. The array has consisted of up to three sites operating since 1995 at SAO, PKD, and PKD1, each of which measures three orthogonal components of the magnetic field and two orthogonal components of the electric field. Multiple sites are necessary in order to separate the fields of a local source (e.g., an earthquake signal, cultural noise) from the natural regional micropulsations [Gamble 1979]. Our approach has been to determine the transfer function between fields at different sites for periods of normal background EM variations and then use this transfer function to predict fields between sites. Differences between the observed and predicted fields are used to search for anomalous local fields.

### 17.2 MT Overview

In 1995 we installed two well-characterized electric and magnetic field measuring systems at two sites along the San Andreas Fault which are part of the Berkeley Digital Seismic Network. Since then, magnetotelluric (MT) data have been continuously recorded at 40 Hz and 1 Hz and archived at the NCEDC (references to these data channels can be found in the 2003 BSL Annual Report). At least one set of orthogonal electric dipoles measures the vector horizontal electric field,  $E$ , and three orthogonal magnetic sensors measure the vector magnetic field,  $B$ . These reference sites, now referred to as electromagnetic (EM) observatories, are co-located with seismographic sites so that the field data share the same time base, data acquisition, telemetry and archiving system as the seismometer outputs.

The MT observatories are located at Parkfield (PKD1, PKD), 300 km south of the San Francisco Bay Area and Hollister (SAO), halfway between San Francisco and Parkfield (Figure 3.32). In 1995, initial sites were established at PKD1 and SAO, separated by a distance of 150 km, and equipped with three induction coils and two 100 m electric dipoles. PKD1 was established as a temporary seismic site, and when a permanent site (PKD) was found, a third MT observatory was installed in 1999 with three induction coils, two 100 m electric dipoles, and two 200 m electric dipoles. PKD and PKD1 ran in parallel for one month in 1999, and then the MT observatory at PKD1 was closed.

Data at the MT sites are fed to Quanterra data loggers, shared with the collocated BDSN stations, synchronized

in time by GPS, and sent to the BSL via dedicated communication links.

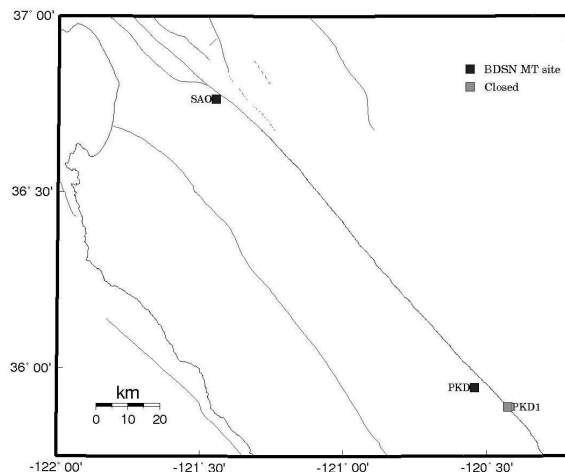


Figure 3.32: Map illustrating the location of operational (filled squares) and closed (grey squares) MT sites in central California.

### 17.3 2005-2006 Activities

Over the past year, limited maintenance has been performed at Parkfield. Resources have been invested in generating a report regarding array observations near the time of the Sept. 28, 2004 Parkfield Earthquake.

### 17.4 Data Processing

We have applied a variety of signal processing techniques to the 1sps array data. The 'raw' data stored on the NCEDC is windowed, Fourier transformed, and then band averaged, such that the time series of each data channel is represented by 25 shorter timeseries of band averaged Fourier coefficients (FCs). Details of the transform and band averaging can be found in *Eisel and Egbert (2001)*. The majority of the signal processing applied to date is done using these FC files as the input time series, although some time-domain Weiner Filtering has been applied to the data around the time of the earthquake. An example of the time domain processing is given in the PKD-SAO EM Monitoring Array chapter of the 2003 BSL Annual Report.

The FC time series are first examined in terms of Signal to Noise Ratio (SNR). Robust estimates of SNR

have been calculated daily over the four-year time window [2002-2005] for all 12 channels of data acquisition. The method of outlier downweighting used is called the RMEV estimation process (Robust multivariate errors-in-variables) and is referenced in *Eisel and Egbert (2001)*. These plots show that the electric field SNRs at both sites correlate positively with global geomagnetic activity indices ( $K_p$  and  $A_p$ ), and the Parkfield electric field SNRs correlate negatively with rainfall events.

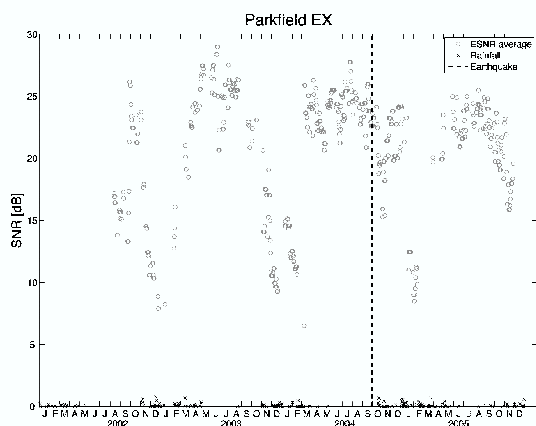


Figure 3.33: The only excessive spikes in the electric field SNR correlate with anomalously high geomagnetic indices. Note the trend towards poor SNR during the rainy season.

The second step of the analysis is the calculation of robust estimates of apparent resistivity curves for Parkfield. These plots showed slight seasonal variation of apparent resistivity on the order of a few percent that also seem to correlate with rainfall. A distortion analysis applied to these curves [*Smith 1995*], where the MT impedance tensor  $Z(\omega, t)$  is decomposed into a frequency-dependent and a time-dependent part, shows that the seasonal variation is almost entirely accounted for by a frequency independent distortion tensor, and hence is a near-surface effect. This suggests that if any regional variation in apparent resistivity occurred coincident with the earthquake, that it is small enough to be masked by the seasonal effect. Robust RMEV techniques were applied in this analysis, and are similarly documented in *Eisel and Egbert (2001)*.

The other two lenses through which we have carefully examined the 1Hz data are the use of Principal Components Analysis (PCA) and canonical coherence analysis (CCA), both of which are derived from the data covariance matrices. These techniques rely on rotating the coordinates of the data-space into directions of dominant characteristics. A discussion on the implications of PCA as applied to magnetotelluric data can be found in *Egbert (1989)*. A discussion of the significance of CCA as

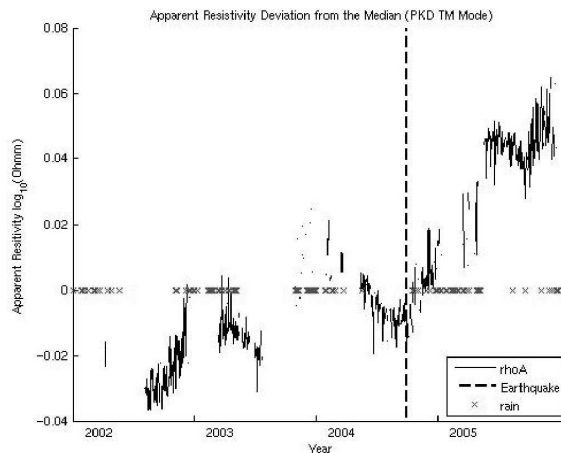


Figure 3.34: Note the offsets in the apparent resistivity which are coincident with times of site maintenance and instrument changes. These offsets are likely responsible for the linear upward trend. A seasonal trend is apparent.

applied to ULF EM data is included in *Kappler et. al. (2006)*.

## 17.5 Implications and Future Work

The 1Hz data do show several interesting characteristics, such as the seasonal dependence of apparent resistivity and the rainfall correlation. In particular an examination of the apparent resistivity residual TS with the distortion effects removed has not been plotted to date. Also the 3rd and 4th principal components, as well as canonical coherences, are of interest in understanding sources of signal contamination, as these monitor the non-regional signals that the array is detecting. An examination of the 40Hz data in a short time-window around the earthquake (2 months on either side) remains to be done in order to see if any anomalous EM signals were occurring at higher frequencies. A statistical analysis of the time-domain residuals has been started for the 1Hz data, and will need to be summarized, and also performed with the 40Hz data. Though several interesting signals have been detected and isolated from the data, we have not detected any clear evidence for anomalous EM activity preceding earthquakes. Significant EM fields are detected coseismically (during ground shaking) and modeling of these fields has begun as a project for the 2006 SEG annual meeting.

## 17.6 Acknowledgments

Frank Morrison directs the MT program and collaborates closely with Gary Egbert of Oregon State University. Rich Clymer and Karl Kappler also contribute to the operation of the MT observatories.

## 17.7 References

Egbert, G.D., Booker, J.R., (1989), Multivariate Analysis of Geomagnetic Array Data 1. The Response Space, *Journal of Geophys. Res.* V94 No.B10 pp14227-14247

Egbert G. D. (1997), Robust multiple-station magnetotelluric data processing, *Geophys. J. Int.* v130 pp475-496

Eisel M., Egbert G.D., (2001), On the stability of magnetotelluric transfer function estimates and the reliability of their variances, *Geophys. J. Int.* v144, pp65-82

Gamble T.D., Goubau W.M., Clarke J. (1979), Magnetotellurics with a remote reference, *Geophysics*, v44, pp53-68

Kappler, K. Egbert, G.D., Morrison, H.F., Long-Term Analysis of ULF electromagnetic fields at Parkfield CA, *in progress*

Smith, J. T., (1995), Understanding Telluric Distortion Matrices, *Geophysical journal International*, v122, 219-226

# 18. Observation and Analysis of Vertical Electric Fields in the Earth

Karl Kappler, H. Frank Morrison

## 18.1 Summary

We have been measuring and recording natural horizontal electric and magnetic fields at two sites on the San Andreas Fault near Parkfield and Hollister, California for the past ten years. The objective of the monitoring program was to determine objectively whether anomalies in either of these fields, or in the impedance of the ground, were observed in association with earthquakes on the San Andreas Fault. As part of a more general plan to study the behavior of the natural ULF and ELF fields, we installed a pair of electrodes in a vertical borehole used to deploy a deep three-component seismometer. The vertical dipole was connected to a spare channel of the seismic acquisition system and recorded along with the regular horizontal E and H data in the period from 01 July 2004 to 01 November 2005. The vertical field data displayed a long-term drift over the first few months of operation and a strong diurnal component as well as small variations (micropulsations) typically seen in the horizontal electric fields. We also discovered four striking variations of a few days duration in the recording. These anomalous fields stand out dramatically above the normal micropulsation signals. These signals are significant because: a) There is no counterpart variation in the horizontal electric fields at a station only 1.6 km away; b) No signals like this have been seen on the horizontal electrodes at any time; c) There were no rainfall events immediately prior to any of these anomalous variations; d) No particular pumping or hydrofracture experiments were conducted on the nearby SAFOD deep drilling site at these times. We propose to connect two more vertical dipoles to the network and to acquire two years of observations of this newly discovered phenomena. The horizontal field arrays will be maintained to provide the complimentary data to the three vertical dipoles. In addition we have access to the data from five volumetric strainmeters, at least two tiltmeters, and a long period seismograph all in the vicinity of the vertical electric dipole holes. The objective of the proposal is to study the relationship between vertical electric fields and the other geophysical data to try and determine the cause of the vertical field anomalies. Additionally, through a study of the ionospheric electron content provided by the GPS array, we will investigate whether there is a relationship between the vertical electric fields and ionospheric properties.

## 18.2 Existing Sites and Instrumentation

The borehole, which is equipped a vertical electric dipole, is labeled as CCRB in Figure 3.35. The site

is between the SAFOD borehole and the PKD electromagnetic observatory. Apart from the orientation of the dipole, the instrumentation and data logging are identical to that described in the Parkfield-Hollister Monitoring Array chapter of this issue.

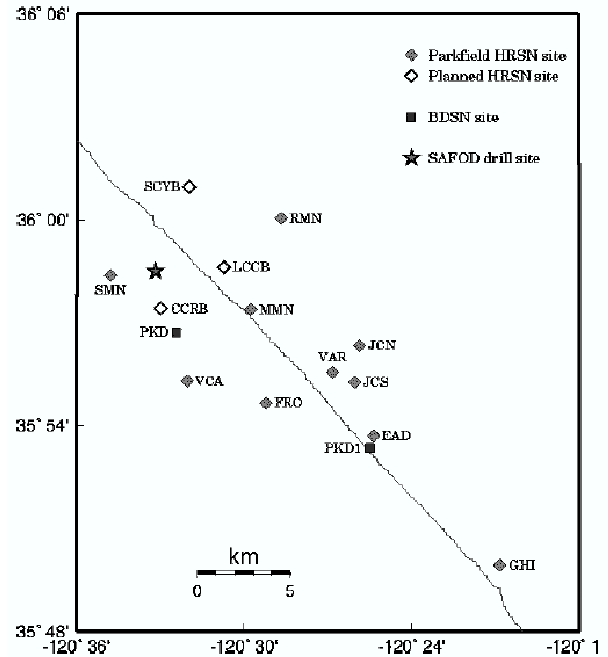


Figure 3.35: Location of borehole network, also showing SAFOD borehole, and PKD ULF observatory, and various other sites with geophysical data acquisition equipment.

## 18.3 Vertical Electric Dipole Data

The long term timeseries of the vertical electric dipole data is displayed in Figure 3.36. For brevity we include zoom-plots of only the first anomaly labeled as A.

The sharp offset depicted in Figure 3.37 looks suspiciously like an instrument step at this scale, but a closer inspection (Figure 3.38) shows that the onset of the step is in fact smooth.

The sharp corner also shows itself to be smooth in time when the 40Hz data are examined over short time intervals.

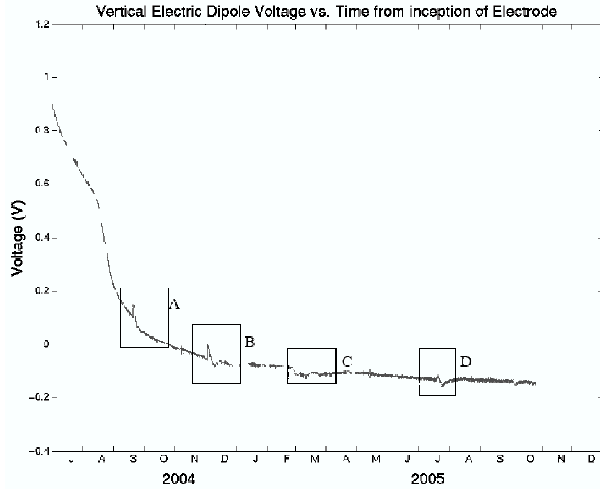


Figure 3.36: The vertical electric field data spanning 16 months of acquisition, mean subtracted. Boxes A-D indicate significant anomalies in the data stream.

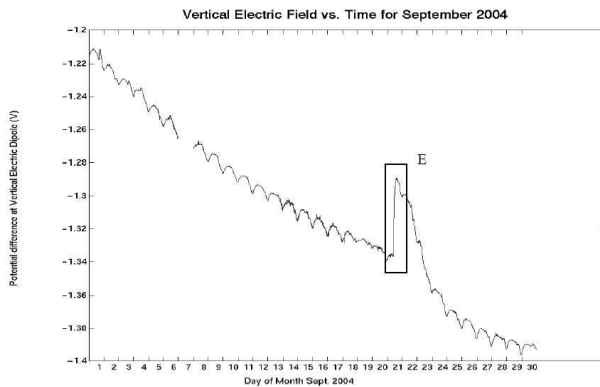


Figure 3.37: A closer look at the first spike in September 2004, shown above in box A.

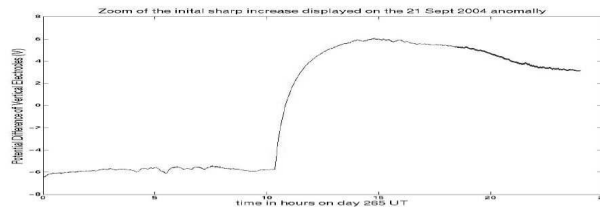


Figure 3.38: Shows the onset of the 21 September 2004 anomaly. The rise-time appears to be on the order of several hours. Once corrected for instrument response the rise is about 10mV.

## 18.4 Preliminary Analysis

We have found only two previous studies on measurements of vertical electric fields in the ground, at depths below the near-surface soil/unconsolidated materials. *Colangelo et. al.* (2005) report on data from a shallow pair of electrodes. The data is noisy as would be expected when at least one electrode is in a near surface layer where surface moisture and chemistry is highly variable, temperature effects are strong and local streaming potentials are prevalent. *Corwin* (1990) presents a good review of the factors that can cause time variations of tens of millivolts in shallow electrode systems. None of these factors seem relevant for electrodes buried below the water table at depths of 100 or 200 meters. *Antonopoulos et. al.* (1993) report vertical electric fields from two adjacent drill holes on an island in Greece. The electrodes at depth were at 200m, but the upper electrodes were at the surface and, as noted above, subject to variations due to the near surface layer. Nonetheless, both vertical electrodes showed high coherence to a horizontal dipole many miles away, basically showing the same relationship between horizontal and vertical fields that we discussed above for our data. In addition, they claim that anomalous vertical fields were seen, related to distant horizontal fields of similar waveform, that were not related in the same manner as the magnetotelluric fields. These anomalous fields were of 15-20 minute duration and were claimed to be related to distant earthquakes. No anomalies of the type we report were described in their paper.

The anomalous variations seen in Figure 3.36 are well above the background micropulsation variations and are readily identified by eye. It is entirely possible that there are smaller variations down to the level of the micropulsations that are not coherent with the horizontal fields and are indicative of this new vertical field phenomenon. We have developed analysis techniques for the horizontal array studies that can identify such phenomena. In general, *Egbert* (1989) and *Booker and Egbert* (1989), have shown that all the components of electric and magnetic field measured on the surface of the ground that are caused by widespread sources in the ionosphere/magnetosphere are related by simple tensor forms. For example orthogonal electric fields at site A are related to orthogonal electric fields at site B by a simple 2x2 tensor. Over time this transfer function can be determined accurately. It is a function only of the conductivity distribution in the ground and has been found to be generally time invariant. Following similar reasoning the relationship between the vertical field and the orthogonal horizontal fields is described simply by a spectral transfer function of the form:

$$E_z = T_{xz}E_x + T_{yz}E_y \quad (3.1)$$

where  $E_i$  represents the  $i$ th component of electric field,

and  $T$  is a simple  $1 \times 2$  tensor. The multiple coherence between  $E_z$  and the horizontal components provides a measure of the noise in the measurement of the  $E$  s. An estimation of this transfer function can be made during a time of good data quality and then used to predict the fields at one site from those at another. The difference between the measured and predicted fields, which we labeled as a residual, becomes a measure of the fields at one site that are not components of the micropulsation source. Of course there is always a residual, which is the noise level of the measurements. So anomalous fields can be assigned a quantitative signal to noise level. *Egbert* (2000, 1997, and 1986) generalized this idea so as to use all the field components measured in two arrays to predict the fields in any one component of either array. This was the basic approach used with the ULF array in an attempt to isolate anomalous electric or magnetic fields that might have been generated by some earthquake related process local to one of the sites. This concept can also be applied in the time domain to yield estimates of electric field as a function of time. In this project we propose to calculate the time domain residuals in the vertical fields using the horizontal components of  $E$  and  $H$  at site PKD for the reference site. In this way other anomalies of a much smaller scale than the large ones highlighted in Figure 3.36 can be quickly identified.

## 18.5 Theory

The cause of these vertical field variations is not known. By measuring something that no one seems to have measured before, we may have discovered an interesting process within the earth or a heretofore unexpected coupling between the earth and the ionosphere. At the very low frequencies considered here, conventional wisdom suggests that there are no vertical electric fields at or within a conductor below free space that has an electric charge or field distribution. Within an inhomogeneous half space, there may, of course, be vertical components of the electromagnetically induced telluric currents which, in fact, we do observe.

The simplest explanation is that the observed vertical fields arise from the charge separation that occurs from the streaming potential phenomenon accompanying the development of a vertical pressure gradient. There are two possible sources for such a vertical pressure gradient: a) atmospheric loading leading to the diffusion of a pressure front into the earth or b) a reduction of pressure within the earth due to a dilatational strain. We briefly analyzed the first of these possibilities by plotting the atmospheric pressure variations at station VCA (Figure 3.35), 4.5 km from CCRB in Figure 3.39. In general the vertical field does not track the pressure variations.

*Pride* (2004) has recently shown that fluid sources or sinks within the ground will only produce vertical electric fields near the surface, not horizontal fields. Local

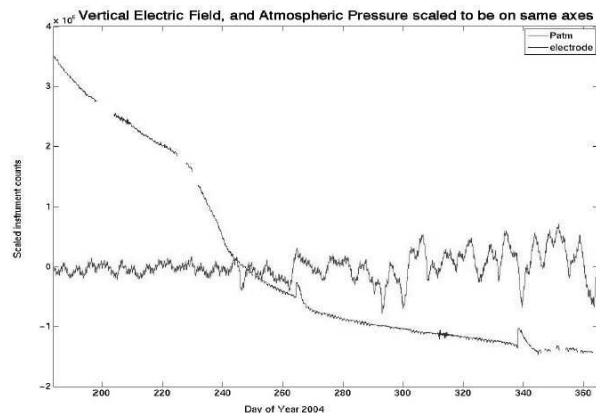


Figure 3.39: Variations of atmospheric pressure plotted together with variations in electric field. No clear correlation between the two signals stands out. The y-axis represents scaled instrument counts, and is only a qualitative measure.

fluid flow transients near the well bore could also cause streaming potentials, but the lack of any correlation with local rainfall and the long time scale of the variations argues against this explanation. *Pride* (2004) also argues that large-scale strain changes after an earthquake should produce long term variations in the streaming potentials with accompanying measurable vertical fields. A cursory examination of the vertical field data after the Parkfield ( $M= 6.0$ ) earthquake on 28 September 2004 (day 272 UT), shows no such trends. A dilatancy strain could certainly produce vertical pressure gradients with associated vertical streaming potentials. We would expect to see some evidence of this in local measurements of strain. We examined the uncorrected strain data from VCA and found, as expected, that the strain tracks the atmospheric pressure changes and the local tidal strain. No anomalous strain associated with the electric field anomalies could be seen in the raw data. We propose to examine the corrected strain data from these sites at the times of the vertical field anomalies. After correction for tidal and atmospheric loading, the noise level for these strainmeters is approximately 0.1 nanostrain [*Malcolm Johnston*, USGS, personal communication, 2006]. These data and the vertical field and ULF array data are directly available from the NCEDC. Another intriguing possibility is that there is some electrical coupling among very low frequency gravity waves, ionospheric properties, local strain and the vertical electric field. *Calais and Minster* (1995) report on the detection of ionospheric perturbations caused by atmospheric-ionospheric-acoustic-gravity waves that were generated by the ground displacement of the 1994 Northridge earthquake. The ionospheric anomalies were found from an analysis of the phase delays on

the two GPS frequencies, which are, in turn, proportional to the electron content of the ionosphere. More subtle transient ground displacements, on the order of 3-5 days, might consequently generate GPS phase delays corresponding to the vertical electric field. As mentioned above it is unlikely that ionospheric fluctuations of such a timescale, essentially electrostatic, could themselves cause the observed fields within the conductive earth.

## 18.6 Future Analysis

We have submitted an NSF proposal to monitor the vertical electric fields at three sites (LCCB, SCYB, CCRB). We intend to calculate the time domain residuals in the vertical fields using the horizontal components of E and H at site PKD (Figure 3.35) for the reference site. In this way other anomalies of a much smaller scale than the large ones highlighted in Figure 3.38 can be quickly identified. Other geophysical measurements that are available to correlate with the anomalous vertical fields basically break into ground and ionospheric. On the ground we have access to the following measurements in the vicinity of the PKD site:

1) The broadband seismometer co-located with the ULF monitoring sensors at PKD. 2) Tiltmeters located at VAR and GHI on Figure 3.35.

3) Volumetric strainmeters located at FRO and VCA on Figure 3.35., and also at three other sites (DLT, JCN, RHL, not shown) within 40 km.

4) Long period magnetic field observations from Fresno Magnetic observatory

## 18.7 References

Antonopoulos, G., Kopanas, K., Eftaxias, K., Hadjicostas, V., 1993, On the experimental evidence for SES vertical component, *Tectonophysics*, v224, 47-49

Boyd, O.S., Egbert, G.D., Eisel, M., Morrison, H.F., 1997, A preliminary analysis of EM field monitoring network. *EOS Trans.* 78 AGU, p459

Calais, E., Minster, J.B., 1995, GPS detection of ionospheric perturbations following the January 17, 1994, Northridge earthquake, *Geophysical Research Letters*, v22, no. 9, 1045-1048

Calais, E., Haase, J.S., 2003, Detection of ionospheric perturbations using a dense GPS array in Southern California, *Geophysical Research Letters*

Colangelo, G., Lapenna, V., Telesca, L., 2005, Vertical dipoles to detect self potential signals in a seismic area of southern Italy: Tito station, *Natural Hazards and Earth System Sciences*, v5, 667-671

Corwin, R.F. 1990, The self Potential method for environmental and engineering applications, *Geotechnical and Environmental Geophysics*, v1 SEG Tulsa, OK

Eisel, M., Egbert, G.D., 2001, On the stability of magnetotelluric transfer function estimates and the reliabil-

ity of their variances, *Geophysical Journal International*, v144, 65-82

Egbert, G.D., Booker, J.R., 1986, Robust estimation of geomagnetic transfer functions, *Geophysical Journal of the Royal Astronomical Society*, v87, 173-194

Egbert, G.D., Booker, J.R., Schultz, A., 1992, Very Long Period Magnetotellurics at Tucson Observatory: Estimation of Impedances, *Journal of Geophysical Research*, v97, no. B11, 15113-15128

Egbert, G.D., Booker, J.R., 1989, Multivariate Analysis of Geomagnetic Array Data 1. The Response Space, *Journal of Geophysical Research*, v94, no. B10, 14227-14247

Egbert, G.D., 1989, Multivariate Analysis of Geomagnetic Array Data 2. Random Source Models, *Journal of Geophysical Research*, v94, no. B10, 14249-14265

Egbert, G.D., 1997, Robust multiple-station magnetotelluric data processing: *Geophysical Journal International*, v130, 475-496

Egbert, G.D., Eisel, M., Boyd, O.S., and Morrison, H.F., 2000, DC trains and Pc3s: Source effects in mid-latitude geomagnetic transfer functions, *Geophysical Research Letters*, v27, no. 1, 25-28

Kappler, K.N., Egbert, G.D., Morrison, H.F., 2005, Long Term Monitoring of EM Signals Near Parkfield CA, AGU paper Fall Meeting 2005

Kappler, K.N., Egbert, G.D., Morrison, H.F., 2006, Results of long term EM monitoring at Parkfield CA, (in progress)

Morrison, H.F., 2004, Anomalous em signals and changes in electrical resistivity at parkfield: collaborative research between the universities of California at Berkeley and Riverside and Oregon State University, Final Technical Report to USGS, 01HQGR0060

Morrison, H. F., Fernandez, R., 1986, Temporal Variations in the electrical resistivity of the Earth's Crust, *Journal of Geophysical Research*, v91, no. B11, pp. 11618-11629.

Nichols, E.A., Morrison, H. F., Clarke, J., 1988, Signals and noise in measurement of low-frequency geomagnetic fields: *J.G.R.*, v93, no. B11, pp. 13,743-13,754.

Pride, S.R., 1994, Governing equations for the coupled electromagnetics and acoustics of porous media, *Physical Review B*, v50, no. 21

Pride, S.R., Moreau, F., Gavrilenco, P, 2004, Mechanical and electrical response to fluid pressure equilibration following an earthquake, *Journal of Geophysical Research*, v109, B03302

# 19. Surface Deformation and Fault Kinematics of the San Francisco Bay Area from PS-InSAR Analysis

Gareth Funning and Roland Bürgmann

## 19.1 Introduction

The aim of this project is to use high-precision geodetic data to characterize, and subsequently model, the surface deformation field of the San Francisco Bay Area. In so doing we hope to recover information about the fault kinematics of the region, the distribution of creeping and locked areas on the Hayward fault, and also about the sources of nontectonic deformation (such as landsliding, subsidence and aquifer recharge) around the Bay, and thus improve our knowledge of the whereabouts and mechanisms of the principal natural hazards in the region. This study builds upon previous work by members of the Active Tectonics group at the Berkeley Seismological Laboratory (*Schmidt and Bürgmann, 2003, 2005; Hilley et al., 2004; Ferretti et al., 2004; d’Alessio et al., 2005; Bürgmann et al., 2006*).

## 19.2 PS-InSAR

Permanent Scatterer Interferometric Synthetic Aperture Radar (PS-InSAR) is a sophisticated geodetic technique that can be used to construct spatially dense datasets detailing the rates of surface deformation over wide ( $\sim 100 \times 100$  km) areas (*e.g. Ferretti et al., 2004*). The technique differs from conventional InSAR in that it uses information from features on the ground – typically buildings or other man-made structures, but also natural features such as rock outcrops – which can act as permanent reflectors of incident radar radiation. These can be identified even when surrounded by vegetation, allowing a substantial improvement in coverage in areas such as the East Bay Hills which are poorly suited to conventional InSAR. A further benefit of the PS-InSAR technique is the ability to mitigate noise sources using spatial and temporal filtering. By making certain assumptions – that surface deformation is correlated in time but not in space, and that atmospheric signals are correlated over small spatial wavelengths ( $< 20$  km) but not in time – it is possible to decompose the radar signal into deformation and atmospheric components, and thus to eliminate the main source of uncertainty in the measurements.

The PS-InSAR data presented here were processed by our long-standing collaborators at Tele-Rilevamento Europa (TRE), Milan, Italy. One of us (GF) visited Milan in the past year to learn about PS-InSAR methods in detail and to supervise data processing. We are also exploring the possibility of using one of the few freely-available codes (*e.g. Hooper et al., 2004*) in order to have our own in-house processing capability in future.

## 19.3 Data

We analyse data from two sources – the European Space Agency ERS satellites (49 descending track radar image acquisitions from 1992-2000), and the Canadian Radarsat platform (31 ascending track images from 2001-2004). Both data sets are plotted in Figure 3.40. Each data set provides a dense coverage of surface velocity observations in the line-of-sight direction of the satellite. Given the different viewing geometries of the two data sets, if we assume that the rates of displacement do not vary with time, we can use the two independent measurements to infer the horizontal and vertical deformation rates across the region.

## 19.4 Creep on the Hayward fault

The Hayward fault is currently considered to pose the greatest threat of a  $M \sim 7$  earthquake of the major faults of the San Francisco Bay Area (*Working Group on California Earthquake Probabilities, 2003*). The fault creeps at the surface – this can be seen in both PS-InSAR data sets as an abrupt change in velocity either side of a linear feature (Figure 3.40). Knowledge of the extent and magnitude of creep at depth is important for understanding the future seismic hazard posed by the structure; areas of very low ( $< 2$  mm/yr) or zero creep can be considered locked, and therefore in potential danger of rupture in future.

We model the distribution of creep on the Hayward fault using elastic dislocation modeling (*Okada, 1985*), assuming a vertical fault geometry with a surface trace matching that of the mapped fault, subdivided into  $2 \times 2$  km patches, and applying Laplacian smoothing. The regional strain gradient is described by placing further, deep, dislocations beneath each of the major faults in the region. The velocity on each fault is inverted for using least squares methods with a positivity constraint to prevent retrograde motion. In addition to the PS-InSAR data, appropriately sub-sampled, we also invert GPS data from 185 sites across the region (*d’Alessio et al., 2005*), and surface creep rates measured at 18 alignment arrays along the trace of the Hayward fault (*Lienkaemper et al., 2001*).

Our model of fault slip is plotted in Figure 3.41a. We find evidence for a patch of very low/zero creep which extends between  $\sim 20$  and 58 km along-strike (measured southeast from Pt Pinole, where the fault trace goes offshore into San Pablo Bay), corresponding to the portion of the fault between south Oakland and Union City. The

overall pattern is similar to that obtained in other studies where characteristic repeating earthquake data are used to constrain creep behavior at depth (e.g. Schmidt et al., 2005). If we assume a long-term slip rate for the Hayward fault of 10 mm/yr, within the uncertainties of geologic estimates (e.g. Lienkaemper and Borchardt, 1996), this implies that this ‘locked’ portion of the fault is accumulating a moment deficit equivalent to a  $M_w$  6.74 event per century. If loading rates have been constant since the last event on the Hayward fault in 1868, the total deficit is equivalent to a  $M_w$  6.9 earthquake; this represents an upper bound of the size of any potential earthquake, as we do not know how much of the total moment deficit would be released aseismically as afterslip or accelerated creep following an earthquake.

This model generally fits the data well, with mean residuals of less than 1 mm/yr (Figure 3.41b). The most prominent residual features are uplift features seen in the Mt Diablo stepover and San Andreas fault restraining bend, which are consistent with the strike-slip fault geometries, but presumably occurring upon structures that we have not modeled in this study. We also see evidence in the Loma Prieta region of the San Andreas fault for continuing residual postseismic subsidence and contraction following the 1989 earthquake in this location. These findings are consistent with other attempts to identify vertical tectonic motions in the San Francisco Bay Area (e.g. Bürgmann et al., 2006).

## 19.5 Acknowledgements

We would like to thank our collaborators at TRE, especially Alessandro Ferretti, Fabrizio Novali and Chiara Giannico, for their continuing assistance with the PS-InSAR processing and with data acquisition/ordering issues. ERS data are copyrighted by the European Space Agency and supplied through the WInSAR consortium, and under project AOE 750. Radarsat data are copyrighted by the Canadian Space Agency and supplied under an agreement with the Alaska SAR Facility. This project is funded by grants from the National Science Foundation, and the National Earthquake Hazard Reduction Program.

## 19.6 References

Bürgmann, R., G. Hilley, A. Ferretti, and F. Novali, Resolving vertical tectonics in the San Francisco Bay area from GPS and Permanent Scatterer InSAR analysis, *Geology*, *34*, 221-224, 2006.

d’Alessio, M. A., I. A. Johanson, R. Bürgmann, D. A. Schmidt and M. H. Murray, Slicing up the San Francisco Bay Area: Block kinematics and fault slip rates from GPS-derived surface velocities, *J. Geophys. Res.*, *110*, B06403, doi:10.1029/2004JB003496, 2005.

Ferretti, A., C. Prati and F. Rocca, Permanent Scatterers in SAR Interferometry, *IEEE Trans. Geosci. Remote Sens.*, *39*, 8-20, 2001.

Ferretti, A., F. Novali, R. Bürgmann, G. Hilley and C. Prati, InSAR Permanent Scatterer Analysis Reveals Ups and Downs in San Francisco Bay Area, *EOS Trans. AGU*, *85*, 317, 2004.

Hilley, G. E., R. Bürgmann, A. Ferretti, F. Novali and F. Rocca, Dynamics of slow-moving landslides from permanent scatter analysis, *Science*, *304*, 1952-1955, 2004.

Lienkaemper, J. J. and G. Borchardt, Holocene slip rate on the Hayward fault at Union City, California, *J. Geophys. Res.*, *101*, 6099-6108, 1996.

Lienkaemper, J. J., J. S. Galehouse and R. W. Simpson, Long-term monitoring of creep rate along the Hayward fault and evidence for a lasting creep response to the 1989 Loma Prieta earthquake, *Geophys. Res. Lett.*, *28*, 2265-2268, 2001.

Okada, Y., Surface deformation due to shear and tensile faults in a half-space, *Bull. Seismol. Soc. Am.*, *75*, 1135-1154, 1985.

Schmidt, D. A. and R. Bürgmann, Time-dependent land uplift and subsidence in the Santa Clara valley, California, from a large interferometric synthetic aperture radar data set, *J. Geophys. Res.*, *108*, B9, 2416, doi:10.1029/2002JB002267, 2003.

Schmidt, D. A. and R. Bürgmann, Distribution of aseismic creep rate on the Hayward fault inferred from seismic and geodetic data, *J. Geophys. Res.*, *110*, B08406, doi:10.1029/2004JB003397, 2005.

Working Group on California Earthquake Probabilities, Earthquake probabilities in the San Francisco Bay Region: 2002 to 2031, *U.S. Geol. Surv. Open File Rep.*, *03-214*, 2003.

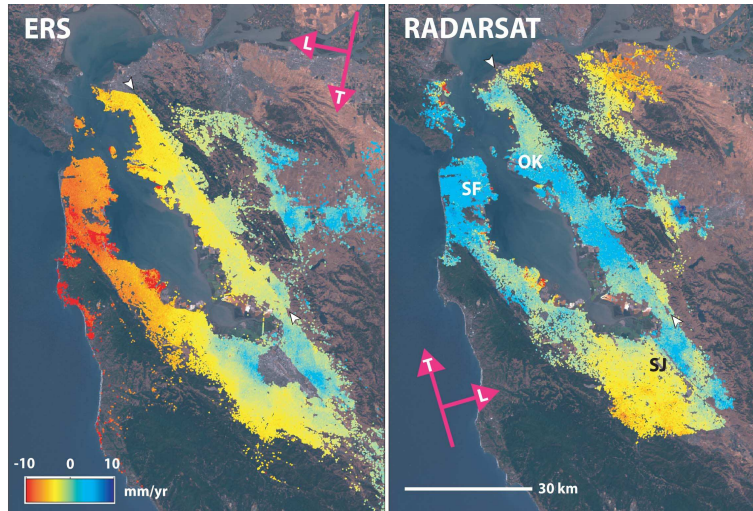


Figure 3.40: PS-InSAR velocities for the San Francisco Bay Area. Red colors indicate motion of the ground away from the satellite, blue colors motion towards. Where a feature has the same color in both datasets, surface deformation is vertical; where colors are opposite, deformation is horizontal. Pink arrows indicate track (T) and line-of-sight (L) directions for each satellite. White arrowheads show the location of the surface trace of the Hayward fault. [SF – San Francisco, OK – Oakland, SJ – San Jose]

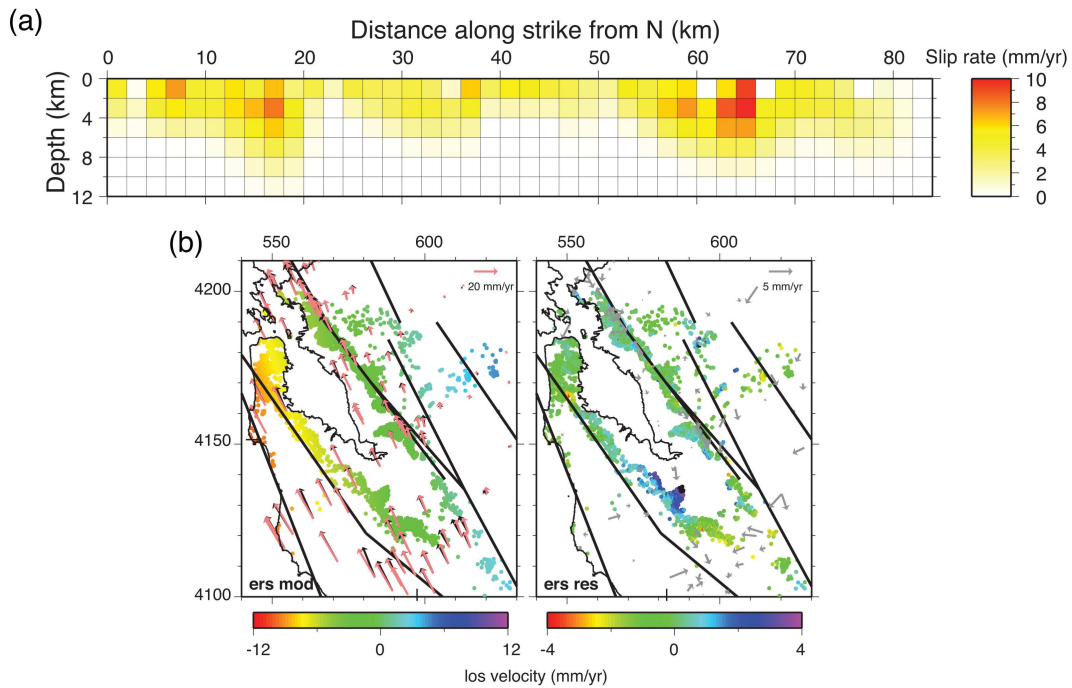


Figure 3.41: (a) Distribution of creep on the Hayward fault. Creep at the surface reaches a maximum of  $\sim 9$  mm/yr at Fremont ( $\sim 66$  km). The white area between 20 and 58 km along-strike is the area we believe to be locked. (b) Modeled (left) and residual (right) PS-InSAR and GPS velocities. Only ERS PS velocities are shown here for an example. Black arrows are BAVU GPS velocities, pink arrows show modeled GPS velocities, gray arrows show residual GPS velocities (note change in scale). Solid black lines are faults modeled in the inversion. Most residuals are of the order 1-2 mm/yr; prominent residual uplift features (blue colors) can be seen where there is unmodeled uplift occurring within stepovers and restraining bends of the fault. Coordinate system is UTM km, zone 10.

## 20. Slip of the 2004 Sumatra-Andaman Earthquake from Joint Inversion of Long Period Global Seismic Waveforms and GPS Static Offsets

Junkee Rhie, Douglas Dreger, Roland Bürgmann, and Barbara Romanowicz

### 20.1 Introduction

The December 26, 2004 Great Sumatra-Andaman earthquake is an important earthquake in many ways. It is the first great event ( $M_w > 9.0$ ) with sufficient data to allow for a detailed analysis of its complex source rupture process. For the first time, global very broadband seismic and geodetic measurements are available. In this study, we present a slip distribution over the finite fault plane constrained by global long period seismic waves and near-field GPS offsets.

### 20.2 Data and Inversion Method

We considered all three components of displacement waveforms recorded at 10 IRIS and GEOSCOPE stations within the epicentral range between  $43.6^\circ$  and  $65.2^\circ$  (Figure 3.42). The GPS offset data used for the inversion represent a 38 near-field subset of the 142 coseismic displacement measurements (*Banerjee et al., 2006*) (Figure 3.42). To account for several weeks of postseismic deformation prior to reoccupation of the GPS stations, we adjusted the offset estimates for near-field campaign-mode GPS sites in this dataset.

To invert data for the slip distribution, we use a widely used least-squares inversion. Here we used normal-mode computed Green's functions for seismic waveforms at teleseismic distances and FORTRAN programs ED-GRN/EDCMB (*Wang et al., 2003*) for GPS Green's functions for flat layered elastic structures. In both cases, PREM is used for the velocity structure. The seismic data and Green's functions were bandpass filtered between 100 and 500 sec. Since the rise time of each sub-fault is very short compared to the passband, we ignored the detailed variation in slip rise time of each sub-fault. The trigger time of each sub-fault is defined by the passage of circular rupture front with constant rupture velocity. In this study, we choose the rupture velocity of 2.5 km/s as it is consistent with other studies (e.g., *Ni et al., 2005*). A Laplacian-smoothing operator and slip positivity constraint are applied in all of the inversions and a weighting factor is applied to the GPS data set and Green's functions for optimal slip model explaining both seismic and GPS data sets.

### 20.3 Results and Discussion

We tested a geometry model, slightly modified from a previous study, constrained by aftershock distribution and the fit to the far-field GPS coseismic offsets (*Baner-*

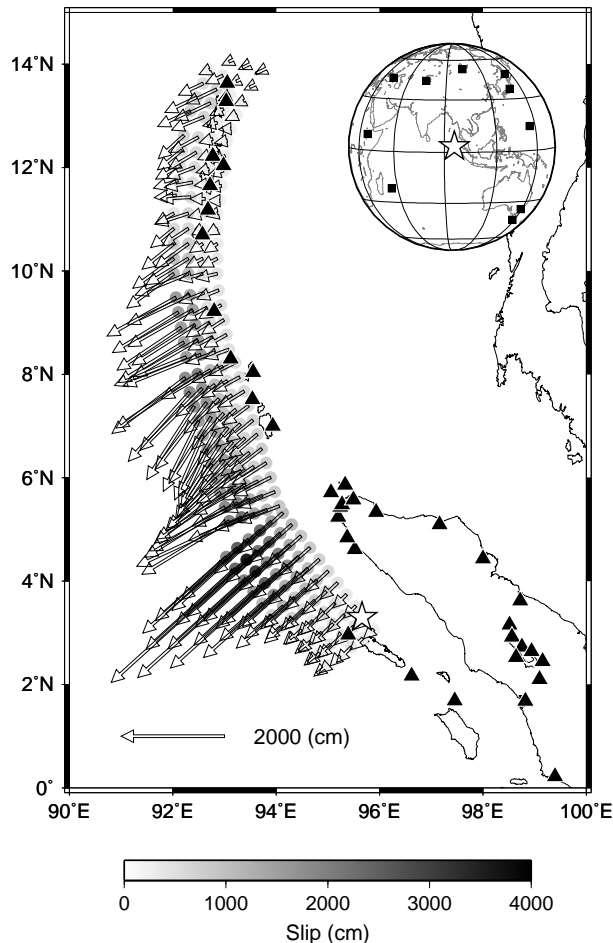


Figure 3.42: The preferred slip distribution model from joint inversion of seismic and GPS static offsets. Color represents total slip and the arrows show the slip vector. Black triangles indicate the locations of the near-field GPS sites and black squares in the small global map on the upper right show 10 selected global seismic stations used in joint inversion. A white star represents the epicenter both in local and global maps.

*jee et al., 2005*). In this study, we removed the steeper and deeper segments of the fault and made a simple fault geometry model because our data sets are not sensitive to a slight geometry change at deeper depth. The slip model inverted from only seismic waveforms shows large slip patches at around  $4^\circ$  N and a high-slip region with slip larger than 10 m extends only up to  $10^\circ$  N, and

its moment magnitude is 9.12. The joint inversion slip model including near-field GPS static offsets data basically keeps the trend of the slip distribution but increases the level of the slip over nearly the whole fault plane, and its seismic magnitude is determined to be  $M_w$  9.20 (for slip distribution see Figure 3.42).

To constrain key model parameters, we consider sensitivity tests for dip angles and rupture velocity, which are important parameters to understand the source process. Unfortunately our data sets are not very sensitive to these two parameters. While neither of the two parameters are well constrained in this study, distribution of aftershocks and several previous studies support that our dip angles and rupture velocity are reasonable (e.g., *Bilham et al.*, 2005; *Ni et al.*, 2005).

A precise estimate of model error is as important as a detailed slip distribution. An error analysis on our slip model is conducted by a random station selection method. We randomly select 50% of seismic and GPS stations and invert them for slip distribution and then repeat this process 10 times. By doing this, we estimate mean and standard deviation of moment magnitude and also slip at each sub-fault. The mean slip distribution is very similar to the slip distribution inverted from the whole data set. The estimate of mean seismic moment and 1 standard deviation error is  $9.19 - 0.02 / + 0.02$ .

To confirm our slip distribution model we compare forward GPS static offsets at far-field sites (Figure 3.43). We do not consider stations at  $> 1000$  km because of the large sphericity effect, which we did not consider in our Green's function computation. A forward prediction of GPS vectors at stations on Malaysian Peninsula shows that the slip model inverted using only seismic data significantly underestimates observed GPS offsets but the slip model from the joint inversion can predict observations nearly perfectly.

This indicates that after-slip correction to get coseismic static offsets for near-field campaign GPS offset data is correct and unaccounted post-seismic excess motion is small.

Our slip model from joint inversion is similar to slip models obtained from different data sets in the location of the largest slip patch and the extent of the large slip region (e.g., *Ammon et al.*, 2005). This largest slip patch is consistent with one of the tsunami source regions found by *Fine et al.*, [2005], and the northward extent of significant slip region is consistent with the tsunamigenic region suggested by *Lay et al.*, [2005].

## 20.4 Acknowledgements

We thank IRIS and GEOSCOPE for providing seismic data. GPS data used in this study were provided by the Survey of India (SOI), BAKO-SURTANAL, the Tectonic Observatory at Caltech, and the Indonesian Institute of Sciences (LIPI).

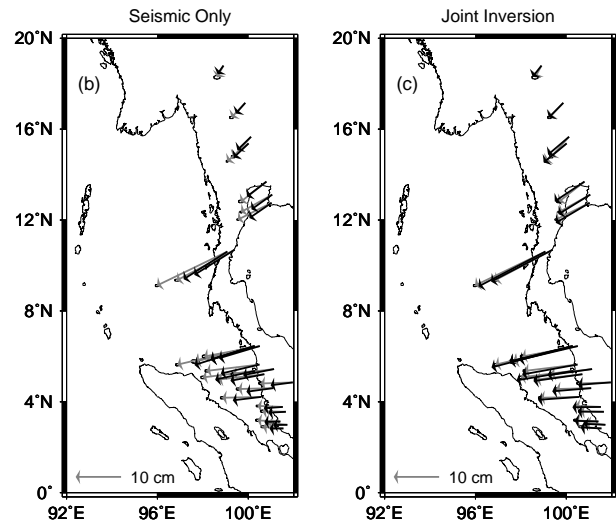


Figure 3.43: Comparison between observed (grey) and synthetic GPS vectors (black) for seismic only and joint inversion models.

## 20.5 References

- Ammon, C. J., C. Ji, H.-K. Thio, D. Robinsons, S. Ni, V. Hrorleifsdottir, H. Kanamori, T. Lay, S. Das, D. Helmberger, G. Ichinose, J. Polet, and D. Wald, Rupture Process of the 2004 Sumatra-Andaman Earthquake, *Science*, *308*, 1133-1139, 2005.
- Banerjee, P., F. Pollitz, and R. Bürgmann, The size and duration of the Sumatra-Andaman earthquakes from far-field static offsets, *Science*, *308*, 1769-1772, 2005.
- Banerjee, P., F. Pollitz, B. Nagarajan, and R. Bürgmann, Coseismic slip distribution of the 26 December 2005 Sumatra-Andaman and 28 March 2005 Nias earthquakes from GPS static offsets, *Bull. Seism. Soc. Am.*, 2006. (submitted).
- Bilham, R., R. Engdahl, N. Feldi, and S. P. Satyabala, Partial and Complete Rupture of the Indo-Andaman Plate Boundary, *Seismol. Res. Lett.*, *76*, 299-311, 2005.
- Fine, I. V., A. B. Rabinovich, and R. E. Thomson, The dual source region of the 2004 Sumatra tsunami, *Geophys. Res. Lett.*, *32*, L16602, doi:10.1029/2005GL023521, 2005.
- Lay, T., H. Kanamori, C. J. Ammon, M. Nettles, S. N. Ward, R. C. Aster, S. L. Beck, S. L. Bilek, M. R. Brudzinski, R. Butler, H. R. DeShon, G. Ekström, K. Satake, and S. Sipkin,
- Ni, S., H. Kanamori, and D. Helmberger, Energy radiation from the Sumatra earthquake, *Nature*, *434*, 582, 2005.

# 21. Inversion for the Velocity Structure of the Santa Clara Valley, California

David Dolenc, Doug Dreger, and Shawn Larsen (Lawrence Livermore National Laboratory)

## 21.1 Introduction

In our previous work, we have found strong correlations between basin depth reported in the USGS 3D seismic velocity model (ver. 2) (*Jachens et al.*, 1997) and different relative measures of ground motion parameters, such as teleseismic arrival delays, P-wave amplitudes, wave energy, local earthquake S-wave amplitudes, and periods of microseism horizontal to vertical spectral ratio peaks (*Dolenc et al.*, 2005; *Dolenc and Dreger*, 2005). The teleseismic, local earthquake, and microseism observations were also found to be strongly correlated with one another. The results suggested that all three datasets are sensitive to the basin structure and could, therefore, be used together to improve the 3D velocity model.

We started to develop a simultaneous inversion of the observations from the three datasets to refine the velocity model within the SCV basins. To reduce the extremely large model space, we invert for the velocity structure within the basins while the basin geometry, as defined in the USGS ver. 2 velocity model, is held fixed. Basin geometry in the USGS model was mainly constrained by the inversion of the gravity data and is one of the better known parameters in the model.

We use the 3D elastic finite-difference code E3D to simulate the teleseismic, local, and microseism wavefields for the models with increasing levels of complexity in the basins. To model the plane wave from the teleseismic events, we used a disc of point sources in the deepest homogeneous layer of the model, representing the upper mantle. To simulate the microseisms, we used a localized source of isotropic Rayleigh waves located offshore.

In the next step, we use the simulated wavefields to do the inversion following the approach developed by *Aoi* [2002]. In his study, *Aoi* [2002] used the inversion scheme to estimate the 3D basin shape from the long-period strong ground motions. In this work we keep the basin geometry fixed and invert for the velocity structure within the basins.

## 21.2 Results

In the test inversions, we used the synthetic waveforms obtained with a selected target model instead of true observations. This was to test the inversion method while the target 3D velocity structure was known and based on the USGS ver. 2 model. We also used teleseismic data from a set of 38 stations. The structure within the basins was laterally uniform with a single velocity gradient. An example of the test inversion is presented below. The

velocities and density of the target and of the starting model are listed in Figure 3.44. The velocity and density gradients in the SCV basins in the target model were the same as in the USGS model. The velocity and density gradients in the starting model were 50% smaller than the USGS gradients in the SCV basins. The perturbation steps used for all six model parameters (P- and S-wave velocity and density at the surface and their gradients with depth) were 15% of their starting values.

The computations were performed on the BSL Linux cluster. Because of the computational limitations, the slowest velocities in the model were increased to a minimum S-wave velocity of 1 km/s. The slowest P-wave velocity was 1.75 km/s. The computation time for a single forward simulation was ~70 minutes when 16 cluster nodes and 2 processors per node were used. Each forward computation required ~4.5 GB of memory.

Results for a subset of four stations are presented in Figure 3.44. Stations 120 and 238 are located over the basins; station 186 is south of the Cupertino basin, and station PG2 is between the basins. Waveforms for the starting model and for a model from iteration steps 2 and 4 are shown (solid lines) as well as the waveforms obtained with a target model (dotted). Waveforms were bandpass filtered between 0.1 and 0.5 Hz as the waveforms from the recorded teleseisms had most of the energy in this frequency band. Only the first 20 s of the waveforms were used in the inversion. This time period includes the P-wave arrival as well as the P- to S-wave converted arrivals. The waveforms shown in Figure 3.44 include the arrival of the pP-wave that was also modeled, but not included in the inversion, as it arrives after the first 20 s. Results from the test inversions performed so far showed that the method is stable, and that four or less iteration steps were needed to reach the target model (*Dolenc*, 2006).

The presented inversion example used only teleseismic waveforms. Future inversions will use additional parameters obtained from the local earthquake and microseisms data. For the local earthquakes, these parameters will include energy estimates and peak ground velocity values. For the microseisms data, the parameter that will be included in the inversion will be the value of the horizontal to vertical spectral ratio peak. Additional parameters that would characterize the teleseismic waves coda could also be added.

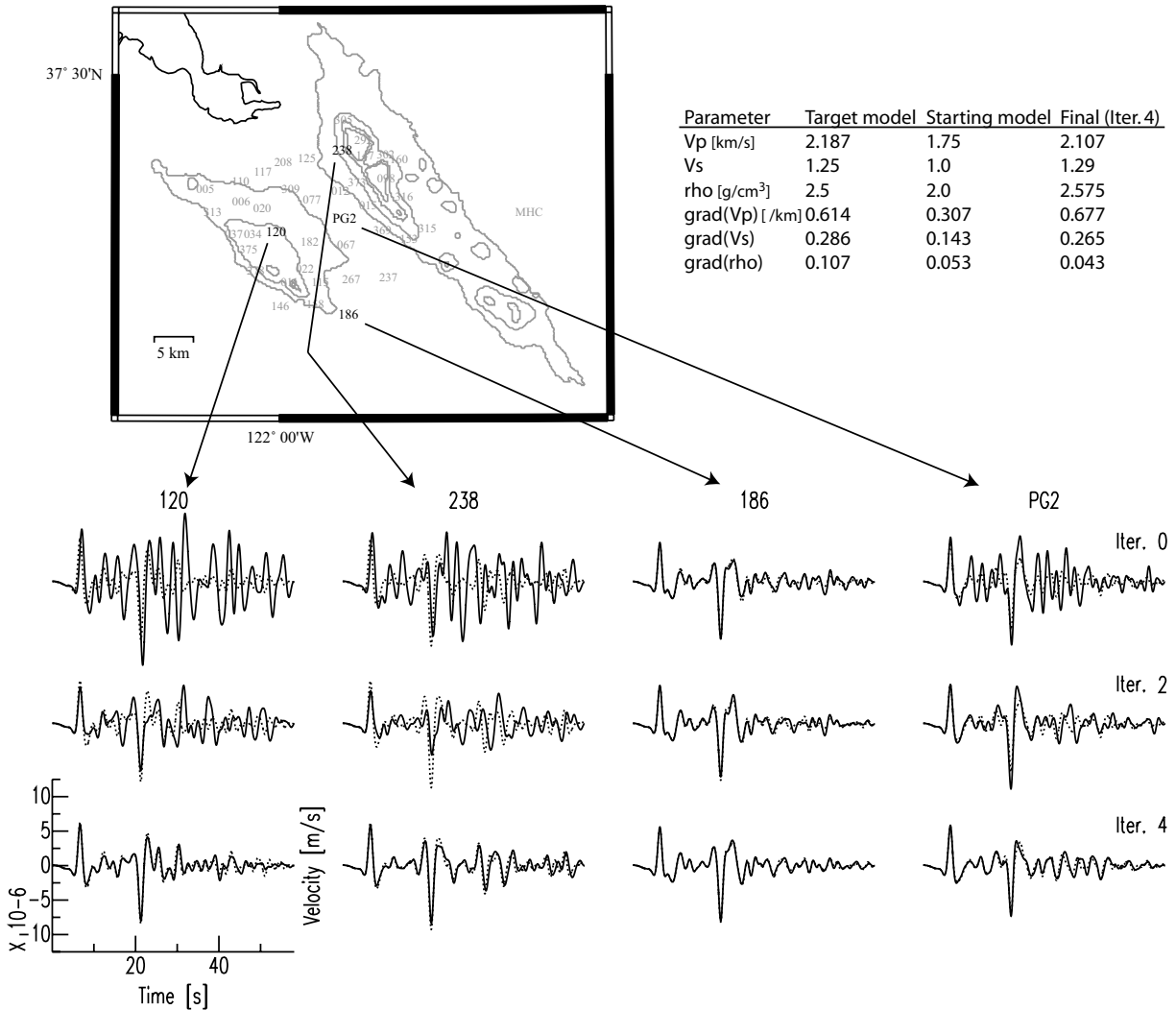


Figure 3.44: *Top left:* Closer look at the SCV region. Contours of the SCV basins from the USGS ver. 2 model at 1 km, 3 km, 5 km, and 6 km are shown in gray. *Top right:* The velocities and density in the SCV basins. *Bottom:* Results from a test inversion. Waveforms for the four SCV station are shown for the starting model (solid, top row) and for a model as it was modified after iteration 2 and 4 (solid, bottom rows). Waveforms obtained with the target model are shown for comparison (dotted).

### 21.3 Acknowledgements

Part of this work was supported by the USGS grants 99HQGR0057 and 00HQGR0048. The Hellman Faculty Fund is acknowledged for partial support.

### 21.4 References

Aoi, S., Boundary shape waveform inversion for estimating the depth of three-dimensional basin structures, *Bull. Seism. Soc. Am.*, 92, 2410-2418, 2002.

Dolenc, D., D. Dreger, and S. Larsen, Basin structure influences on the propagation of teleseismic waves in the Santa Clara Valley, California, *Bull. Seism. Soc. Am.*, 95, 1120-1136, 2005a.

Dolenc, D. and D. Dreger, Microseisms observations in the Santa Clara Valley, California, *Bull. Seism. Soc. Am.*, 95, 1137-1149, 2005.

Dolenc, D., Results From Two Studies in Seismology: I. Seismic Observations and Modeling in the Santa Clara Valley, California II. Observations and Removal of the Long-Period Noise at the Monterey Ocean Bottom Broadband Station (MOBB), *Ph.D. Thesis*, University of California, Berkeley, 2006.

Jachens, R. C., R. F. Sikora, E. E. Brabb, C. M. Wentworth, T. M. Brocher, M. S. Marlow, and C. W. Roberts, The basement interface: San Francisco Bay area, California, 3-D seismic velocity model, *EOS Trans. AGU.*, 78, F436, 1997.

## 22. A Study of the Relation between Ocean Storms and the Earth's Hum

Junkee Rhie and Barbara Romanowicz

### 22.1 Introduction

It had been shown that long period surface waves, especially Rayleigh wave type, are continuously and primarily radiating from the northern oceans during the northern hemisphere winter and from the southern oceans during the summer (Rhie and Romanowicz, 2004; Nishida and Fukao, 2004; Ekström and Ekström, 2005). In this study, we investigate a four day time window, which is free of large earthquakes but during which the long period seismic amplitude due to the "hum" is unusually high. By doing this, we infer that the "hum" events occur close to the shore rather than the deep ocean and the details of the generation mechanism. We also compare the variation in seismic amplitude at long period and short period bands for three years and show that there is a strong correlation during winter periods. It indicates that the "microseisms" and the "hum" events have a common generation mechanism.

### 22.2 Earthquake "free" interval 2000.031-034

The time interval between 2000.031 and 2000.034 is important to infer the "hum" mechanism because it is not contaminated by large earthquakes but shows the high level of long period seismic amplitudes. We considered stacks of vertical velocity seismograms recorded at very broadband STS-1 seismometers of two regional arrays in Japan (F-net) and California (BDSN). For each array, we stacked Gaussian filtered seismograms with various center periods according to the dispersion of Rayleigh waves, assuming plane wave propagation from an arbitrary azimuth. We apply a 6 hour running average with a time step of 1 hour to the stacked data at BDSN and F-net respectively. The results of a mean stack amplitude for center period of 150 and 240 s as a function of time and back-azimuth are shown in Figure 3.45. During given time interval, two noise events, probably due to the "hum" of the Earth, are clearly seen on 2000.031 and 2000.033 at both arrays. However, the arrival time of each event at each array is quite different. It is clear that BDSN records the event about 8-10 hours earlier than F-net does. 8-10 hour time difference is too large to be explained by seismic wave propagation, but it can be explained by the propagation speed of "free" infragravity waves at  $\sim 220$  m/s.

We also compare the seismic observation with a direct ocean buoy measurement near the coast of California and Japan. Unfortunately, many buoys near the Japanese

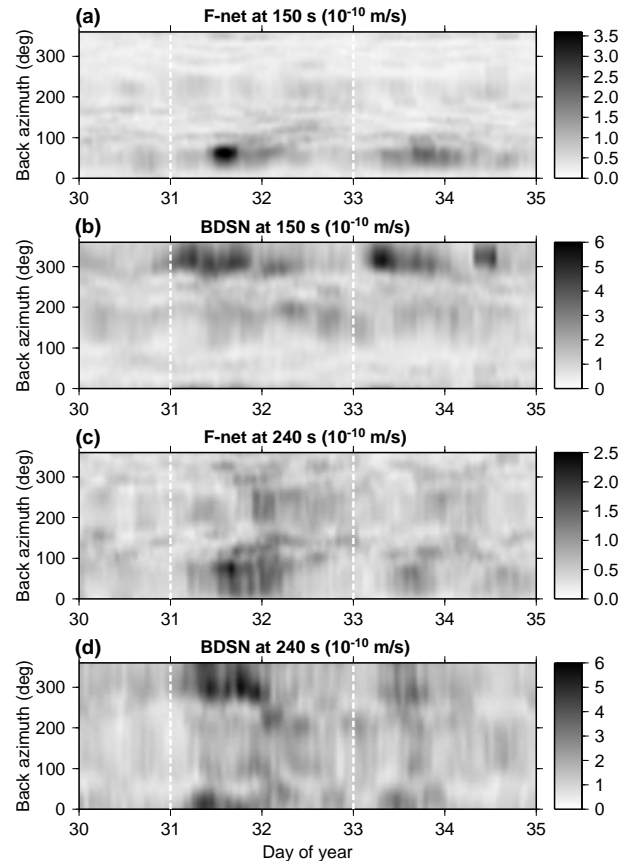


Figure 3.45: (a) Mean stack amplitude (MSA) with 6 hour time window lagged by 1 hour as a function of time and back azimuth for F-net. A Gaussian filter with center period of 150 s was applied before stacking. (b) Same as (a) for BDSN. (c) Same as (a) for center period of 240 s. (d) Same as (c) for BDSN.

eastern coast are not available. However, we can see very strong correlation between the variation in seismic amplitude and significant wave height recorded at buoys near the California coast.

### 22.3 Comparison with Microseisms

It is well known that non-linear interaction of ocean swells generates microseisms, especially double frequency microseisms, which is dominant seismic noise at short periods (2-25 s, Longuet-Higgins, 1950). We have shown that there is a strong correlation between the variation in

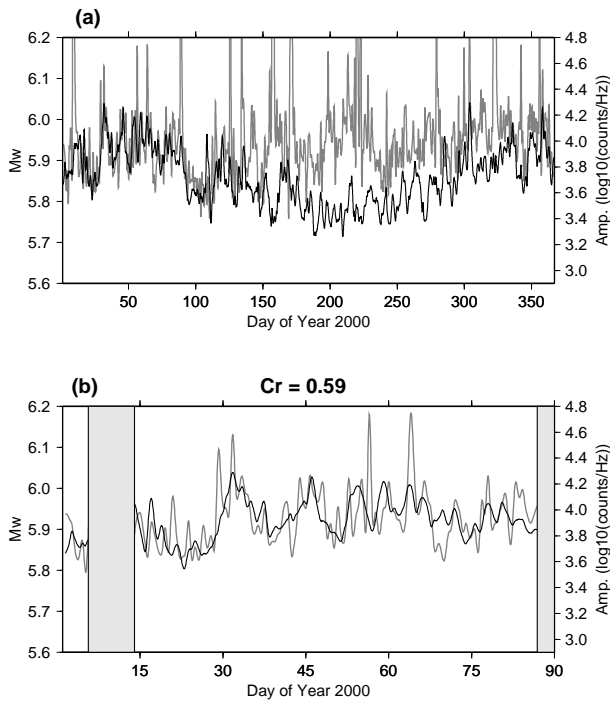


Figure 3.46: (a) A comparison between a processed long period (hum) amplitude (gray) and short period Fourier amplitude (black) for BDSN. (b) Detailed comparison of (a) during first 90 days of year 2000. Time window strongly contaminated by earthquakes are shaded in gray. Corresponding correlation coefficient is shown in the plot.

ocean wave height and long period seismic energy fluctuation. It indicates that both seismic noises at short (microseisms) and long (hum) periods are probably generated from common sources. Therefore, we compared amplitude levels in the two frequency bands for long time interval (e.g., a whole year). To do that, we need to reduce the contamination from the earthquakes. We developed a data processing method that avoids eliminating time windows contaminated by earthquakes (for details see *Rhie and Romanowicz, 2006*).

We compare the processed "hum" and microseism amplitude time series for BDSN over 3 years (e.g., Figure 3.46). The level of low frequency (hum) amplitude does not vary significantly with time (Figure 3.46a). However, there is a seasonal variation in the short period (microseism) amplitude, and it shows a strong correlation with significant wave height at buoys near California. During the winter period, short period amplitudes are maximum and the correlation between long and short period amplitude variations is high (Figure 3.46b).

## 22.4 Conclusions

By comparison between the variations in long period seismic amplitudes for two regional arrays in Japan and California, we observed that there is a time gap between arrivals of the common "hum" event on both sides of Pacific Ocean. This observation and direct comparison between seismic amplitude and significant wave height measurements at buoys lead us to a detailed scenario of generation of the "hum" comprising three steps: 1) short period ocean waves interact non-linearly to produce infragravity waves as the storm-related swell reaches the coast of North America; 2) infragravity waves interact with the seafloor locally to generate long period Rayleigh waves, which can be followed as they propagate to seismic stations located across North America; 3) some free infragravity wave energy radiates out into the open ocean, propagates across the north Pacific basin, and couples to the seafloor when it reaches distant coasts north-east of Japan, giving rise to the corresponding low frequency seismic excitation observed on the Japanese F-net array.

We have assembled and processed 3 years of microseism data at stations of the BDSN and F-NET arrays, and show a strong correlation of amplitude fluctuations in the microseismic band with that in the "hum" band during the northern hemispheric winter, but not during summer months, suggesting that in the winter, the microseisms and hum have a common "regional" or "local" origin, whereas in the summer, the origin of the hum is indeed distant (southern hemisphere) while the microseisms remain local and have smaller amplitudes

## 22.5 Acknowledgements

We wish to thank BDSN, F-net, JMA, and NOAA for providing high quality and continuous seismic and ocean buoy data.

## 22.6 References

- Ekström G., and S. Ekström, Correlation of Earth's long-period background seismic radiation with the height of ocean waves, *Eos Trans. AGU, 86*, Fall Meet. Suppl., Abstract S34B-02, 2005.
- Longuet-Higgins, M. S., A Theory of the origin of microseisms, *Philos. Trans. R. Soc. London, Ser. A, 243*, 1-35, 1950.
- Nishida, K., and Y. Fukao, Spatial variations of excitation amplitudes of Earth's background free oscillations, *Eos Trans. AGU, 84*, Fall Meet. Suppl., Abstract S31B-1068, 2004.
- Rhie, J., and B. Romanowicz, Excitation of Earth's continuous free oscillations by atmosphere-ocean-seafloor coupling, *Nature, 431*, 552-556, 2004.
- Rhie, J., and B. Romanowicz, A Study of the relation between ocean storms and the Earth's hum, *Geochem. Geophys. Geosyst.*, 2006 (in press).

## 23. Physically Constrained Inversion of Long-Period Seismic Data: Insights on the Nature of the Transition Zone

Fabio Cammarano and Barbara Romanowicz

### 23.1 Introduction

The thermal state and composition of the Earth's upper mantle and transition zone dictate its dynamics from microscale (e.g., creep mechanisms, earthquakes) to macroscale (e.g., modality of mantle convection, plate tectonics). The knowledge of these fundamental physical parameters and their three-dimensional variations in Earth's deep interior is indirect and relies entirely on the interpretation of geophysical data, based on insights from theoretical and experimental mineral physics. Among these, seismological observations constitute a main source of information. Seismic waves record information about the elastic (and anelastic) structure of the Earth. Long-period seismic data provide the most comprehensive global constraints on upper mantle shear velocity structure. Fundamental-mode surface waves are mostly sensitive to the uppermost mantle structure, while including overtones provide resolution in the transition zone.

Lateral temperature variations in the Earth have been inferred since the first tomography studies began to reconstruct 3-D seismic velocity structure (*Dziewonski et al.*, 1977, *Woodhouse and Dziewonski*, 1984). However, in spite of the ever-improving resolution of seismic velocity models and a general agreement of different models on at least the large-scale structure (e.g. *Ritsema*, 2004, *Su et al.*, 1994, *Li and Romanowicz*, 1995), interpretation is still challenging.

An important issue for seismic interpretation concerns the non-physical nature of any seismic model. Typically, the physical interpretation of a given seismic dataset is performed in two steps. First, a seismic model that fits satisfactorily the data is constructed. Second, the model is interpreted for the physical parameters based on the knowledge of the elastic and anelastic properties of mantle minerals plus constraints on plausible composition and temperature ranges from geochemistry - i.e. the signature of outcropping rocks (orogenic peridotites) and mantle inclusions (xenoliths and xenocrysts) -, heat flow measurements at surface and conditions for melting mantle materials. The second part of the process is commonly regarded as the critical one for the interpretation. Instead, it is often forgotten that the seismic models are already an interpretation of the data. The seismic models are non-unique and depend on the parametrization and distribution, quality and type of data used. More important, it is not ensured that a given best-fit seismic model corresponds to a physical model. For example,

the non-clear physical meaning of the seismic reference models (PREM *Dziewonski and Anderson*, 1981, AK135 *Kennett et al.*, 1995) has been elucidated by the previous work of one of us (*Cammarano et al.*, 2003). The same problems are transferred to 3-D tomography models that are obtained by perturbing the starting average model.

Here we invert long-period seismic waveforms, which are mainly sensitive to shear velocity, with respect to a physical reference model instead than common seismic reference models (e.g., PREM). Velocity variations will thus correspond to thermal (or compositional) variations and a consistent three-dimensional density and  $V_P$  structure may be determined. We start assuming purely thermal variations because in the upper mantle composition plays a secondary role. We compare the thermal features constrained by the seismic data against expected thermal variations and estimated geotherms in various tectonic regions. The average velocity model extracted from the physically constrained tomography provides insights on the nature of the transition zone. In order to assess the uncertainties in the thermal model and estimate how well average velocity and velocity gradient with depth in the upper mantle are constrained by long-period seismic data, we perform a series of inversions starting with various models.

### 23.2 Procedure

We test our inversion by using some of the PREF models from *Cammarano et al.* (2005a,b). These are pyrolytic, adiabatic models that fit global seismic data (i.e. travel times and fundamental modes). We select three PREF models that represent well the differences in seismic and mineral physics properties within the family of PREF models. The use of different starting PREF models, characterized by their own sensitivities of seismic velocities to temperature, will help to assess the effects of the mineral physics uncertainties on the physically-constrained inversion. At the same time, this will test how good is the assumption of non-dependence of the outcome from the starting model. To further investigate this point, we also invert the seismic data starting with a model that has a much smaller jump at 410km and different velocity gradients above and below this discontinuity (Figure 3).

The data used are long-period fundamental and higher-order mode surface waveforms from the existing Berkeley compilation. Events with moment magnitude larger than six and at teleseismic distance (epicentral distance

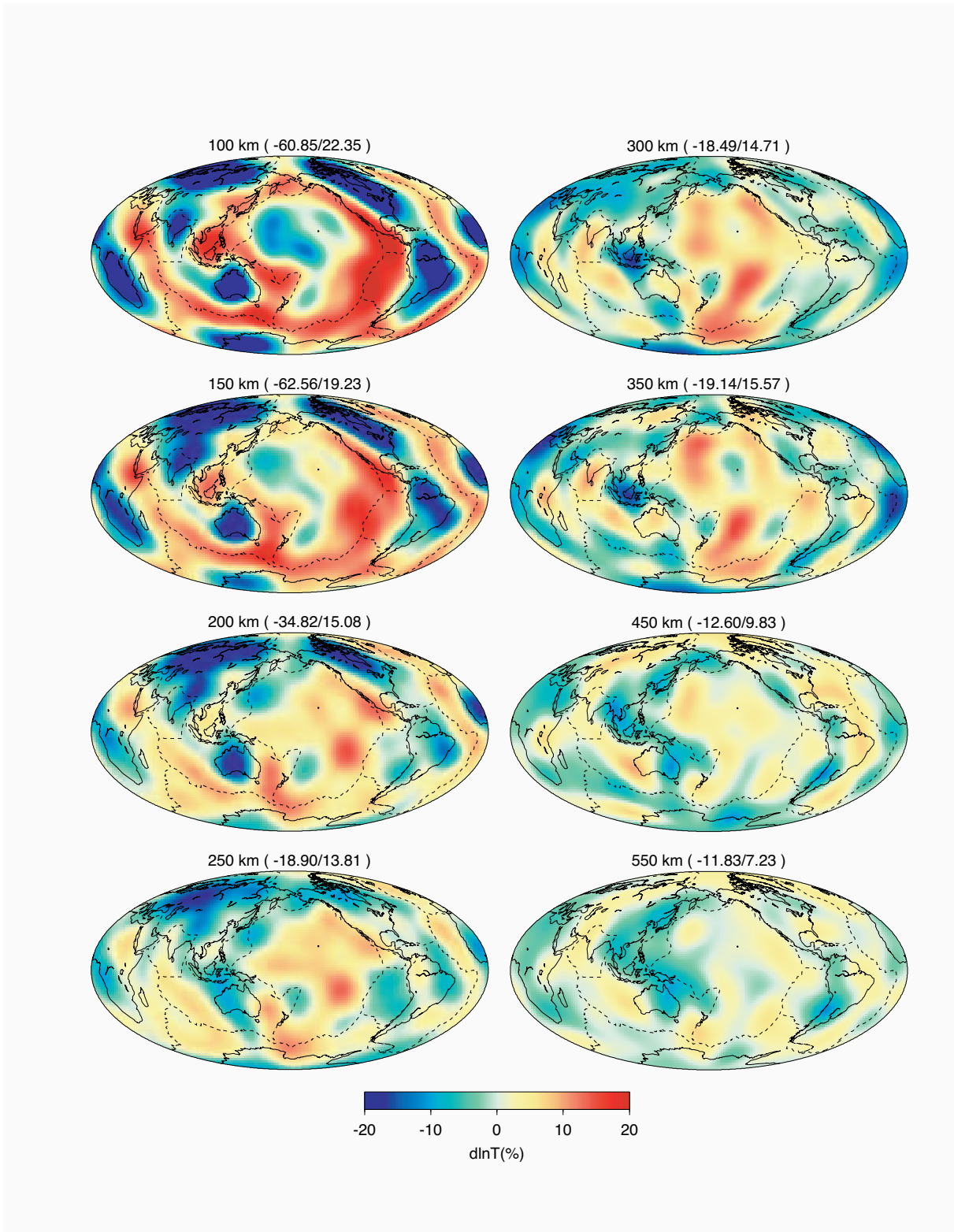


Figure 3.47: Lateral temperature variations inferred from the physically-constrained waveform inversion. In the uppermost mantle, positive anomalies correspond to oceanic ridges, negative to cratonic areas. Negative thermal anomalies related to subduction zones appear below. Minimum and maximum value of anomaly compared to the mean temperature value is given for each depth.

between  $15^\circ$  and  $165^\circ$ ) have been selected. The original seismograms have been deconvolved for the instrument response and filtered between 60 s and a variable maximum period, typically between 220 s and one hour, which is chosen according to the event magnitude. Wavepackets for both fundamental and overtones are extracted from the seismograms. The seismic waveform tomographic method is based on the Non-linear Asymptotic Coupling Theory method (NACT, *Li and Romanowicz, 1995*).

We start the inversion with a low-resolution version of a recent anisotropic model (SAW642AN, *Panning and Romanowicz, 2006*), but replacing the background seismic reference model with a physical reference model (i.e., PREF). We invert for the isotropic part down to 1000 km, while we keep fixed the radially anisotropic part of the model, represented by  $\xi$  ( $V_{SH}^2/V_{SV}^2$ ). Radial anisotropy is required to simultaneously fit spheroidal and toroidal fundamental modes. We correct for crustal structure assuming the model CRUST2.0 (*Bassin et al., 2000*). We solve iteratively the inversion procedure following, for each step, the classical least-squares approach.

### 23.3 The Thermal model

The lateral variations in temperature (Figure 3.47) confirm the primary role of temperature in determining the seismic structure of the upper mantle and transition zone. Thermal variations that explain the seismic data are indeed consistent with the range expected from dynamics modeling. However, the secondary compositional effect clearly emerges when looking at the “too-low” values of temperature obtained in the first 250 km beneath cratons. The lateral thermal variations between inversions with respect to different PREF models are very similar, indicating that the additional uncertainties in the temperature partial derivatives do not affect much the interpretation. Specifically, they affect it much less than regularization schemes required by the inversion process.

The upper-mantle geotherms constrained by long-period seismic data are able to reproduce the range of expected geotherms beneath oceans and cratons (Figure 3.48). We compare the seismic geotherms with geotherms for different oceanic age, based on the plate cooling model (*Turcotte and Schubert, 1982*), and continental geotherms, purely conductive, computed at steady-state and based on surface heat flow and radiogenic heat production in the crust (*Chapman, 1986*). Extremely low temperatures are found, sometimes, in cratons (Figure 3.48), that are likely to be related to the secondary compositional effect.

The capacity of inferring absolute temperatures and thermal gradients depends on how precisely we can determine absolute seismic velocity and gradients. To this end, we should point out that our results rely on assumed crustal and anisotropy structure.

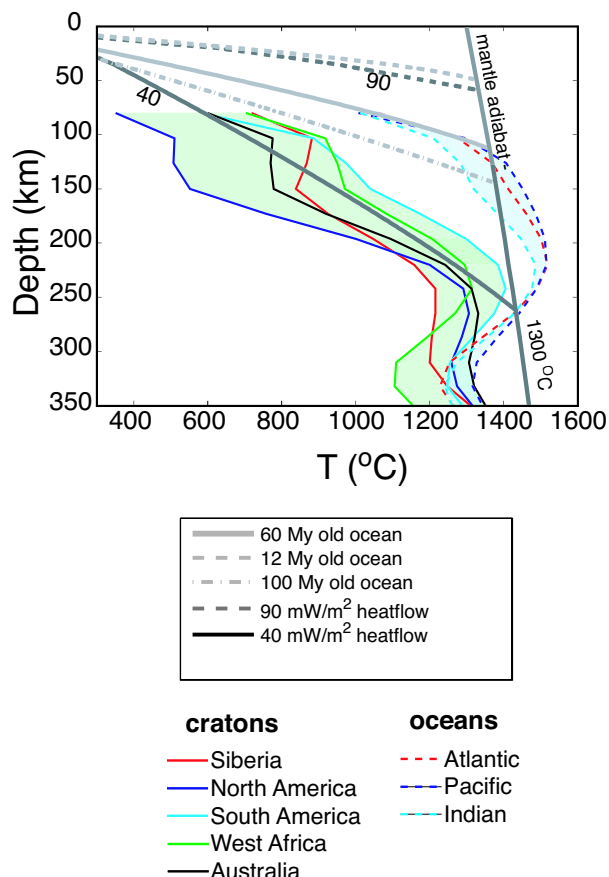


Figure 3.48: Seismic geotherms averaged over oceanic and cratonic regions.

### 23.4 The average model

In figure 3, we show the inverted average  $V_S$  structure obtained by the 3-D tomographic model. Absolute velocities and gradients are well constrained from long period data, except in proximity of the 410 km discontinuity (Figure 3.49). The velocity structure below 300 km is very similar in those different tectonic regions indicating the global character of the inverted average model in the transition zone.

The inverted model tends toward PREM, which is confirmed to be a very good average seismic model. The differences are due to the different starting parametrization. For example, because PREF does not have a 220 km discontinuity as PREM, the final model does not have this feature either. Instead, a higher velocity gradient than the starting model is required by the seismic data around this depth (Figure 3.49). Long-period seismic waveforms are not directly sensitive to the mantle discontinuities, and therefore, the gradients nearby a discontinuity are not well constrained by those data. This can be clearly seen when we compare the gradients nearby the 410 km discontinuity between the PREF inverted model and the

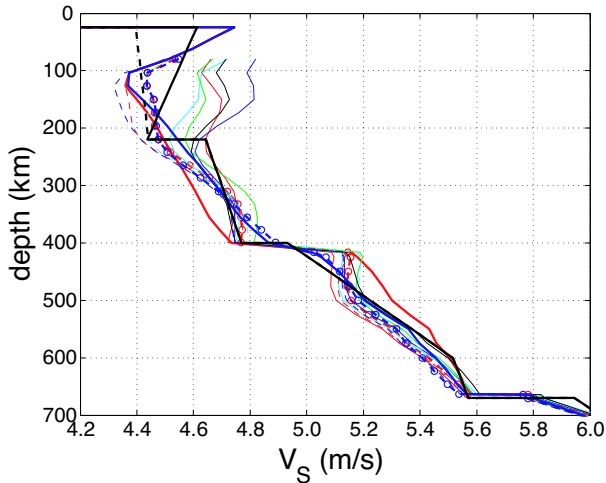


Figure 3.49: Inverted average structures for a PREF model (red) and a model with different gradient and smaller jump at 410km (blue). Solid lines are starting models, dots and dashed lines are inverted models. In background, velocity models beneath oceanic (thin dashed lines) and cratonic (thin solid lines) regions are shown.

model with the small jump at 410 km (see Figure 3.49).

### 23.5 The nature of the transition zone

The velocity jump imposed in the starting model at the olivine-wadsleyite transition dictates the gradients around it (Figure 3). Pyrolitic models, which have ~60 vol % of olivine, do have a larger jump than seismic reference models for this discontinuity ( $\Delta V_P$  6-10%,  $\Delta V_S$  6-12% (Cammarano *et al.*, 2005a) vs 2.5% and 3.5%, respectively, for PREM and 3.5% and 4% for AK135). If we assume in our starting model the large jump inferred from mineral physics, long period seismic waveforms require the changes in gradients above and below the 410 km discontinuity shown in Figure 3. A thermal interpretation of this structure is not feasible as we obtain temperatures ~1250 K at 350 km, ~1750 K around 500 km and geodynamically unrealistic thermal gradients throughout the upper mantle. We conclude that dry pyrolite can not be reconciled with seismic data. This conclusion has a global character as the similarity of the velocity profiles below 300 km beneath oceans and cratons show (Figure 3.49).

### 23.6 References

Bassin C., Laske G. and Masters G., The current limits of resolution for surface-wave tomography in North America, *EOS, Transactions Am. Geophys. Union* 81 F897, 2000

Cammarano F., Goes S., Deuss A. and Giardini D., Is a pyrolitic adiabatic mantle compatible with seismic data? *Earth Planet. Sci. Lett.* 232 227-243, 2005b

Cammarano F., Deuss A., Goes S. and Giardini D. (2005), One-dimensional physical reference models for the upper mantle and transition zone: combining seismic and mineral physics constraints, *J. Geophys. Res.* 110 B01306 doi:10.1029/2004JB003272, 2005a

Cammarano F., Goes S., Giardini D., Vacher P. (2003) *Phys. Earth Planet. Inter.* 138 197-222, 2003

Chapman D.S., Thermal gradients in the continental crust, in *The Nature of the Lower Continental Crust, Geol. Soc. Spec. Publ.*, vol. 24 63-70, 1986

Dziewonski A.M., and Anderson D.L., Preliminary Reference Earth Model, *Phys. Earth Planet. Inter.* 25 297-356, 1981

Dziewonski A.M., Hager B.H. and O'Connell R.J., Large-scale heterogeneities in the lower mantle, *J. Geophys. Res.* 82 239-255, 1977.

Kennett, B.L.N., E.R. Engdahl, and R.P. Buland, Constraints on seismic velocities in the Earth from travel times, *Geophys. J. Int.*, (122, 108-124, 1995.

Li, X.D. and Romanowicz B., Comparison of global waveform inversions with and without considering cross-branch modal coupling, *Geophys. J. Int.* 121 695-709, 1995

Turcotte D.L. and Schubert G. *Geodynamics. Cambridge University Press*, 1982

Ritsema J., van Heijst H.J., and Woodhouse J.H., Global transition zone tomography, *J. Geophys. Res.* 109 B02302, doi:10.1029/2003JB002610, 2004

Su W.J., Woodward R.L., and Dziewonski A.M., Degree 12 model of shear velocity in the mantle, *J. Geophys. Res.* 99 6945-6980, 1994

Woodhouse J.H. and Dziewonski A.M., Mapping the upper mantle: Three-dimensional modeling of the Earth structure by inversion of seismic waveforms, *J. Geophys. Res.* 89 9793-9823, 1994

## 24. The Fate of the Juan de Fuca Plate

Mei Xue and Richard M. Allen

### 24.1 Introduction

The Juan de Fuca plate is subducting beneath the northwestern United States and southwestern Canada. While the slab has been imaged to depths of  $\sim 300$  km beneath southern Washington and of at least 200 km beneath southern Oregon, there is little evidence for a slab deeper than  $\sim 100$  km east of High Cascades beneath central Oregon (Bostock, et al., 2002; Harris, et al., 1991; Iyer and Rite, 1981; Michaelson and Weaver, 1986; Rasmussen and Humphreys, 1988; Rondenay, et al., 2001). The apparent absence of the slab east of High Cascades can be interpreted as (1) a low high-velocity contrast making the slab indistinct from the surrounding mantle (Iyer and Stewart, 1977; Michaelson and Weaver, 1986); (2) a more vertical geometry of the slab (Michaelson and Weaver, 1986), or (3) a loss of seismic resolution. To image the slab beneath Oregon, we apply tomography technique using a dataset consisting of our own OATS deployment and all other available data.

### 24.2 Teleseismic tomography results

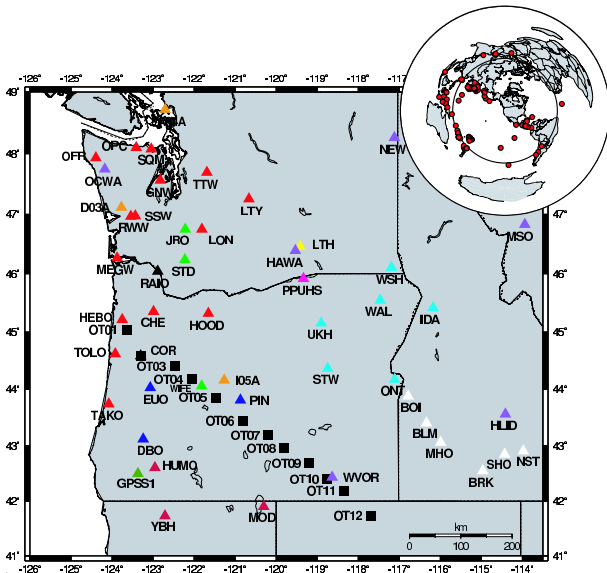


Figure 3.50: Seismic stations used in this study with a total number of 61. Inset shows the distribution of the 95 events used in the inversion for S-wave velocity model.

We have collected data from our own deployment of the Oregon Array for Teleseismic Study (OATS), an array extending northwest-southeast across Oregon from the coast to the McDermitt Caldera (Figure 3.50). We

have also collected data from permanent networks (BK, CC, US, UO, UW, PN, IU, TA, LI), and temporary deployments (XJ, YC, YS) (Figure 3.50). We inspect events with magnitude 6.0 and above from July 19th, 2003 to Nov. 11th, 2004 for a total of 61 stations and follow the same inversion procedure as in (Allen, et al., 2002). For the Vs inversion, a total of 95 events (Figure 3.50) with clear S and SKS phases were recorded at 45 stations, and a total number of 2148 rays were used. For the Vp inversion, a total of 74 events with clear direct P phase were recorded at 46 stations, and a total number of 2043 rays were used.

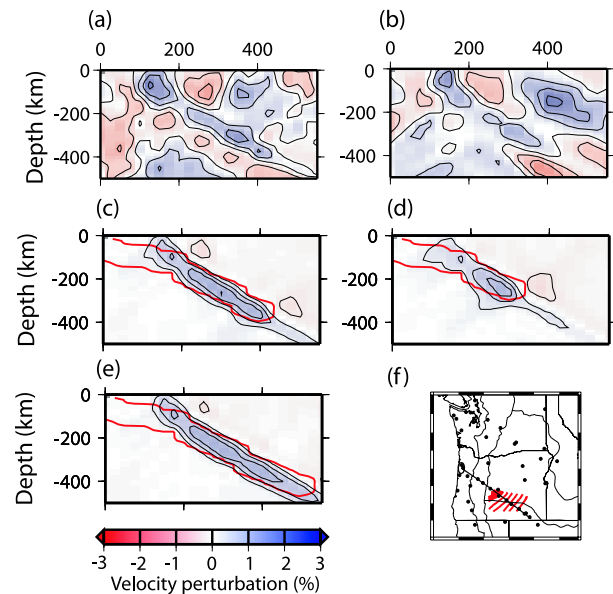


Figure 3.51: Tomographic results showing S- and P- wave velocity structures beneath Oregon and results of inverting synthetic data created from various test slabs. All vertical slices show the same cross section as in (f), along the OATS line, where we have high resolution: (a) the Vs model; (b) the Vp model; resolution tests of S-wave velocity inversion for a slab ending at (c) 400 km depth, (d) 300 km depth, and (e) 500 km depth, and the input anomaly is 3% and dips  $50^\circ$ , outlined by red lines; (f) a map shows the location of the cross-section.

Our tomography results show that the subducted slab extends to a depth of  $\sim 400$  km with a dip of  $\sim 44^\circ$  (Figure 3.51, a and b). After correcting the oblique trend of the cross section, the real dip angle is  $\sim 50^\circ$ . Resolution tests show that structures at shallower depths are better recovered in terms of amplitudes and smearing is less significant. Here, we show three resolution tests for

S-wave velocity models (Figure 3.51, c, d, and e). To test whether the structure we observed between 300 km and 400 km depth is caused by smearing shallow structure or not, we used a synthetic velocity anomaly with a high velocity to 300 km depth only. Figure 2d shows that a slab ending at 300 km depth is not sufficient to produce the observed slab structure between 300 km and 400 km depth. Figure 2c shows a case that the recovered structure resembles what we observed best, where the input slab extends to 400 km and stops there. To test whether the slab stops at 400 km, we conducted the test as shown in Figure 2e where the input slab extends to 500 km depth. Considering the depth range between 400 km to 500 km, the recovered structure differs from the observed structure in three aspects: (1) it has a much stronger velocity anomaly, (2) the transition of velocity anomaly from higher amplitudes to lower amplitudes is smooth, and (3) it didn't lose its width (Figure 3.51e). Thus we speculate that the slab likely stops at  $\sim 400$  km depth and does not extend deeper. The P-wave velocity model also suggests that the slab stops at  $\sim 400$  km (Figure 3.51b). This interpretation can be better tested when USArray data becomes available further east.

### 24.3 Conclusion

Our tomographic images clearly show the Juan de Fuca plate diving into the mantle beneath Oregon and continues east of the High Cascades with a dip of  $\sim 50^\circ$  reaching a depth of  $\sim 400$  km. The slab dips shallower compared with its counterparts to north and south, which have a dip of  $\sim 65^\circ$  (Harris, et al., 1991; Rasmussen and Humphreys, 1988). Resolution tests suggest there is little or no velocity anomaly associated with a slab below  $\sim 400$  km.

### 24.4 Acknowledgements

This work was supported by the NSF (EAR-0539987). We thank Gene Humphreys for allowing us using data from their deployment at Wallowa Mountain. The IRIS DMC provided seismic data. The figures were produced with SAC and GMT (Wessel and Smith, 1995).

### 24.5 References

Allen, R. M., et al., Imaging the mantle beneath Iceland using integrated seismological techniques, in *Journal of Geophysical Research-Solid Earth*, 107, 2325, doi:2310.1029/2001JB000595, 2002.

Bostock, M. G., et al., An inverted continental Moho and serpentinization of the forearc mantle, in *Nature*, 417, 536-538, 2002.

Harris, R. A., et al., Imaging the Juan Defuca Plate beneath Southern Oregon Using Teleseismic P-Wave Residuals, in *Journal of Geophysical Research-Solid Earth*, 96, 19879-19889, 1991.

Iyer, H. M., and A. Rite, Teleseismic P-wave delays in Oregon Cascades, in *EOS, Trans. Am. geophys. Un.*, 62, 1981.

Iyer, H. M., and R. M. Stewart, Teleseismic technique to locate magma in the crust and upper mantle, in Magma Genesis, in *Proceedings of the AGU Chapman Conference on Partial Melting in the Upper Mantle*, edited by H. J. B. Dick, pp. 281-299, Oreg. Dep. Geol. Min. Ind. Bull, 1977.

Michaelson, C. A., and C. S. Weaver, Upper Mantle Structure from Teleseismic P-Wave Arrivals in Washington and Northern Oregon, in *Journal of Geophysical Research-Solid Earth and Planets*, 91, 2077-2094, 1986.

Rasmussen, J., and E. Humphreys, Tomographic Image of the Juan-Defuca-Plate beneath Washington and Western Oregon Using Teleseismic P-Wave Travel-Times, in *Geophysical Research Letters*, 15, 1417-1420, 1988.

Rondenay, S., et al., Multiparameter two-dimensional inversion of scattered teleseismic body waves 3. Application to the Cascadia 1993 data set, in *Journal of Geophysical Research-Solid Earth*, 106, 30795-30807, 2001.

Wessel, P., and W. H. F. Smith, New version of the Generic Mapping Tools released, EOS, in *Trans. Am. geophys. Un.*, 76, 329, 1995.

# 25. Applying the Spectral Element Method to Model 3D Attenuation in the Upper Mantle

Vedran Lekic, Barbara Romanowicz and Yann Capdeville (IPGP)

## 25.1 Introduction

Observations of surface waves and overtones provide a unique opportunity for probing the physical state and dynamics of the upper mantle, due to their global coverage and sensitivity to structure at depths approaching 1000 km. Earth structure affects seismic waveforms through elastic effects of (de)focusing and scattering, as well as anelastic effects that result in amplitude decay and velocity dispersion. Because anelastic processes appear to be thermally activated, temperature has a stronger effect on seismic attenuation than does chemical heterogeneity. This is not the case with seismic velocity, which can strongly depend on both chemical composition and temperature. These differences - combined with a three-dimensional model of both seismic velocity and attenuation - translate into a unique opportunity to separate the effects of temperature variation from those of compositional heterogeneity within the mantle.

## 25.2 Past Work and Challenges

Normal mode summation methods coupled with approximate first-order perturbation techniques have been successfully applied to modeling of surface waves. Recent high-resolution global tomographic models based on these techniques can resolve regions of fast and slow seismic velocities as small as a few hundred kilometers across (e.g. *Mégnin and Romanowicz, 2000*). Yet, modeling of the 3D distribution of seismic attenuation has lagged behind due to difficulties in separating the effects on seismic waveforms of focusing and scattering of seismic energy in the heterogeneous earth from those due to attenuation intrinsic to the medium. Even when the elastic structure is known perfectly, first-order perturbation techniques are inadequate in modeling wave propagation near the source or receiver, near nodes of the radiation pattern, in locations of strong heterogeneity, and at times long after the source time. Spectral element methods, on the other hand, allow accurate modeling of seismic wave propagation, including the effects of (de)focusing of energy and multiple scattering.

Extracting structural information from seismic waveforms requires calculating the sensitivity kernels of the waveform to parameters like elastic wave velocity and attenuation at each point in the earth. The conventional way of computing sensitivity kernels, called the path average approximation (PAVA), assumes that the wave is only sensitive to structure along the great circle path joining the source with the receiver, and that this sensitivity

is only a function of depth. Higher-order asymptotic approaches, such as non-linear asymptotic coupling theory (NACT: *Li and Romanowicz, 1995*), are capable of more accurately modeling the wave's actual sensitivity within the plane defined by the great circle path. Yet, long period surface waves observed at teleseismic distances are sensitive to structure both along and off the great circle path. While the (de)focusing effects that arise from velocity gradients transverse to the great circle path can be incorporated into the NACT formalism (NACT+F: *Gung and Romanowicz, 2004*), it is also now within reach to use more exact formalisms - such as the full Born approximation - in order to more accurately calculate sensitivity kernels.

## 25.3 Method

We propose a hybrid approach to tomography, in which we calculate the propagation of seismic waves through an arbitrary 3D medium exactly, using the coupled Spectral Element Method (cSEM: *Capdeville et al., 2003*), and compute the sensitivity kernels approximately, using perturbation theory. This approach allows us to iteratively converge on the correct model as long as the sign of the sensitivity kernels is correct. We apply this approach to 3-component fundamental and overtone waveforms, low-passed at 60 sec, and recorded at more than 100 stations of the IRIS/GSN, GEOSCOPE, GEOFON, and various regional broadband networks. Because of the increased computational costs associated with using cSEM, we at first restrict our focus to  $\sim 70$  events. We ensure excellent global coverage by including major arc surface waves, which provide complimentary sensitivity to minor arc paths. Furthermore, we select deep focus events in all regions where deep seismicity is present. Figure 3.52 shows the events used in our study, color-coded by centroid depth. Resolution tests indicate that our data coverage is sufficient for resolving structures  $\sim 900$  km at the surface, and that vertical smearing is limited.

## 25.4 Preliminary Results and Future Work

We have modified cSEM to include the effects of ellipticity, topography/bathymetry, radial anisotropy, 3D attenuation, and lateral variations in crustal velocities and depth to the Moho discontinuity. Because their sensitivities are concentrated near the surface, fundamental mode waves are especially strongly affected by 3D Moho topography; in contrast, crustal velocities play a

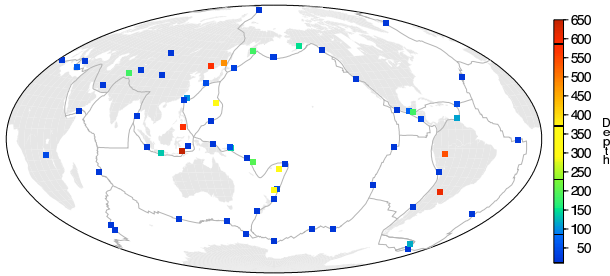


Figure 3.52: Events used in our study color coded by centroid depth.

secondary role. For long continental paths, waveforms corrected for crustal structure display phase delays of 100 sec. Interestingly, first order perturbation theory underpredicts by as much as 50 percent the cSEM phase delays over continents. Along oceanic paths, the differences between cSEM and first order perturbation theory are negligible. Figure 3.53 shows synthetic waveforms calculated by cSEM and NACT for typical long continental and oceanic paths.

We adopt an iterative waveform inversion approach, in which we solve for elastic and anelastic structure in successive steps. As a starting model, we adopt a high-resolution 3D elastic model of Panning and Romanowicz (2006), and a one-dimensional attenuation model constructed from separate upper mantle (QL6: *Durek and Ekstrom, 1996*) and lower mantle (PREM: *Dziewonski and Anderson, 1981*) models. Following our first iteration for elastic structure, which is performed in order to render compatible the starting model with our new dataset, we shall proceed to invert for source parameters. Because rotations of the radiation pattern can result in large amplitude changes - especially near the radiation nodes - inverting for the source mechanism is crucial to developing high resolution models of mantle attenuation.

## 25.5 Conclusion

We have compiled a waveform dataset of fundamental mode surface waves and overtones with good global lateral and depth coverage. We have modified cSEM to make it capable of accurately modeling wave propagation in an elliptic earth with surface topography / bathymetry, oceans, and 3D crustal structure. We find that first order perturbation theory inadequately predicts the effects of crustal structure on waveforms for long continental paths. Because of the magnitude of this deficiency, we expect our use of cSEM to allow us to model more accurately mantle structure below continents. Furthermore, the use of cSEM will allow us to better model amplitudes of seismic waveforms, and therefore to separate the often elusive signal of attenuation from that due to elastic structure.

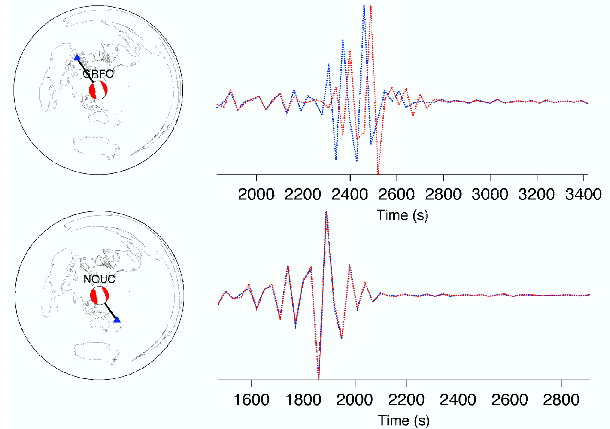


Figure 3.53: Synthetic seismograms from mode summation (blue) and cSEM (red) for a long continental (top) and oceanic (bottom) path.

## 25.6 Acknowledgements

Support for V. Lekic was provided by the Berkeley Fellowship.

## 25.7 References

- Capdeville, Y., E. Chaljub, J.P. Vilotte and J.P. Montagner, Coupling the spectral element method with a modal solution for elastic wave propagation in global Earth models. *Geophys. J. Int.*, 152, 34-66, 2003.
- Durek, J.J. and G. Ekström, A radial model of anelasticity consistent with long-period surface-wave attenuation. *BSSA*, 86, 144-158, 1996.
- Dziewonski, A.M. and D.L. Anderson, Preliminary reference Earth model. *Phys. Earth and Planetary Int.*, 25, 297-356, 1981.
- Gung, Y. and B. Romanowicz., Q tomography of the upper mantle using three-component long-period waveforms. *Geophys. J. Int.*, 157, 813-830, 2004.
- Li, X.D. and B. Romanowicz, Comparison of global waveform inversions with and without considering cross-branch modal coupling, *Geophys. J. Int.*, 121, 695-709, 1995.
- Megnin, C. and B. Romanowicz, The three-dimensional shear velocity structure of the mantle from the inversion of body, surface and higher-mode waveforms. *Geophys. J. Int.*, 143, 709-728, 2000.
- Panning, M. and B. Romanowicz, A three-dimensional radially anisotropic model of shear velocity in the mantle. *Geophys. J. Int.*, in press, 2006.



# 26. Radial and Azimuthal Anisotropic Structure of the North American Upper Mantle From Inversion of Surface Waveform Data

Federica Marone and Barbara Romanowicz

## 26.1 Introduction

Seismic anisotropy is required for a correct interpretation of the retrieved  $S$ -velocity structure in tomographic studies at least in the first 400 km of the upper mantle (Gung *et al.*, 2003). A detailed knowledge of the seismic anisotropic structure of the earth’s mantle also provides insight into paleo and recent deformation processes and therefore mantle dynamics. As a consequence, seismic anisotropy is a very powerful “tool” with the potential to shed light onto debated geophysical issues, such as the nature and strength of the lithosphere/asthenosphere coupling, the depth extent of continental sub-regions and the relation of imaged seismic anisotropy to present-day asthenospheric flow and/or past tectonic events recorded in the lithosphere.

To date, our knowledge of the North American upper mantle anisotropic structure arises mainly from global tomographic models (e.g. Ritsema *et al.*, 1999; Gung *et al.*, 2003) or  $SKS$  splitting studies (e.g. Fouch *et al.*, 2000; Savage and Sheehan, 2000), which lack horizontal and vertical resolution respectively, and are limited to either radial or azimuthal anisotropy. It is most probably due to these limitations that to date continental anisotropic models derived from surface and body wave data are not in agreement and cannot be reconciled.

Our goal is a new high resolution model for the North American upper mantle incorporating both radial and azimuthal anisotropy. We aim at unprecedented lateral and depth resolution by improving both data coverage and methodology.

## 26.2 Dataset

We consider fundamental and overtone surface waveforms selected from 3 component long period seismograms. Surface wave data for paths relevant to the study region have been extracted from the existing compilation used for global tomography in Panning and Romanowicz (2006). This dataset has been further complemented with waveforms from events at teleseismic and far regional distances ( $15^\circ < \Delta < 165^\circ$ ) recorded at permanent and temporary broad band seismic stations in North America. The collected dataset includes data for 657 events from 1990 to 2003, with  $M_w$  between 6.0 and 7.0. Each seismogram is filtered (between 60 s and 220 s to 1 hour, according to the event magnitude) and divided into wavepackets containing individual fundamental and higher mode first orbit energy packets. Each wavepacket is weighted so as to equalize the contribution of large and

small amplitude packets in the least-squares inversion. Our final dataset consists of more than 18,000 fundamental mode and 27,000 higher modes high quality surface wave packets, which provides a fairly homogeneous path and azimuthal coverage for North America.

In addition, we compiled station average  $SKS$  splitting measurements (delay times  $dt$  and fast axis directions  $\phi$  and their uncertainties) from published studies for about 300 North American stations.

## 26.3 Methodology

We apply a full waveform tomographic method based on the Non-linear Asymptotic Coupling Theory (NACT - Li and Romanowicz (1995)), which permits the inversion of entire long period seismograms in the time domain (including fundamental mode and overtones portions of the record) for 3D elastic structure. NACT is a normal-mode perturbation approach, which takes into account coupling between modes both along and across dispersion branches. The asymptotic calculation of this coupling allows the computation to 2D broad band sensitivity kernels which more rigorously reproduce the sensitivity of body waveforms to structure along and around the ray geometrical path in the vertical plane containing the source and the receiver.

To ensure high quality of the retrieved regional upper mantle structure, accurate crustal corrections are essential. Here, we follow an approach which goes beyond the linear perturbation approximation and split the correction into a linear and non-linear part (Montagner and Jobert, 1988).

We followed an iterative inversion approach. In a first step, we inverted waveform data simultaneously for perturbations in the isotropic  $S$ -velocity structure and the anisotropic parameter  $\xi = v_{SH}^2/v_{SV}^2$ . While keeping this obtained radial anisotropic model fixed, in a second step we inverted the waveform dataset jointly with the compiled  $SKS$  splitting measurements for two additional parameters related to the dominant  $2\Psi$  azimuthal dependence of the propagation velocity of surface waves (Montagner *et al.*, 2000; Marone and Romanowicz, 1996a).

## 26.4 Results

Our 3D radial anisotropic model (Marone *et al.*, 2006b) shares the large scale features of previous regional studies for North America (e.g. Van der Lee and Nolet, 1997; Grand, 2001). We confirm the pronounced difference in the isotropic velocity structure (Figure 3.54a) between

the western active tectonic region and the central/eastern stable shield, as well as the presence of subducted material (Juan de Fuca and Farallon plate) at transition zone depths. Concerning the radial anisotropic signature (Figure 3.54b), we observe a positive  $\xi$  anomaly in correspondence of the cratonic areas down to 300 km depth, while a negative  $\xi$  anomaly beneath the Appalachians mapped at 250 km depth, where a low velocity feature is also present, supports the hypothesis of mantle upwelling induced by water released during subduction of the Iapetus ocean or related to the subducted Farallon plate (Van der Lee *et al.*, 2005).

Our 3D azimuthal anisotropic model (Figure 3.54c) indicates the presence of two layers of anisotropy with distinct fast axis directions under the stable part of the North American continent: a deeper layer with the fast axis direction aligned with the absolute plate motion direction suggesting lattice preferred orientation of anisotropic minerals in a present day asthenospheric flow and a shallower lithospheric layer likely showing records of past tectonic events. Under the tectonically active western US, where the lithosphere is thin, the direction of tomographically inferred anisotropy is stable with depth and compatible with both absolute plate motion direction and the dominant direction obtained from *SKS* splitting measurements. The combined radial and azimuthal anisotropic 3D structure retrieved in our model, resolved throughout the upper mantle, represents the advancement of this study with respect to previous works. These new results seem to suggest a possible reconciliation between anisotropic models derived from surface and body wave data.

## 26.5 Acknowledgements

This research was partially supported through a grant from the Stefano Frascini Foundation (Switzerland) and NSF-EAR (Earthscope) grant #0345481. The digital seismograms used in our work have been distributed by the IRIS-DMC, the Geological Survey of Canada and the Northern California Earthquake Data Center (data contributed by the Berkeley Seismological Laboratory, University of California, Berkeley).

## 26.6 References

Fouch, M.J., K.M. Fischer, E.M. Parmentier, M.E. Wysession and T.J. Clarke, Shear-wave splitting, continental keels, and patterns of mantle flow, *J. Geophys. Res.*, 105, 6255-6275, 2000.

Grand, S.P., Mantle shear structure beneath the Americas and surrounding oceans, *J. Geophys. Res.*, 99, 591-621, 1994.

Gung, Y., M. Panning and B. Romanowicz, Global anisotropy and the thickness of continents, *Nature*, 422, 707-711, 2003.

Li, X.D. and B. Romanowicz, Comparison of global waveform inversions with and without considering cross-branch modal coupling, *Geophys. J. Int.*, 121, 695-709, 1995.

Marone, F. and B. Romanowicz, Non-linear crustal corrections in high resolution regional waveform seismic tomography, *Geophys. J. Int.*, in revision, 2006a.

Marone, F., Y. Gung and B. Romanowicz, 3D radial anisotropic structure of the North American upper mantle from inversion of surface waveform data, *Geophys. J. Int.*, submitted, 2006b.

Montagner, J.-P. and N. Jobert, Vectorial tomography; II. Application to the Indian Ocean, *Geophys. J.*, 94, 309-344, 1988.

Montagner, J.-P., D.-A. Griot-Pommeroy and J. Lavé, How to relate body wave and surface wave anisotropy?, *J. Geophys. Res.*, 105(B5), 19015-19027, 2000.

Panning, M. and B. Romanowicz, A three dimensional radially anisotropic model of shear velocity in the whole mantle, *Geophys. J. Int.*, in press, 2006.

Ritsema, J., H. van Heijst and J. Woodhouse, Complex shear wave velocity structure imaged beneath Africa and Iceland, *Science*, 286, 1925-1928, 1999.

Savage, M.K. and A.F. Sheehan, Seismic anisotropy and mantle flow from the Great Basin to the Great Plains, western United States, *J. Geophys. Res.*, 105, 13715-13734, 2000.

Van der Lee, S. and G. Nolet, Upper mantle *S*-velocity structure of North America, *J. Geophys. Res.*, 102, 22815-22838, 1997.

Van der Lee, S., K. Regenauer-Lieb and D. Yuen, The role of water in connecting past and future episodes of subduction, *Eos Trans., AGU*, 86(52), Fall Meet. Suppl., 2005.

## 27. Improvements in Waveform Modeling and Application to Eurasian Velocity Structure

Mark Panning (now at Princeton), Federica Marone, Ahyi Kim, Yann Capdeville (IPG Paris), Paul Cupillard (IPG Paris), Yuancheng Gung (National Taiwan University), and Barbara Romanowicz

### 27.1 Introduction

We introduce several recent improvements to mode-based 3D and asymptotic waveform modeling and examine how to integrate them with numerical approaches for an improved model of upper-mantle structure under eastern Eurasia. There is considerable information on structure in broadband seismograms that is currently not fully utilized. With numerical techniques, such as the Spectral Element Method (SEM), it should be possible to compute the complete predicted wavefield accurately without any restrictions on the strength or spatial extent of heterogeneity. This approach, however, requires considerable computational power.

We have implemented an approach which relies on a cascade of increasingly accurate theoretical approximations for the computation of the seismic wavefield to develop a model of regional structure for the area of Eurasia located between longitudes of 30 and 150 degrees E, and latitudes of -10 to 60 degrees North. The selected area is very heterogeneous, but is well surrounded by earthquakes and a significant number of high quality broadband digital stations, making it an ideal area to test new methods.

### 27.2 Starting Model

The first step in our modeling approach is to create a large-scale starting model including shear anisotropy using Nonlinear Asymptotic Coupling Theory (NACT; *Li and Romanowicz, 1995*), which models the 2D sensitivity of the waveform to the great-circle path between source and receiver, but neglects the influence of off-path structure. We have recently improved this approach by implementing a new crustal correction scheme, which includes a non-linear correction for the difference between the average structure of several large regions from the global model with further linear corrections to account for the local structure at each point along the path between source and receiver (*Marone and Romanowicz, 2006; Panning and Romanowicz, 2006*).

We inverted a global dataset augmented by additional data collection for paths which cross the region. To use the global dataset, we correct for structure outside the region using a global anisotropic starting model, SAW642AN (*Panning and Romanowicz, 2006*). The model in the region includes isotropic S structure parameterized in level 6 spherical splines, which correspond to a lateral resolution of  $\sim 200$  km (figure 3.55).

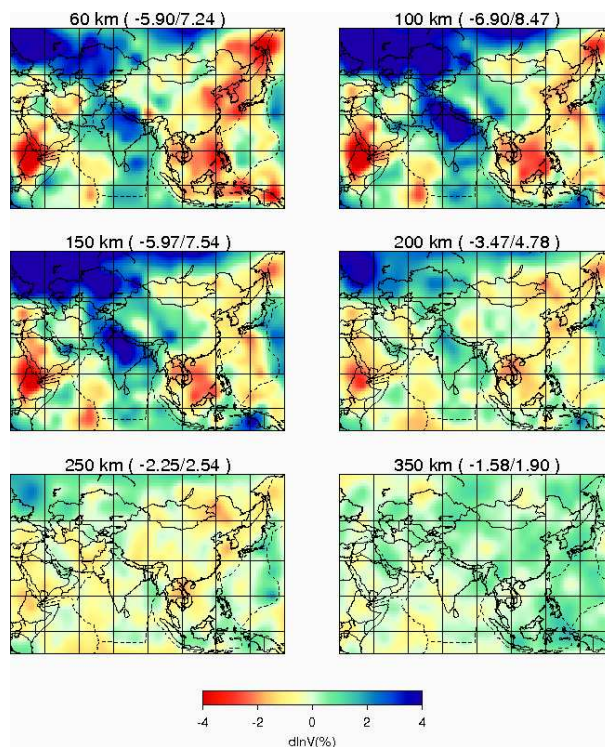


Figure 3.55: Starting isotropic S velocity model for the upper mantle for Eurasia developed using NACT. Values are the percent perturbations in isotropic velocity from PREM. Model is parameterized in radial splines spaced approximately 100 km, and in level 6 spherical splines (spacing  $\sim 200$  km).

It also includes anisotropy through the parameter  $\xi = (V_{SH})^2 / (V_{SV})^2$ . This is parameterized with a lateral resolution of  $\sim 400$  km (not shown here).

### 27.3 3D Born approximation

This model is further refined using a 3D implementation of Born scattering (*Capdeville, 2005*). We have made several recent improvements to this method, such as including perturbations to discontinuities. While the approach treats all sensitivity as linear perturbations to the waveform, we have also experimented with a non-linear modification to the approach analogous to that used in development of NACT. This modification allows us to treat large accumulated phase delays determined from a path-average approximation non-linearly, while

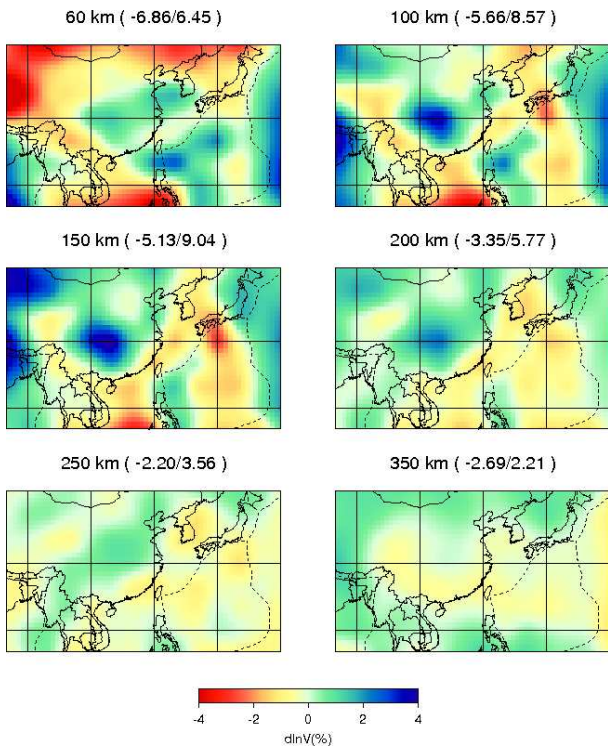


Figure 3.56: Shear velocity model developed using linear Born kernels for 180 events recorded on the vertical component. Values shown are perturbations relative to the isotropic average of the reference model.

still using the full 3D sensitivity of the Born scattering approximation.

We have performed some preliminary modeling of a subregion between longitudes 90 and 145 degrees E, and latitudes 15 and 40 degrees N with a subset of the original dataset consisting of the vertical component data from source-receiver pairs contained within the large region. The preliminary model is a relatively low resolution ( $\sim 400$  km) isotropic velocity model. We show the model derived using the Born approximation with (figure 3.56) and without the non-linear correction (figure 3.57). In these preliminary models, it is difficult to determine which model is better able to image the anomalies.

## 27.4 Numerical approaches

In preparation for the next step in the modeling, we have adapted to the regional case the Spectral Element Method (SEM) code (e.g. *Komatitsch and Vilotte, 1998*). The regionalization is performed by limiting the lateral and radial extent of the volume of interest through the implementation of Perfectly Matched Layers (PML) which effectively eliminate spurious reflections from the boundaries. This code now works for 3D regional models, and will be integrated into the forward modeling of our

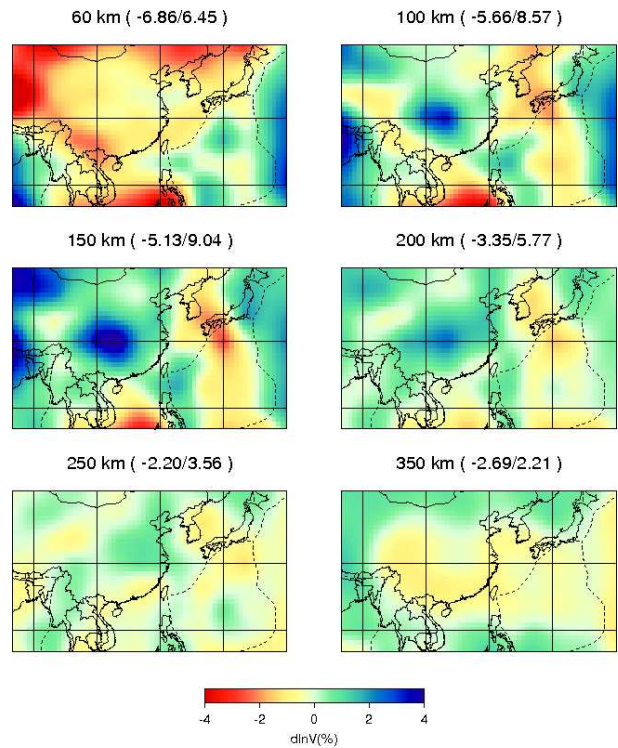


Figure 3.57: Same as figure 3.56 for the model developed using the non-linear Born partial derivatives.

inverse method to further improve our modeling.

## 27.5 Acknowledgements

This project has been funded through the Dept. of Energy, National Nuclear Security Administration, contract no. DE-FC52-04NA25543

## 27.6 References

- Capdeville, Y., An efficient Born normal mode method to compute sensitivity kernels and synthetic seismograms in the Earth, submitted to *Geophys. J. Int.*, 2005.
- Komatitsch, D. and J. P. Vilotte, The spectral element method: an effective tool to simulate the seismic response of 2D and 3D geological structures, *Bull. Seism. Soc. Am.*, 88, 368-392, 1998
- Li, X.D. and B. Romanowicz, Comparison of global waveform inversions with and without considering cross-branch modal coupling, *Geophys. J. Int.*, 121, 695-709, 1995.
- Marone, F. and B. Romanowicz, Non-linear crustal corrections in high resolution regional waveform seismic tomography, *Geophys. J. Int.*, in revision, 2006.
- Panning, M.P. and B. Romanowicz, A three-dimensional radially anisotropic model of shear velocity in the whole mantle, *Geophys. J. Int.* online early, doi: 10.1111/j.1365-246X.2006.03100.x, 2006.

## 28. Toward Constraints on Lateral S Wave Velocity Gradients around the Pacific Superplume

Akiko To, Barbara Romanowicz

### 28.1 Introduction

Global shear velocity tomographic models show two large-scale low velocity structures in the lower mantle, under southern Africa and under the mid-Pacific. While tomographic models show the shape of the structures, the gradient and amplitude of the anomalies are yet to be constrained. By forward modeling of Sdiffracted phases using the Coupled Spectral Element Method (CSEM, Capdeville *et al.*, 2003), we have previously shown that observed secondary phases following the Sdiff can be explained by interaction of the wavefield with sharp boundaries of the superplumes in the south Indian and south Pacific oceans (To *et al.*, 2005). We search for further constraints on velocity gradients at the border of the Pacific superplume all around the Pacific using a multi-step approach.

### 28.2 Preliminary Results

We have assembled a large dataset of Sdiff waveforms and travel time throughout the Pacific region. As shown in Fig.3.58, the new dataset has more sampling than the original one especially in the south Pacific. The original dataset was used to construct the original model, SAW24b16 (Mégnin and Romanowicz, 2000). We first apply a finite frequency tomographic inversion methodology (NACT, Li and Romanowicz, 1996), which provides a good starting 3D model. In particular, the inversion method allows us to position the fast and slow anomalies and their boundaries quite well, as has been shown previously, but underestimates the gradients and velocity contrasts. The result of the inversion using the newly obtained dataset shows shrinking of the Pacific superplume area in its northern and southern edge (Fig.3.59). Based on this starting model, we will perform forward modeling to search for further constraints on the gradients at the boundary of the Pacific superplume.

### 28.3 Acknowledgements

The data were downloaded from IRIS DMC and CNSN.

### 28.4 References

Li, X.D. and B. Romanowicz, Global mantle shear-velocity model developed using nonlinear asymptotic coupling theory, *Geophys. J. R. Astr. Soc.*, 101, 22,245-22,272, 1996.

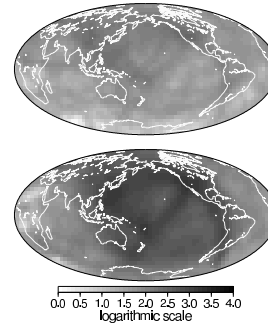


Figure 3.58: Sampling density of the collected Sdiff data. Top: The Sdiff phase raypath distribution of the previously collected dataset. The data is used in the construction of the original model, SAW24B16. Bottom: The raypath distribution of the newly obtained dataset. Compared to the previous dataset, there are more samplings in the south Pacific.

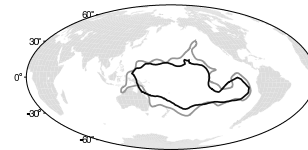


Figure 3.59: Contours of the Pacific superplume. Gray line: Original model, SAW24B16. Black line: New model, obtained from the recently collected dataset. The lines are the contour lines of -0.4% S velocity anomaly at a depth of 2820km. The east sides of the contours overlap each other, whereas the contours are shifted on the north and south side in the new model.

Mégnin C. and B. Romanowicz, The three-dimensional shear velocity structure of the mantle from the inversion of body, surface and higher-mode waveforms. *Geophys. J. Int.*, 143, pp. 709-728, 2000

Capdeville, Y., A. To and B. Romanowicz, Coupling spectral elements and modes in a spherical earth: an extension to the "sandwich" case, *Geophys. J. Int.*, 154, 44-57, 2003

To, A., B. Romanowicz, Y. Capdeville and N. Takeuchi, 3D effects of sharp boundaries at the borders of the African and Pacific Superplumes: observation and modeling, *Earth and Planet. Sci. Lett.*, 233, 137-153, 2005

## 29. Joint Inversion for 3D Velocity Structure of the Broader Africa-Eurasia Collision Region

Suzan van der Lee (Northwestern University), Heather Bedle (Northwestern University), Megan Flanagan (LLNL), Eric Matzel (LLNL), Michael Pasyanos (LLNL), Federica Marone, Barbara Romanowicz, Christian Schmid (ETH Zurich), Arthur Rodgers (LLNL),

### 29.1 Introduction

The need to monitor broader areas and an increasing number of nations with nascent nuclear weapons programs has led to major challenges to nuclear explosion monitoring research. Agencies must, in fact, be prepared to detect, identify and locate nuclear explosions in wide regions, often aseismic and lacking previous seismic observations. Since the 1980's, the importance of monitoring at regional distances has been well established. However, such monitoring is complicated by the passage of seismic waves through the structurally complex crust and uppermost mantle. As a consequence, traveltimes and amplitudes of regional phases show great variability leading to large uncertainties in event locations and decreased performance of regional discriminants. A major requirement for the accurate modeling of regional seismic data, and therefore improved event locations and regional discriminant performance, are 3D regional velocity models characterized by high resolution from the crust down to the transition zone.

Our aim is a 3D velocity model of the crust and upper mantle for the geographic region extending from the western Mediterranean to Pakistan, including the aseismic region of North Africa. The joint inversion of different types of seismic data with diverse sensitivity to the crust and mantle is essential to achieve a high resolution image of the structure in this tectonically complex area, where six major tectonic plates and several microplates interact with each other. We expect predictions for seismogram characteristics (phase arrival times, amplitudes, dispersion) based on this new model to match most observations and be useful for event discrimination. Simultaneously, the new model will refine our understanding of the structure and tectonics in the study region.

### 29.2 Technical approach and dataset

Our 3D  $S$ -velocity model will be derived from the joint inversion of regional waveform fits, surface wave group velocity measurements, teleseismic arrival times of  $S$  and  $P$  waves, receiver functions and published results from active source experiments. The strength of jointly using various datasets lies in their redundancy (increase in the results accuracy) and complementarity (resolving power increase and trade-offs reduction).

The fitting of regional fundamental and higher mode Rayleigh waveforms has been accomplished using the Partitioned Waveform Inversion method (Nolet, 1990)

for thousands of paths covering the study area (Figure 3.60). The modeling of both fundamental and higher mode surface waveforms ensures resolution of the entire upper mantle structure down to the transition zone. The inclusion in the inversion of teleseismic arrival times will further boost the resolving power at mid and deep upper mantle levels, while group velocity measurements and constraints on crustal thickness from active-source literature and receiver function analysis will ensure high resolution in the shallow upper mantle.

The seismograms used in this work have been recently recorded by a variety of different stations and networks, both permanent and temporary, operating in the study region: MIDSEA deployment, Kuwait National Seismic Network (KNSN), the United Arab Emirates (UAE) Broadband deployment, the Jordan deployment, the Eastern Turkey Seismic Experiment (ETSE), the Caspian Broadband deployment, the Global Seismic Network (GSN), the International Monitoring System (IMS), MedNet and Geofon. While each of these waveform datasets is valuable on its own, their combination is unique and key to this study.

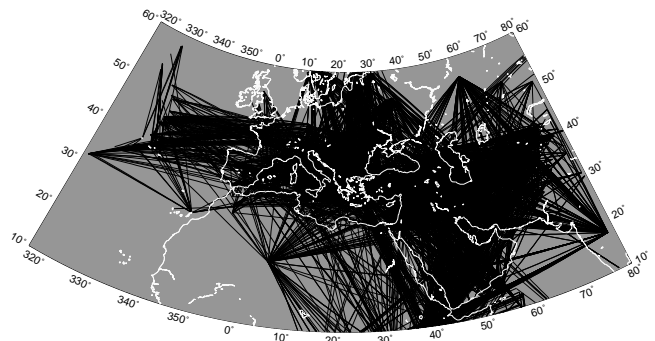


Figure 3.60: Great circle wave paths for the vertical and radial component seismograms used in this study to date.

### 29.3 Preliminary results

The broad consistency between seismic velocity anomalies inferred from existing and performed measurements of teleseismic arrival times and Rayleigh wave group velocities as well as from regional waveform fits implies that these different types of dataset are at least in part redundant. The consistency further shows that the datasets record the same structural phenomena, despite

differences in size and character between typical sensitivity kernels for each dataset.

The preliminary model (Figure 3.61) obtained by jointly inverting linear constraints provided by the performed waveform fits and collected point constraints on crustal thickness from active-source seismic studies and receiver function analysis shows that the uppermost mantle in the study area is strongly heterogeneous, reflecting the complex tectonics of this region. Particularly low velocities are observed at 100km depth beneath the Mid-Atlantic Ridge, the East African Rift and the western Mediterranean basin. Lower velocities than average are also present deeper (150-200 km) beneath Turkey and western Arabia. High velocity mantle material has been imaged at 100 km depth in correspondence with the Russian Platform and the Ukraine Shield. Linear high velocity features, possibly representing subducted material, are observed in the central Mediterranean basin (Italy and Greece) and beneath the Zagros Mountains Range in Iran (e.g. at 150 km depth).

The observed large scale features of our preliminary model are in agreement with existing regional models (e.g. *Marone et al., 2004; Maggi and Priestley, 2005*).

## 29.4 Future of the project

Our final 3D  $S$ -velocity model will be derived from the joint inversion of regional waveform fits, surface wave group velocity measurements, teleseismic arrival times of  $S$  and  $P$  waves, receiver functions and published results from active source experiments. This model will be converted to a 3D  $P$ -velocity model, using both published data on elastic properties (and their partial derivatives with temperature and pressure) of mantle rocks and empirical information provided by measured arrival times of teleseismic  $P$  and  $Pms$  waves. This new  $P$ -wave model will provide an improved ability to locate seismic events.

The prediction and calibration of regional traveltimes and waveforms depend strongly on the methodology used to compute synthetic traveltimes and waveforms from a 3D velocity model. Our goal is to test the obtained  $S$ - and  $P$ -wave models' ability to predict regional  $P$  and  $S$  traveltimes, deflect wave paths and deform waveforms using different approximations (e.g. path average vs. exact numerical approaches). We will assess the effects of 3D heterogeneities first on the studied seismograms (traveltimes and waveforms) and subsequently on the 3D models derived from these data.

## 29.5 Acknowledgements

This work has been financially supported by the National Nuclear Security Administration, Office of Nonproliferation Research and Engineering and Office of Defense Nuclear Nonproliferation (DE-FC52-04NA25542).

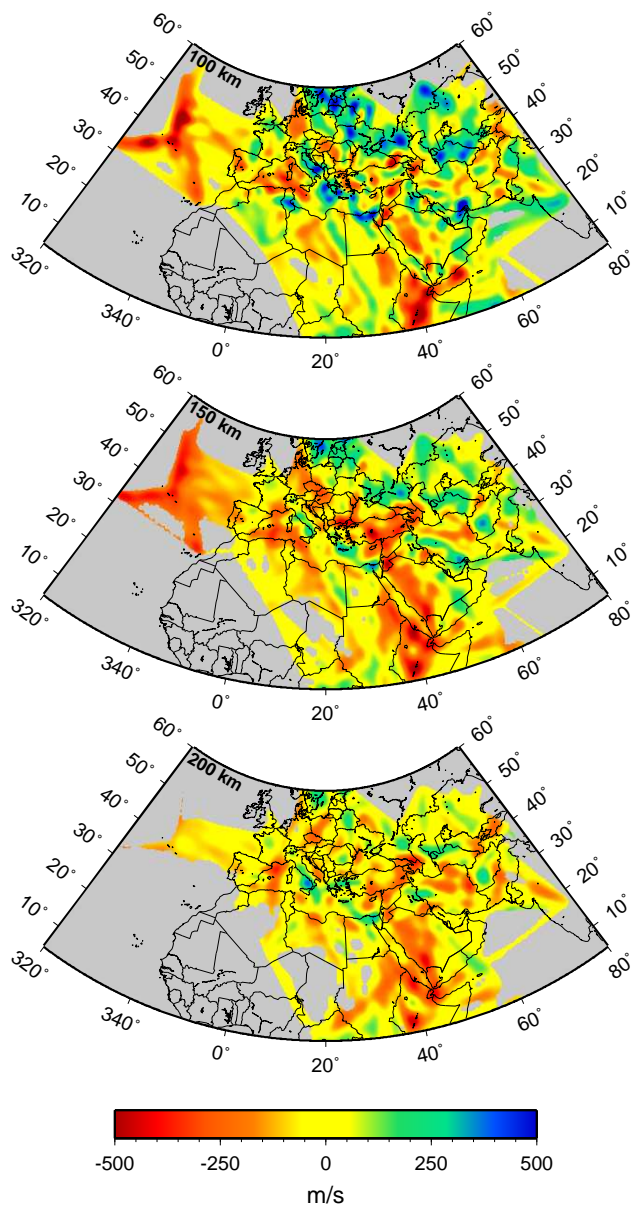


Figure 3.61: Horizontal slices at different depths through our preliminary upper mantle model. Anomalies are relative to a 1D average model for the Mediterranean region.

## 29.6 References

- Maggi, A. and K. Priestly, Surface waveform tomography of the Turkish-Iranian Plateau, *Geophys. J. Int.*, 160, 1068-1080, 2005.
- Marone, F., S. van der Lee and D. Giardini, 3-D upper mantle  $S$ -velocity model for the Eurasia-Africa plate boundary region, *Geophys. J. Int.*, 158, 109-130, 2004.
- Nolet, G., Partitioned waveform inversion and two-dimensional structure under the network of autonomously recording seismographs, *J. Geophys. Res.*, 95, 8499-8512, 1997.

## 30. A Three Dimensional Radially Anisotropic Model of Shear Velocity in the Whole Mantle

Mark Panning (now at Princeton) and Barbara Romanowicz

### 30.1 Introduction

The 3D seismic velocity structure of the Earth’s mantle represents a snapshot of its current thermal and chemical state. As tomographic models of the isotropic seismic velocity converge in their main features (*Masters et al., 2000; Mégnin and Romanowicz, 2000; Ritsema and van Heijst, 2000; Gu et al., 2001*), geodynamicists can use them to infer the density structure, and thus the buoyancy contrasts which drive mantle convection. This process, however, is complicated by the difficulty of separating thermal and chemical contrasts, and the lack of direct sensitivity of seismic velocities to the density contrasts which drive the convection.

In many regions of the mantle, analyzing the anisotropy of seismic velocities can give us another constraint on mantle dynamics. Random orientations of the anisotropic minerals which make up the mantle tend to cancel out on the macroscopic scale observable by seismic waves, unless crystals or materials with strongly contrasting elastic properties are aligned through deformation processes. While in the relatively cold regions of the lithosphere these anisotropic signatures can remain frozen in over geologic time-scales (*Silver, 1996*), observed anisotropy at greater depths likely requires dynamic support (*Vinnik et al., 1992*). Thus, the anisotropy observed at sub-lithospheric depths is most likely a function of the current mantle strain field, and these observations can help us map out mantle flow.

### 30.2 Model results

We have developed a 3D radially anisotropic S velocity model of the whole mantle (SAW642AN; *Panning and Romanowicz, 2006*), obtained using a large three component surface and body waveform dataset and an iterative inversion for structure and source parameters based on Nonlinear Asymptotic Coupling Theory (NACT) (*Li and Romanowicz, 1995*). The model is parameterized in level 4 spherical splines, which have a spacing of  $\sim 800$  km. The model shows a link between mantle flow and anisotropy in a variety of depth ranges.

In the uppermost mantle, we confirm previous observations of regions with  $V_{SH} > V_{SV}$  starting at  $\sim 80$  km under oceanic regions and  $\sim 200$  km under stable continental lithosphere (*Gung et al., 2003*), suggesting horizontal flow beneath the lithosphere (figure 3.62). We also observe a  $V_{SV} > V_{SH}$  signature at  $\sim 150$ -300 km depth beneath major ridge systems with amplitude correlated with spreading rate for fast-spreading segments. In the transition

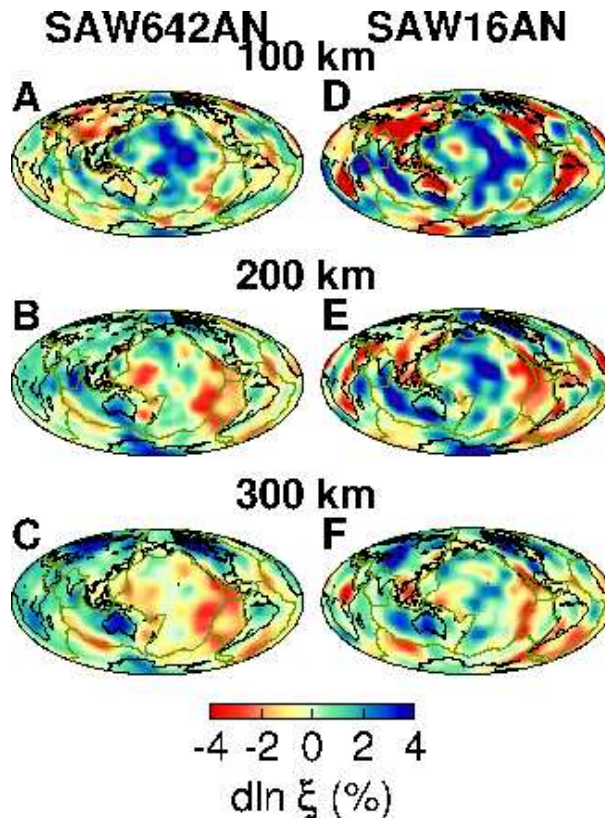


Figure 3.62: Comparison between SAW642AN  $\xi$  (A-C) and the upper mantle  $\xi$  calculated from SAW16AN (*Gung et al., 2003*) (D-F) at depths of 100 (top), 200 (middle), and 300 km (bottom).

zone (400-700 km depth), regions of subducted slab material are associated with  $V_{SV} > V_{SH}$  (figure 3.63), while the ridge signal decreases. We also confirm the observation of radially symmetric  $V_{SH} > V_{SV}$  in the lowermost 300 km (*Panning and Romanowicz, 2004*). The 3D deviations from this signature (figure 3.64) are associated with the large-scale low-velocity superplumes under the central Pacific and Africa, suggesting that  $V_{SH} > V_{SV}$  is generated in the predominant horizontal flow of a mechanical boundary layer, with a change in signature related to transition to upwelling at the superplumes.

### 30.3 Acknowledgements

This research was supported by NSF grant EAR-0308750.

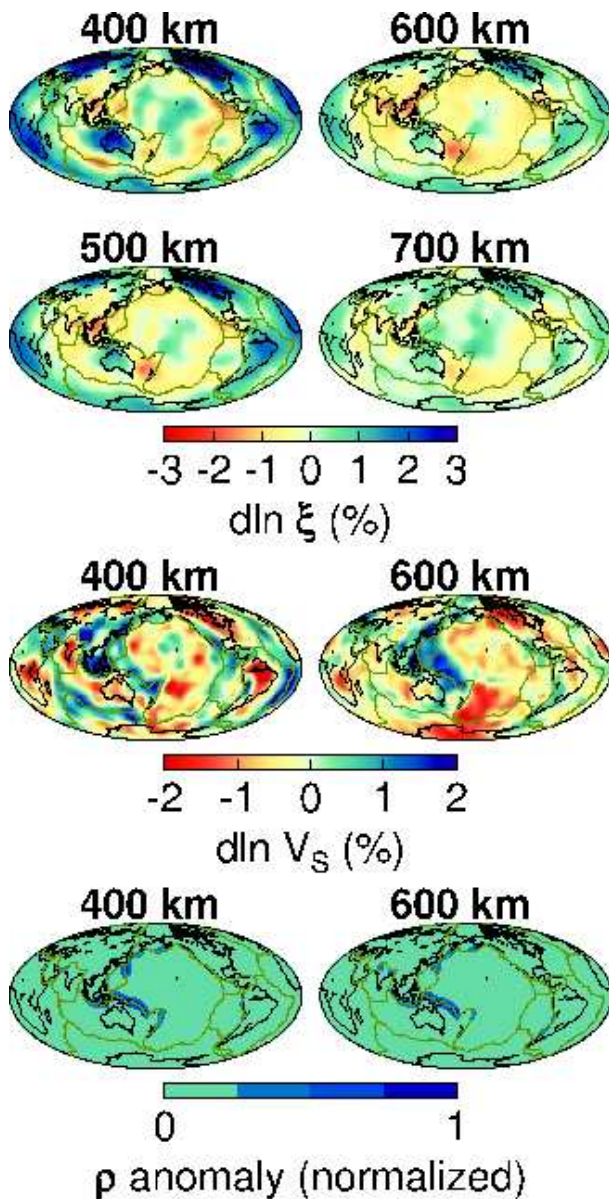


Figure 3.63:  $\xi$  structure at depths 400-700 km (top two rows) and  $V_S$  at depths of 400 and 600 km (third row). The bottom row shows the density anomalies for layers centered at depths of 362.5 km (left) and 652.5 km (right) for the model of Lithgow-Bertelloni and Richards (1998), normalized to the maximum density anomaly in each depth range.

### 30.4 References

Gu, Y.J., A.M. Dziewonski, W. Su, and G Ekström, Models of the mantle shear velocity and discontinuities in the pattern of lateral heterogeneities, *J. Geophys. Res.*, **106**, 11,169-11,199, 2001.

Gung, Y., M. Panning and B. Romanowicz, Global anisotropy and the thickness of continents, *Nature*, **422**,

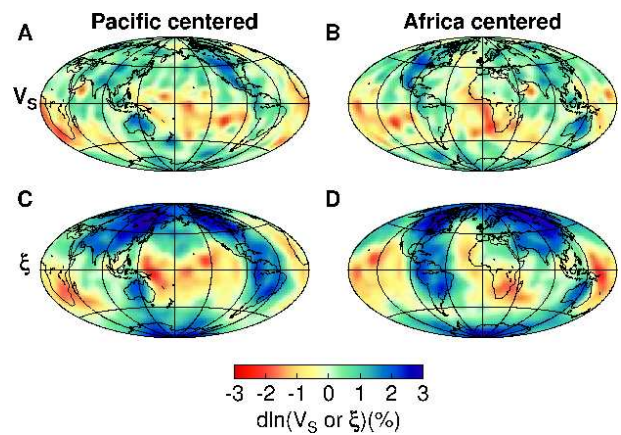


Figure 3.64:  $V_S$  (A,B) and  $\xi$  structure (C,D) at a depth of 2800 km centered under the central Pacific (A,C) and Africa (B,D)

707-711, 2003.

Li, X.D. and B. Romanowicz, Comparison of global waveform inversions with and without considering cross-branch modal coupling, *Geophys. J. Int.*, **121**, 695-709, 1995.

Lithgow-Bertelloni, C. and M. Richards, The dynamics of Cenozoic and Mesozoic plate motions, *Rev. Geophys.*, **36**, 27-78, 1998.

Masters, G., G. Laske, H. Bolton and A. Dziewonski, The relative behavior of shear velocity, bulk sound speed, and compressional velocity in the mantle: implications for chemical and thermal structure, in *Earth's Deep Interior*, AGU Monograph 117, pp. 63-86, eds. Karato, S., A.M. Forte, R.C. Liebermann, G. Masters and L. Stixrude, Amer. Geophys. Union, Washington, D.C., 2000.

Mégnin, C., and B. Romanowicz, The 3D shear velocity of the mantle from the inversion of body, surface, and higher mode waveforms, *Geophys. J. Int.*, **143**, 709-728, 2000.

Panning, M.P. and B. Romanowicz, A three-dimensional radially anisotropic model of shear velocity in the whole mantle, *Geophys. J. Int.* online early, doi: 10.1111/j.1365-246X.2006.03100.x, 2006.

Ritsema, J. and H.-J. van Heijst, Seismic imaging of structural heterogeneity in Earth's mantle: evidence for large-scale mantle flow, *Science Progress*, **83**, 243-259, 2000.

Silver, P.G., Seismic anisotropy beneath the continents: probing the depths of geology, *Annu. Rev. Earth Planet. Sci.*, **24**, 385-432, 1996.

Vinnik, L.P., L.I. Makeyeva, A. Milev and Y. Usenko, Global patterns of azimuthal anisotropy and deformations in the continental mantle, *Geophys. J. Int.*, **111**, 433-447, 1992.

## 31. Short Wavelength Topography on the Inner Core Boundary

Aimin Cao, Yder Masson, and Barbara Romanowicz

### 31.1 Introduction

The ICB separates the liquid outer core from the solid inner core and is the site of important dynamical processes, as the core freezes and light elements are expelled to power convection in the outer core (Glatzmeier and Roberts, 1995). Significant long wavelength topography of the ICB is ruled out by dynamical considerations (Buffett, 1997). While hemispherical variations in the seismic properties at the top of the inner core have been documented, seismological investigations indicate that the ICB is, to a good approximation, quite spherical. However, the observation of significant PKiKP coda, likely due to multiple scattering (Poupinet and Kennett, 2004), indicates that the structure of the ICB is more complex at short wavelengths. There is also evidence for significant scattering near the top of the inner core (Vidale and Earle, 2000). Recently, in a study of amplitudes of ICB reflected phases (PKiKP), Krasnoshchekov *et al.* (2005) have proposed that the ICB is “patchy” in its reflective properties at scales of 10-200km laterally. Because their data were obtained at sub-critical distances, these authors could not constrain the precise nature of the variability in the measured PKiKP amplitudes.

In their efforts to constrain the rate of differential rotation of the inner core previously estimated using PKP(DF-BC) differential travel times on paths to Alaska stations in the epicentral distance range  $147-155^\circ$ , Zhang *et al.* (2005) found several high quality earthquake doublets in the South-Sandwich region, separated in time by a decade or more. The high waveform similarity at many stations indicates that the two sources are located within a wavelength for compressional waves. One of the earthquake doublets reported in the Zhang *et al.* study is of exceptional quality (Dec 1, 1993/ Sep 6, 2003). Highly similar waveforms for both events were recorded at 102 stations with a broad coverage of epicentral distances and azimuths, and the hypocenter separation of the two events was inferred to be 100 m vertically and less than 1.0 km horizontally.

### 31.2 Data, Method, and Results

We found that this doublet was also well recorded on the short-period Yellowknife Seismograph Array (YK) in northern Canada, which is located in an optimal position for the study of mantle phases PP as well as both refracted (PKIKP) and post-critically reflected (PKiKP) core phases. Indeed, these phases are emitted near the maximum in the lobe of the doublet’s radiation pattern (Figure 3.65), at an epicentral distance of  $137.8^\circ$ , where

the two core phases are well separated and where the PKiKP undergoes total reflection. High signal-to-noise seismic waveforms were recorded for both events at eighteen of the nineteen YK stations. In a 50-second time window around the PP phases of the doublet, unfiltered waveforms are very highly similar at all stations of the array, with cross-correlation coefficients larger than 0.97. The amplitudes of PP for both events differ only by a factor of 1.05. This provides strong additional confirmation of the high quality of this doublet. We therefore expect the waveforms of other phases to be very similar in shape and amplitude for this special doublet.

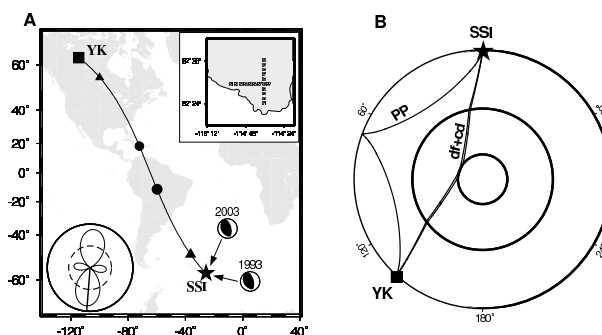


Figure 3.65: (A) Yellowknife Seismic Array (YK) and the doublet. The 19 stations of the array form two arms, one along a lake (shore indicated) and one orthogonal to it. Its aperture is 25 km with a station interval of 2.5 km (upper-right inset). The doublet consists of two South Sandwich Islands (SSI) events at an epicentral distance of  $137.8^\circ$ : Dec 1, 1993,  $m_b=5.5$ , depth=33 km according to the PDE catalog; and Sept. 6, 2003,  $m_b=5.6$ , depth=33 km according to the PDE catalog. According to Harvard CMT (<http://www.seismology.harvard.edu>), scalar moments and depths are ( $M_o=3.53 \times 10^{24}$  dyne-cm,  $h=45$  km) and ( $M_o=4.02 \times 10^{24}$  dyne-cm,  $h=44$  km), respectively. The lower-left inset is the P-wave radiation pattern of the doublet based Harvard CMT moment tensors. Black triangles and dots are entry (exit) points of PKIKP at the ICB and the CMB, respectively. (B) Ray paths of PP, PKIKP(df), and PKiKP(cd) phases used in this study.

However, the first two arrivals (PKIKP and PKiKP) in the individual unfiltered YK seismograms, which are well separated for both events, have significantly different waveforms (Figure 3.66A). For the 2003 event, the waveforms of PKiKP are simply reversed in polarity with respect to those of PKIKP as theoretically predicted

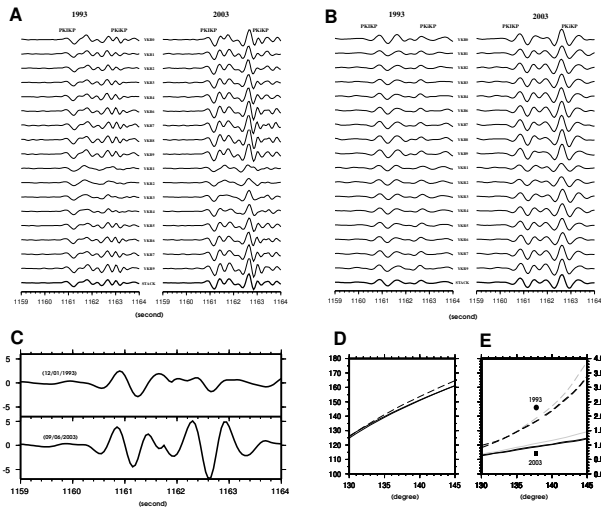


Figure 3.66: (A) Original waveform profile of PKIKP and PKiKP phases. For each event, waveforms are highly similar at most of stations except YKR1, YKR2, and YKR3 stations. These three stations are close to the lake, and they have a common feature for both events: site-related filtering of higher frequencies. (B) Bandpass filtered waveform profile of PKIKP and PKiKP phases (from 1.0 to 2.0 Hz). In this frequency range, waveforms of PKIKP and PKiKP are highly similar at all stations (including YKR1, YKR2, and YKR3) for each event. Also, waveform shapes of PKIKP and PKiKP for the 1993 event are more similar to those of the 2003 event. In this profile, it is obvious that phase shifts between PKiKP and PKIKP are close to  $180^\circ$  as predicted theoretically. (C) Linearly stacked waveforms of PKIKP and the reversed PKiKP phases after bandpass filtering (1-2Hz) showing the similarity of shape. Vertical broken line indicates place where the PKiKP waveform has been cut and reversed. The amplitude of PKIKP for 2003 event is 1.5 times larger than that for 1993 event; the amplitude of PKiKP for 2003 event is 7.2 times larger than that for 1993 event. Amplitude ratios of PKIKP to PKiKP are 2.3 (1993) and 0.7(2003) event. (D) Theoretical phase shifts of PKiKP with respect to PKIKP based on PREM, IASPEI91, and AK135 reference models. In this study, the phase shift is  $\sim 145^\circ$ . (E) Theoretical amplitude ratios of PKIKP to PKiKP. Dashed lines are assuming that the inner core  $Q_\alpha = \infty$  (i.e., no seismic attenuation in the inner core) based on the above three reference models. Solid lines are using  $Q_\alpha = 445$  provided in PREM model. The black dot and square are observed amplitude ratios of PKIKP to PKiKP for the 1993 and 2003 events, respectively.

for post-critical reflections (Figure 3.66D). For the 1993 event, the amplitudes of PKiKP are much reduced (by a factor of 3.0). The later part of the PKiKP waveform also shows some change. In the frequency range 1-2 Hz, PKIKP and PKiKP waveforms of both events are simpler (Figure 3.66B), so that reversed waveforms of PKiKP are similar to those of PKIKP for both events (Figure 3.66B,C). In this frequency range, where the amplitude ratios can be determined more robustly, the amplitudes of PKiKP for 2003 and 1993 events differ by a factor of 7.2. Given the striking similarity of the PP waveforms and their coda, and the other evidence for the quality of the doublet, we infer that both phases (especially the PKiKP phase) have undergone temporal changes within 10 years.

This observation, complemented by data from several other doublets, indicates the presence of topography at the inner-core boundary, with a horizontal wavelength of about 10 km. Such topography could be sustained by small scale convection at the top of the inner core, and is compatible with a rate of super-rotation of the inner core of  $\sim 0.1$ - $0.15$  deg/year. In the absence of inner core rotation, decadal scale temporal changes in the ICB topography would provide an upper bound on the viscosity at the top of the inner core.

### 31.3 Acknowledgements

We thank the operators of Yellowknife Seismic Array and Canadian National Seismograph Network. This work was partially supported by the NSF.

### 31.4 References

Glatzmeier, G.A., P. H. Roberts, A three-dimensional self-consistent computer simulation of a geomagnetic field reversal, *Nature*, 377, 203, 1995.  
 Buffett, B.A., Geodynamic estimates of the viscosity of the earth's inner core, *Nature*, 388, 571, 1997.  
 G. Poupinet, B.L.N. Kennett, On the observation of high frequency PKiKP and its coda in Australia, *Phys. Earth Planet. Inter.*, 146, 497, 2004.  
 J.E. Vidale, P.S. Earle, Slow differential rotation of the Earth's inner core indicated by temporal changes in scattering, *Nature*, 404, 273, 2000.  
 D.N. Krasnoshechekov, P.B. Kaazik, V.M. Ovtchinnikov, Seismological evidence for mosaic structure of the surface of the Earth's inner core, *Nature*, 435, 483, 2005.  
 Zhang, J., et al., Inner core differential rotation confirmed by earthquake waveform doublets. *Science*, 309, 1357 2005.

## 32. Long Period Seismology on Europa

Fabio Cammarano, Mark Panning, Ved Lekic, Michael Manga, Barbara Romanowicz

### 32.1 Introduction

Seismological observations provide unparalleled capability for studying planetary interiors. While seismological studies of the Earth and, to a lesser extent, the Earth’s Moon have placed strong constraints on the internal structure and dynamics of these bodies, the absence of seismic measurements on other planetary bodies has stymied analysis of their detailed structures. There are a wide variety of internal compositions and structures hinted at by recent exploration of the Jovian and Saturnian systems. In order to inform future mission design, it is important to determine what observations hold potential for answering outstanding questions concerning planetary interiors.

Physically consistent models of planetary bodies, constrained by moment of inertia measurements and by well-characterized elastic and anelastic properties of relevant minerals, make possible the study of the seismic response of planetary bodies, even when seismic measurements are not yet available.

Here, we summarize the main results of such interdisciplinary approach for the Jupiter’s moon Europa. We develop a menagerie of physically consistent models of Europa (Cammarano *et al.*, 2006) which allows us to explore which seismic measurements on Europa have the potential to answer the many outstanding questions about its structure and current thermal state (Panning *et al.*, 2006).

### 32.2 Physically consistent interior models

We calculate a range of thermodynamically consistent models for the physical structure of Europa, as constrained by the satellite’s mass and moment of inertia. We start with either a pyrolitic or a chondritic mantle composition and a core of either pure iron or iron plus 20% sulfur. The models completely characterize the radial seismic structure, i.e. elastic and anelastic properties, and they can be used to compute the seismic response of the planet.

The coupling between the thermal state of the ice shell and its viscosity dictates the ice-shell thickness and its seismic properties. It is likely that attenuation could be very high within the “warm”, convective part of the ice shell. Due to the feedback between radiogenic and tidal heating, two extreme thermal profiles are possible in the mantle (see Figure 1). Strong dispersion and dissipation are expected in the hot convective mantle, while anelasticity effects will be much weaker in the case of the cold

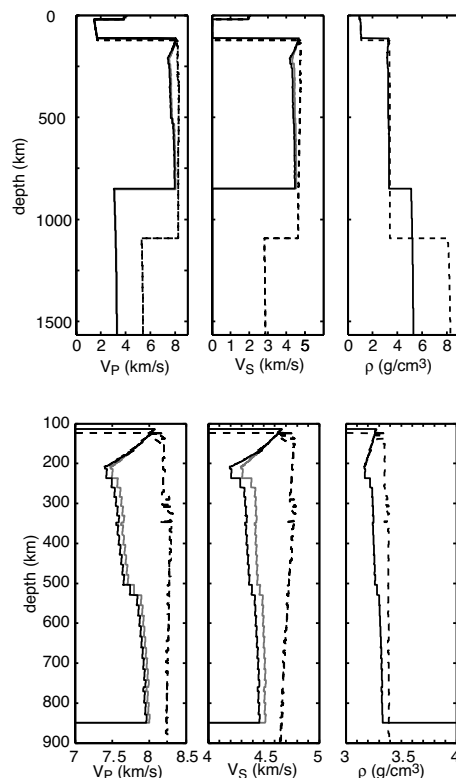


Figure 3.67: Physically consistent models for hot (solid lines) and cold (dashed) thermal structures with a pyrolitic mantle. Purely elastic models without dissipative effects are shown in light gray. The bottom panel shows a mantle close-up of the same models.

mantle. There is a strong relationship between different thermal structures and compositions. The “hot” mantle may well keep temperatures high enough to be consistent with a liquid core made of iron plus light elements. In the case of the “cold scenarios”, the possibility of a solid iron core cannot be excluded and it may even be favored. The depth of the ocean and of the core-mantle boundary are determined with high precision once we assume a composition and thermal structure. Furthermore, the depth of the ocean is not very sensitive to the core composition used.

### 32.3 Predicted Seismic Response

The normal modes for the determined seismic radial structures of Europa are computed with the MINOS code (Woodhouse, 1988). Seismograms for any proposed

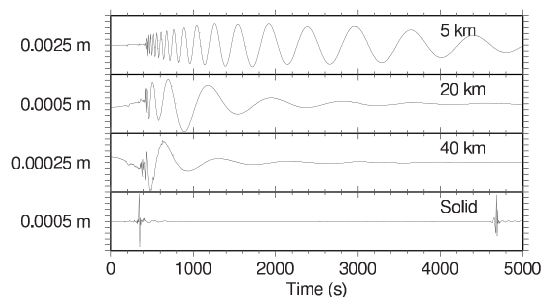


Figure 3.68: Synthetic displacement seismograms at a distance of  $25^\circ$  (680 km) from the  $M_W = 5$  normal event. Seismograms are calculated for the low-attenuation cold chondritic model with ice shell thicknesses (from top) of 5, 20, 40, and a solid 137 km thick ice layer model. The maximum amplitude for each panel is shown to the left of the panel.

source and receiver configuration can then be modeled using normal mode summation, which models the complete broadband seismic wavefield. Given the normal mode catalogs and a predicted seismic source process, we can compute synthetic seismograms at any distance from the source. The seismograms presented here assume a  $M_W = 5$  (seismic moment of  $3.94 \times 10^{16}$  Nm) normal faulting source, as proposed in *Nimmo and Schenk (2006)*. For simplicity, we used a dip-slip event with a  $45^\circ$  dip and  $90^\circ$  rake. We computed all modes up to 0.1 Hz, and then bandpass filtered the seismograms with corner frequencies at 12 and 800 seconds period, and cut-off frequencies at 10 and 1000 seconds period. We send to *Panning et al. (2006)* for a detailed discussion about measurement requirements and potential for answering questions on Europa's interior. Compared to high frequency signals, that require a surface installation, long-period measurements can be acquired potentially by an orbiter. Unless an orbiter is at the correct altitude for geosynchronous orbit, the seismic measurements will be made at a moving point on the surface. This presents additional challenges, but may provide us with interesting methods for determining surface wave velocities from a single measurement. To test this, we adapted the mode summation code to synthesize seismograms at a moving observation point. Seismic displacement from an event that occurs near the trajectory of the orbiter recorded on an observation point moving away from the source location produces a seismogram at sufficient time after the event with a resonant frequency (Figure 3). This resonance is caused by a wavepacket of a given frequency having a group velocity which closely matches the velocity of the observation point. Because the frequency at which the group velocity will match a given orbital velocity depends on the ice shell model, an observation of this resonance phenomenon may be diagnostic.

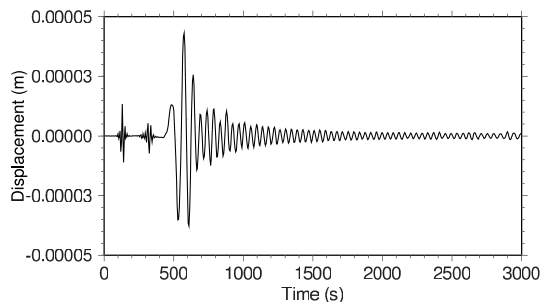


Figure 3.69: 3000 seconds of seismic displacement (in m) for an observation point that starts  $15^\circ$  (410km) east of the source at the event origin time, and moves north with an apparent surface velocity of 1.4 km/s calculated in the low attenuation 5 km thick ice shell model. The arrivals at about 120 s and 350 s are the P and S waves respectively.

## 32.4 Conclusions

Long-period seismic observations on Europa have potential to greatly expand our knowledge of the satellite. Long-period displacement measurements with millimeter accuracy may be able to determine the current tectonic activity of Europa's surface, the presence of a liquid ocean, and the thickness of the ice shell. These observations hold considerable promise relative to shorter period acceleration and velocity measurements, as the peak amplitudes occur at frequencies that minimize the complications from unknown 3D heterogeneity and finite source dimension and duration. Such displacement measurements may be possible from orbit, but many instrument design and data processing details need to be carefully considered. Determination of deeper structure with seismic measurements is much more difficult in the presence of a global liquid subsurface ocean, which acts to decouple deeper seismic energy from the surface.

## 32.5 References

- Cammarano, F., Lekic, V., Manga, M., Panning, M., Romanowicz, B. (2006) Long-period seismology on Europa: I. Physically consistent models, *J. Geophys. Res. - Planets*, in press.
- Nimmo, F., Schenk, P. (2006), Normal faulting on Europa: implications for ice shell properties, *J. Struct. Geol.*, in press.
- Panning, M., Lekic, V., Manga, M., Cammarano, F., Romanowicz, B. (2006) Long-period seismology on Europa: II. Predicted Seismic Response *J. Geophys. Res. - Planets*, in press.
- Woodhouse, J.H., (1988) The calculation of eigenfrequencies and eigenfunctions of the free oscillations of the Earth and the Sun, *Seismological Algorithms*, 321-370, ed. Doornbos, D.J.

## 33. Tidal Excitation of Free Oscillations of Icy Satellites

Vedran Lekic and Michael Manga

### 33.1 Motivation

Small bodies, lacking both significant heat of accretion and possessing large surface to volume ratios, were thought to lack significant internal sources of heat, and therefore to be geologically dead. However, exploration of Jovian and Saturnian systems by the Voyager spacecraft revealed that the surfaces of a number of satellites were actively modified by volcanic and tectonic processes. Europa, Jupiter’s third-largest satellite, is marked by many fractures, yet few craters, indicative of a geologically young, active surface. Subsequent study by the Galileo probe confirmed the existence of an ocean beneath its icy shell (*Kivelson et al.*, 2000). Images of Enceladus, a smallish moon of Saturn, revealed a highly reflective surface marked by large tectonic features. Recently, the Cassini probe found anomalously high temperatures at ice fractures near Enceladus’ south pole (*Spencer et al.*, 2006), and a diffuse plume of water molecules reaching hundreds of kilometers above the surface (*Hansen et al.*, 2006).

Tidal dissipation appears to be an important source of heat for the Galilean satellites, which are locked in orbital resonances which force orbital eccentricities. Eccentric orbits allow transfer of orbital/rotational energy to internal heat even for synchronously rotating satellites. The efficiency of this transfer is related to the anelasticity of the moon in question, which causes a phase lag between the tidal forcing and the resulting deformation, and is on the order of  $10^{-4}$  (*Hussman and Spohn*, 2004). Tidal excitation of free oscillations may be a more efficient mechanism of tidal heating, but has heretofore been neglected, due to the assumption that frequencies of free oscillations are incompatible with those of tidal forcing.

Europa’s subsurface ocean is a potential habitat for life (e.g. *Marion et al.*, 2003). Orbital modeling that includes the effects of thermal dissipation indicates that heat dissipation within Europa has varied through time, causing the thickness of the liquid ocean to oscillate (e.g. *Hussmann and Spohn*, 2004). In order to ascertain the potential for life in the European ocean, it is important to identify possible tidal dissipation feedback mechanisms that would work to stabilize the ocean on geological timescales. We propose to study the effects of tidal excitation of free oscillations for a variety of ice-shell/ocean models of Europa, and to quantify the resulting heat deposition.

Widespread fracturing and heating of water ice on Enceladus cannot be explained by heat dissipation through tidal deformation (e.g. *Poirier et al.*, 1983;

*Porco et al.*, 2006). Furthermore, tidal forcing on Enceladus is comparable to that experienced by other moons that, despite their larger size and radioactive heat budget, do not exhibit signs of geological activity. We propose to investigate the possibility of tidal excitation of free oscillations on Enceladus as a more efficient means of orbital-to-heat energy transfer.

### 33.2 Method

We adopt the approach of *Press and Teukolsky* (1977), in which the tidal potential is projected onto the normal modes, and the amount of tidal normal mode coupling is quantified in terms of an overlap integral

$$A_n(\omega) = \int_V \xi_n \cdot \nabla \tilde{U}(\omega) dv, \quad (3.2)$$

where the subscript  $n$  is the mode identifier,  $\xi_n$  is the eigenfunction in question,  $\nabla \tilde{U}(\omega)$  is the gradient of the potential in the frequency domain,  $\omega$  is the relevant frequency of oscillation, and integration is carried out over the perturbed body. The energy deposited into the mode is then simply

$$\Delta E_n = 2\pi^2 |A_n(\omega)|^2. \quad (3.3)$$

We can see that tidal excitation of free oscillations requires that the tidal forces overlap with a given mode both spatially and in the frequency domain. Studies of tidal excitation of stellar oscillations (*Wu and Murray*, 2003) demonstrate that spatial overlap falls rapidly with increasing radial order of the mode under consideration.

Quantifying frequency overlap requires both calculating the frequency spectrum of tidal forcing and the frequencies of the body’s free oscillations. For Europa, we consider the tidal effects of Jupiter, Io, and Ganymede, and plot the dominant frequencies of forcing from these bodies in Figure 1. We expect Saturn, Dione and Rhea to contribute significantly to tidal forces acting on Enceladus, and we plot the relevant dominant frequencies in Figure 2. Next, we proceed to calculate a range of possible frequencies for the  ${}_0S_2$  mode of oscillation (“the football mode”) by considering a set of 1D models of elastic velocity and density for Enceladus and Europa. In order to calculate the frequencies and functions describing the free oscillations of a spherically symmetric body, we employ the MINOS code (*Woodhouse*, 1988). At present, we neglect effects of viscosity.

### 33.3 Preliminary Results

Figure 3.70 shows that the frequency of  ${}_0S_2$  on Europa decreases with decreasing thickness of its subsurface ocean. We use the physical model developed by Cammarano et al (2006) for a chondritic mantle topped by a 137 km thick ice/water layer. Note that tidal forces due to Io excite Europa's  ${}_0S_2$  when the ocean is several kilometers thick, Ganymede's effect becomes relevant when the ocean is a few kilometers thick, and frequency overlap with the dynamical tide due to Jupiter occurs when the ocean is a mere 100 m thick.

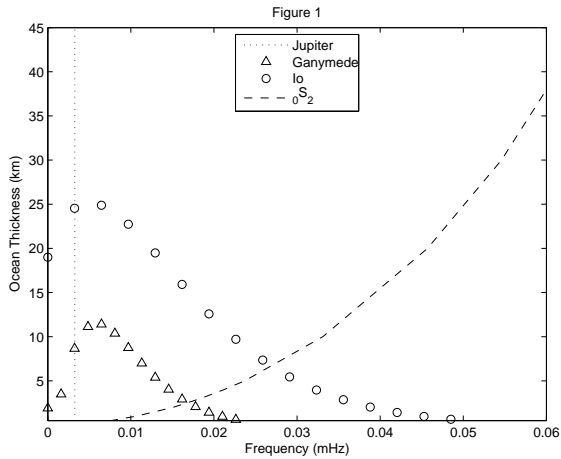


Figure 3.70: The dashed line shows the frequency of  ${}_0S_2$  as a function of ocean thickness. Frequencies and amplitudes (in arbitrary units) of tidal forcing due to Ganymede (triangles) and Io (circles) are also shown. The dominant frequency of Jupiter forcing is indicated by the vertical dotted line.

In Figure 3.71, we show the frequency of  ${}_0S_2$  on Enceladus as a function of the thickness of a hypothetical subsurface ocean. We consider a physical structure of Enceladus which fits the density and shape constraints (Porco et al., 2006). Our model consists of a core with a density of  $\rho = 1700 \text{ kgm}^{-3}$  overlain by a ocean/ice layer that is 10 km thick. The low density of the rocky core is consistent with a 2:3 rock-to-water mixture. We use the upper bounds on seismic velocities in the mantle derived by computing the Voigt average of the rock and water moduli (Watt et al., 1976). We consider a fully differentiated Enceladus – with a non-porous chondritic interior and a  $\sim 50 \text{ km}$  thick ocean/ice layer – to be unlikely, given the paucity of accretionary and radiogenic heating, and inconsistency with the observed shape (Porco et al., 2006). Note that tidal forces due to Dione and Rhea excite  ${}_0S_2$  when the thickness of the hypothetical subsurface ocean  $\leq 1 \text{ km}$ .

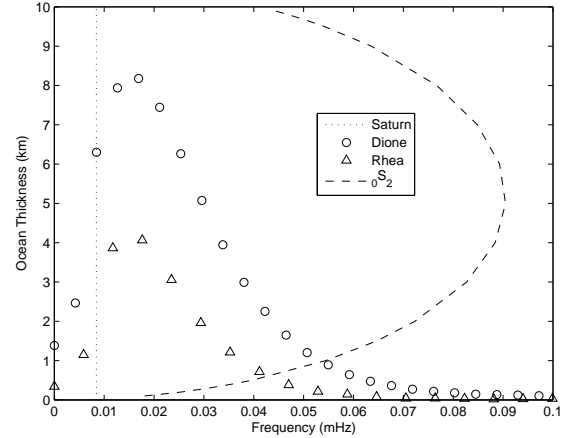


Figure 3.71: The dashed line shows the frequency of  ${}_0S_2$  as a function of ocean thickness. Frequencies and amplitudes (in arbitrary units) of tidal forcing due to Rhea (triangles) and Dione (circles) are also shown. The dominant frequency of Saturn forcing is indicated by the vertical dotted line.

### 33.4 Implications and Future Work

Having identified the interactions that may give rise to tidal excitation of free oscillations, we shall proceed to quantify the effect, and determine whether it is, or may have been, an important source of heat for Europa and Enceladus. Since  ${}_0S_2$  frequencies for very thin ice shells are of the same order as the Maxwell relaxation time, we must modify our purely elastic treatment of the problem to include effects of viscosity.

Recent modeling of Ceres by McCord and Sotin (2005) suggests that it may have a subsurface ocean layer, which would result in very low frequency for  ${}_0S_2$ . We will explore the implications that tidal excitation of free oscillations has for Ceres and other bodies suspected of harboring subsurface oceans (e.g. Callisto, Ganymede, etc.). Furthermore, the transfer of angular momentum into heat through excitation of free oscillations – even if insufficient to drastically raise the temperature within the affected body – may significantly affect orbital evolution within the Jovian and Saturnian systems, or perhaps even the asteroid belt.

### 33.5 References

- Cammarano, F., V. Lekic, M. Manga, et al., Long period seismology on Europa: I. Physically consistent interior models. submitted to *J. Geophys. Res.*
- Hansen, C.J., L. Esposito, A.I.F. Stewart, et al., Enceladus' water vapor plume. *Science*, 311, 1422-1425. 2006.
- Hussmann, H and T. Spohn, Thermal-orbital evolution

of Europa. *Icarus*, 171, 391-410, 2004.

Kivelson, M.G., K.K. Khurana, C.T. Russell, et al., Galileo magnetometer measurements: A stronger case for a subsurface ocean at Europa. *Science*, 289, 1340-1343, 2000.

Marion, G.M., C.H. Fritsen, H. Eicken, et al., The search for life on Europa: Limiting environmental factors, potential habitats, and earth analogues. *Astrobiology*, 3:4, 785-811, 2003.

McCord, T.B. and C. Sotin, Ceres: Evolution and current state. *J. Geophys. Res.*, 110, doi:10.1029/2004JE002244, 2005.

Poirier, J.P., L. Boloh, and P. Chambon, Tidal dissipation in small viscoelastic ice moons: The case of Enceladus. *Icarus*, 55, 218-230, 1983.

Porco, C.C., P. Helfenstein, P.C. Thomas, et al., Cassini observes the active south pole of Enceladus. *Science*, 311, 1393-1401. 2006.

Press, W.H. and S.A. Teukolsky. On formation of close binaries by two-body tidal capture. *Astrophys. J.*, 213, 183-192, 1977.

Spencer, J.R., J.C. Pearl, M. Segura, et al., Cassini encounters Enceladus: Background and the discovery of a south polar hot spot. *Science*, 311, 1401-1405, 2006.

Watt, J.P., G.F. Davies and R.J. O'Connell, The elastic properties of composite materials. *Rev. of Geophys. and Space Phys.*, 14:4, 541-563, 1976.

Woodhouse, J.H., The calculation of eigenfrequencies and eigenfunctions of the free oscillations of the Earth and the Sun. *Seismological Algorithms*, ed. Doornbos, D.J., 321-370, 1988.

Wu, Y. and N. Murray, Planet migration and binary companions: The case of HD 80606b. *Astrophys. J.*, 589, 605-614, 2003.

# 34. A Comparison of Standard Inversion, Neural Networks and Support Vector Machines

Karl Kappler, Heidi Kuzma, James W. Rector

## 34.1 Summary

The object of geophysical inversion is to recover earth parameters from measured data. If the relationship between an earth model and the data is linear, then three different methods of data interpretation, linear inversion, Neural Networks and Support Vector Machines, arrive at the same model from different paradigms. Linear inversion finds a model by minimizing a least squares objective function to which there is a closed form solution. NNs and SVMs use training data to approximate a functional inverse. If the relationship between models and data is non-linear, there is no longer a closed form solution to the inversion objective function, and a model is found by iterative guessing, or by applying a linear approximation to the non-linear physics governing the problem in conjunction with standard linear inversion. An NN finds non-linear relationships by adopting an architecture tuned to a user-designed search algorithm. A SVM is rendered non-linear by changing a single parameter. All three approaches can be used independently or in combination. We are actively developing a tutorial which explains the differences and relationships between these methods.

## 34.2 Introduction

Geophysical relationships can be written

$$d = G(m) \tag{3.4}$$

$d$  is a vector of measured data,  $m$  is a vector of model parameters that describe the earth, and  $G$  is a function derived from physics and geometry. The goal of geophysical inversion is to find  $m$ , given  $G$  and  $d$ .

### Linear Inversion

If the relationship between data and models is linear, then  $G$  can be written as a matrix of coefficients:

$$d = Gm \tag{3.5}$$

Least squares linear inversion is done by minimizing an objective function:

$$m_{inv} = \underset{m}{\operatorname{argmin}} ((d - Gm)^T (d - Gm)) \tag{3.6}$$

which has the well known closed form solution

$$m_{inv} = (G^T G)^{-1} G^T d \tag{3.7}$$

Notice that any vector of data can be inverted once the matrix  $(G^T G)^{-1} G^T$  has been computed.

### Inversion via Machine Learning

In the machine learning paradigm, it is assumed that examples of  $m$  and  $d$  are available, and  $G$  does not necessarily have to be known. The goal of inversion via machine learning, either with a Neural Network or a Support Vector Machine, is to find a function  $S$  such that

$$m_{ML} = S(d) \approx SVD(d) \approx NN(d) \tag{3.8}$$

In geophysics, usually  $G$  is known, and it is possible to select a series of example models and use  $G$  to compute a corresponding set of training data. The goal of a linear machine learning problem is to find  $S$  such that

$$M = DS \tag{3.9}$$

$M$  is now a matrix of example or 'training models' and  $D$  is a matrix in which each row is the corresponding 'training data'.

### Linear Neural Network

Another frame of reference in which to cast information processing is that of a network of interlinked, adaptive data structures, broadly known as neural networks. The neural net format is inspired by the neuron model. The neuron is composed of three main parts. There are the input channels (dendrites), a cell which performs a function on the inputs (the neuron body), and an output channel to conduct the function result away from the body (axon).

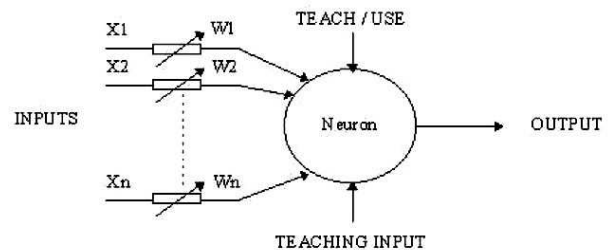


Figure 3.72: Schematic of a single Neuron

In a simple, linear neural net, the inputs are subjected to a weighting scheme which seeks to optimize the output of the network. The method of steepest ascent is the most common method of selecting weights for the input

Inversion, NN and SVM channels. In the case of a linear weighting scheme applied to a single set of inputs, the steepest ascent reduces to the method of ordinary least squares, or linear inversion. Neural Network approaches to computing partition the coding into nodal structures like the neuron and interlink the nodes with axon/dendrites. Using the NN paradigm when designing software is helpful in making the design modular.

### Linear SVM

Least Squares SVMs (LS-SVM) are derived starting from equation 6 by minimizing an objective function of the form.

$$S_{SVM} = \underset{S}{\operatorname{argmin}} (C(DS - M)T(DS - M) - STS) \quad (3.10)$$

If the scalar C (picked by the user) is very large, then the solution to equation (7) reduces to

$$S_{SVM} = (G^T G)^{-1} G^T \quad (3.11)$$

Instead of solving equation 7 directly, an LS-SVM is derived from an equivalent, dual form of the minimization (Kuzma, 2003). The solution is formed in terms of inner-products, or Kernel functions. In the simplest case the kernel function is just the standard dot-product. A LS-SVM does not find S directly, but instead finds a set of coefficients  $\alpha$  such that

$$\alpha = (DD^T + \frac{1}{2C})^{-1} M \quad (3.12)$$

To then use the SVM to find a model from new data, the following is computed

$$m = SVM(d) = \sum_{\text{training data}} \alpha_i (d_i^T d) \quad (3.13)$$

In essence the SVM is approximating the model which fits the field data by 'projecting' the field data onto a basis of training data vectors (the support vectors). Thus a weighted linear combination of training models forms the solution. This is described in more detail in the tutorial we are preparing.

### Non-Linear Inversion

If the relationship between models and data is not linear, then it is no longer possible to invert G directly. Nonlinear iterative inversions rely on numerical methods to minimize objective functions similar to that in equation 3. Non-linear inversion follows a sequence of steps:

1. Make an initial guess for m
2. Compute data (or gradients) via equation 1
3. Update the guess for m
4. Repeat steps 2 and 3 until a solution is established

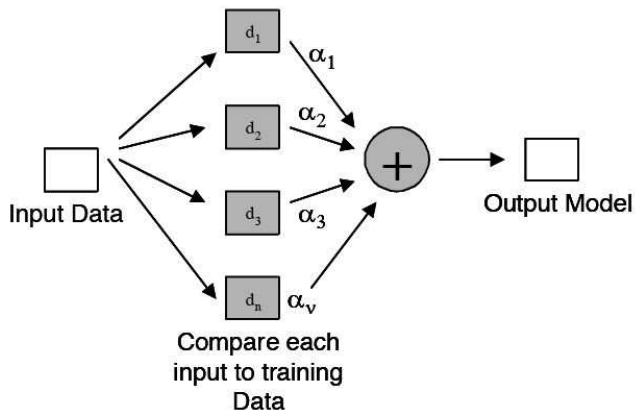


Figure 3.73: Given proper training data, the models found from a linear LS-SVM are equivalent to those found by linear inversion

In practice, many different algorithms may be used for nonlinear inversion. Constraints, regularization and limits on step size may be used to force the solution toward desired models. In our tutorial we treat the following common numerical methods by outlining them conceptually, and citing formulae:

Newton's Method

Gradient : Steepest Ascent/Descent

Conjugate Gradient

Monte Carlo methods: Genetic and Simulated Annealing

Occam's Constraint

Some of the pitfalls of each method, such as slow convergence or choice of a good starting model are discussed, as well as tricks to avoid these pitfalls. For example using a simple SVM to select a good starting model and a decaying step size applied to a subsequent gradient search.

### Non-linear NN

A linear NN refers to the linear relationship between neurons. Each node itself can be working in a non-linear fashion, as in the case of a network of switching nodes in which node potentials decay exponentially when node is off, and increase linear when it is on (Kappler et al. 2002). The linearity is in the connection between nodes. The state or potential of a given node depends on a linear function of the state and the potentials of its input nodes. The NN offers the advantage of being adaptable, and can respond to a changing data set on the fly, where as a linear inversion needs to be recomputed whenever a data set changes. The SVM and NN share this property, that once trained they can interpret new data for free.

A more complicated neural net often uses connectivity as a strength for optimizing a solution. Once the data are

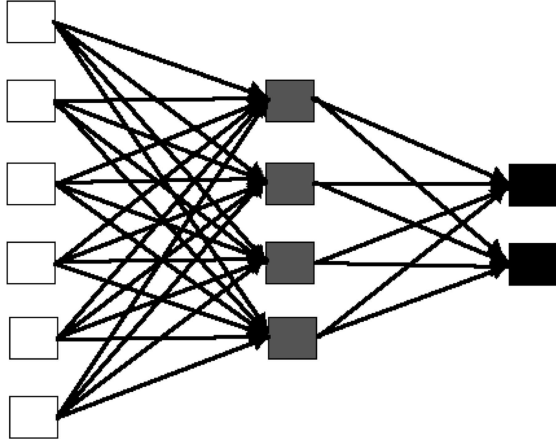


Figure 3.74: Diagram of a neural net with a single hidden layer, comprised of four nodes

input, a series of hidden layers are used to analyze different aspects of data. The connection strengths between nodes can be varied. A NN could incorporate a group of parallel SVMs, each optimizing different functions, and weighting the inversion from each SVM into a resulting output.

A description of a NN which emulates an SVM and the supporting mathematics can be found in *Haykin* CH7. In the NN paradigm, SVMs are known as radial basis function networks.

### Non-Linear SVMs

The architecture of a non-linear SVM is the same as the architecture of a linear SVM except that dot products are replaced by kernel function. To capture non-linear relationships in an LS-SVM, equations 11 and 12 are replaced by

$$\alpha = \left(\Gamma + \frac{1}{2C}\right)^{-1}M \quad (3.14)$$

$$\Gamma_{i,j} = K(d_i, d_j) \quad (3.15)$$

$$m = \sum_{\text{trainingdata}} \alpha_i K(d_i^T d) \quad (3.16)$$

The kernel function  $K(d_i, d_j)$  can be any function such that the Gram matrix,  $G$ , is positive definite (has no negative eigenvalues). In practice,  $K$  is picked by trial and error out of a small library of kernels. Training the SVM means finding the  $s$ , which still only requires inverting a well conditioned matrix that is the size of the number of training examples.

### 34.3 Implications and Future Work

The ordinary method of linear inversion can be recovered from simple assumptions applied to Neural Networks and SVMs. The NN and SVM approach however offer several advantages such as adaptability, expanding training sets without restarting the inversion, and nonlinear methods. The framework of a NN is also intuitive in the sense that the neural clusters can be set up so that each set of nodes is working on a specific user defined question.

### 34.4 Acknowledgments

The DCI Postdoctoral Fellowship Program partially supported this work.

### 34.5 References

- Haykin, S., 1994, *Neural Networks*, A comprehensive Foundation, Macmillan
- Kappler et al., 2002 *Dynamics in High Dimensional Networks*, *Signal Processing, Elsevier*
- Kuzma, H. A., Rector, J.W., (2004), *Non-linear AVO inversion using support vector machines: 74th annual International Meeting of Soc. Expl. Geophysics* Scholkopf, B. and Smola, A., 2002, *Learning with Kernels, Support Vector Machines, Regularization, Optimization, and Beyond: The MIT Press.*

